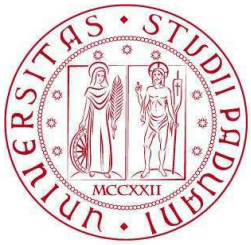

UNIVERSITÀ
DEGLI STUDI
DI PADOVA

Host Institution: Università degli Studi di Padova

Dipartimento di Geoscienze

DOCTORAL COURSE IN EARTH SCIENCES

SERIES XXIX

NON–INVASIVE MONITORING AND NUMERICAL MODELING OF THE SOIL–PLANT CONTINUUM

Coordinator: Ch.mo Prof. Fabrizio Nestola
Supervisor: Ch.mo Prof. Giorgio Cassiani
Co-Supervisor: Dott. Jacopo Boaga

PhD Candidate: Laura Busato

"Those who have handled sciences
have been either men of experiment or men of dogmas.
The men of experiment are like the ant, they only collect and use;
the reasoners resemble spiders,
who make cobwebs out of their own substance.
But the bee takes a middle course:
it gathers its material from the flowers of the garden and of the field,
but transforms and digests it by a power of its own."
F. Bacon., *The New Organon [Book One]*, 1620.

Contents

***

List of Figures **ii**

List of Tables **iii**

List of Symbols **vii**

Abstract **ix**

Sommario **xi**

1 Introduction **1**
1.1 Outline: the Soil–Plant continuum 2

2 Electrical resistivity tomography **7**
2.1 Founding principles 7
2.2 In situ measurements 10
2.2.1 Electrode arrays 10
2.2.2 Non-homogeneous soil 11
2.3 Survey configuration for electrical resistivity tomography 12
2.3.1 2–D imaging: surface surveys 12
2.3.2 3–D imaging: surface and borehole surveys 13
2.4 Processing, inversion, and interpretation 14
2.4.1 Measurement errors 14
2.4.2 Forward modeling 15
2.4.3 Inverse modeling 16
2.4.4 Time–lapse inversion 18

3 Bulgherano field site: data acquisition and analysis **19**
3.1 Site description 20
3.2 Data acquisition 21
3.2.1 Micrometeorological and sap flow measurements 21
3.2.2 Small–scale 3–D ERT acquisitions 22
3.3 ERT data inversion and results 24

3.3.1 Living orange tree . . . 25
3.3.2 Dead orange tree . . . 28
3.4 Discussion . . . 29

4 Palazzelli field site: data acquisition and analysis 31
4.1 Site description . . . 32
4.2 Data acquisition and analysis . . . 34
4.2.1 Tree transpiration measurements . . . 34
4.2.2 Small–scale 3–D ERT acquisitions . . . 34
4.2.3 Inversion of the ERT data . . . 36
4.3 Results . . . 38
4.3.1 Soil moisture dynamics during the monitoring campaign . . . 38
4.3.2 Long–term ERT monitoring . . . 38
4.3.3 Short–term ERT monitoring . . . 41
4.4 Discussion . . . 46

5 Numerical procedures for the localization of the active root zone 49
5.1 Introduction . . . 49
5.1.1 Outline of the numerical procedure . . . 50
5.1.2 Synthetic case study outline . . . 52
5.2 Model description: CATHY . . . 53
5.3 Taylor series expansion of a multi–variable vector–valued function . . . 56
5.3.1 Example 1: $f(x)$ linear function . . . 56
5.3.2 Example 2: $f(x)$ non–linear function . . . 57
5.4 Newton–Raphson and Picard iteration schemes . . . 59
5.4.1 Numerical discretization . . . 59
5.4.2 Newton–Rapshon and Picard iteration schemes . . . 60
5.5 Estimation of plant transpiration . . . 62
5.6 Example on a saturated domain . . . 64
5.6.1 Introduction . . . 64
5.6.2 Modeling details . . . 65
5.6.3 Application of the numerical procedure . . . 65

6 Synthetic case study 69
6.1 Infiltration model . . . 69
6.2 Plant model . . . 72
6.3 Transpiration reconstruction and discussion . . . 75

7 Conclusions 81
7.1 Challenges for future research . . . 82

Acknowledgments 83

Bibliography 84

A Attachments **93**
A.1 Time–lapse monitoring of the hyporheic zone of an alpine river using non–invasive methodologies 93
A.2 Combined geophysical surveys for the characterization of a reconstructed river embankment 102

List of Figures

***

1.1 Earth's critical zone 1
1.2 Soil–Plant–Atmosphere continuum 3

2.1 Current injection in a 2–D homogeneous half space 9
2.2 Acquisition schemes represented as electrical networks 10
2.3 Wenner, dipole–dipole, and Schlumberger arrays 11
2.4 3–D scheme of a 4–electrode measurement in a nonhomogeneous system 12
2.5 Pseudosection 13

3.1 3–D instrumentation set–up for small–scale ERT measurements . . . 22
3.2 Sector subdivision for irrigation test 23
3.3 Pipeline with borehole electrodes 23
3.4 Absolute inversion of the background measurement (2^{nd} October 2013) 25
3.5 Time–lapse inversions during scheduled irrigation (2^{nd}–3^{rd} October 2013), sap flow, and evapotranspiration 26
3.6 Soil water content variations by means of TDR probes 27
3.7 Time–lapse inversion results of the irrigation test (9^{th} June 2014) . . 28

4.1 Scheme of the randomized block design of irrigation treatments at Palazzelli field site 33
4.2 Electrodes layout with four quadrants for both full irrigation treatment and partial root drying treatment 35
4.3 Three–dimensional distribution of ERT electrodes 36
4.4 Soil water content variations over time for both treatments T1 and T4 39
4.5 ERT absolute inversions, long–term monitoring 40
4.6 ERT time–lapse inversions, short–term monitoring 42
4.7 Time–lapse ERT results on C4 (treatment T1) 44
4.8 Time–lapse ERT results on Q4 (treatment T4) 45

5.1 Finite element mesh for the saturated example 65
5.2 Variation of the uclidean norm of known terms differences with time (saturated example). 66

6.1 Finite element mesh for infiltration and plant models 69
6.2 Pressure head vs soil water content graph for the synthetic simulations 71
6.3 Pressure head vs relative hydraulic conductivity graph for the synthetic simulations 71
6.4 Comparison between real and synthetic plant transpiration 72
6.5 Evolution of saturation in the irrigation and plant models 74
6.6 Comparison between real transpiration and exact reconstruction: vertical section 76
6.7 Comparison between real transpiration and approximated reconstruction: vertical section 77
6.8 Comparison between real transpiration and approximated reconstruction as seen from top 79

List of Tables

***

3.1 Summary of ERT measurements and irrigation schedule at Bulgherano, October 2013 – living orange tree 24
3.2 Summary of ERT measurements and irrigation schedule at Bulgherano, June 2014 – dead orange tree 24

4.1 Summary of ERT measurements at Palazzelli 37

6.1 Soil and van Genuchten parameters for the infiltration and plant models 70
6.2 Plant parameters for the synthetic plant model 73

List of Symbols

***

Electrical resistivity tomography

α	Parameter regulating balance between data misfit and model objective function during the ERT inversion.
$\delta(x)$	Dirac delta function
λ	Integration variable of the Stefanescu integral, i.e. wavenumber
∇	Gradient operator
$\Phi(m)$	Objective function
$\Phi_d(m)$	Data misfit
$\Phi_m(m)$	Stabilizing objective function
ρ	Electrical resistivity
ρ_a	Apparent resistivity
ρ_m	Resistivity of the forward model
σ	Electrical conductivity
$\tilde{v}$	Transformed electrical potential by means of Fourier transform
a	Minimum error level
b	Error increase with transfer resistance
C_S	Cross–section of a given cylinder for R definition
d	Vector of real ERT data
E	Error of the direct–reciprocal measurements pair
e	Gaussian error model
E_{fw}	Forward model percent error
f	Forward model operator
I	Electric current
I_0	Imposed current flux for Neumann boundary conditions
J	Jacobian
$J_1(\lambda r)$	Bessel function of the first kind and order 1
k	Geometric factor
L	Length of a given cylinder for R definition
m	Set of parameters in ERT forward model
R	Electrical resistance
r	Distance from the current source
R_d	Transfer resistance of direct measurement
R_r	Transfer resistance of reciprocal measurement
R_t	Transfer resistance at acquisition t
R_{hom}	Transfer resistance from a homogeneous resistivity distribution model
R_{TL}	Resistance ratio
S	Sensitivity
$T(\lambda)$	Kernel function of both layer thickness and resistivity
V	Electric potential
W_d	Diagonal data weighting matrix
W_m	Weighting matrix
z_{C_+}	Depth of electrode C_+
z_{P_+}	Depth of electrode P_+

Active root zone identification

A_x	Xylem cross–sectional area
$D(\Theta_h^{k+1,r+1})$	Reconstructed difference of the known terms between E1 and E2
D_{real}	Real difference between the known terms of E1 and E2
d_r	Difference between real and reconstructed known terms differences
α	van Genuchten curve parameter
β	Empirical parameter
Δt	Time step size
ϵ_w	Function of molar weight and density of water
η_z	Gravitational potential energy gradient
γ	Apparent quantum yield
$\hat{\Psi}$	Nodal pressure head solution
λ_{max}	Maximum marginal water use efficiency
∇	Nabla operator
Ω	Discretized domain
ϕ	Porosity
ψ	Soil water potential
ψ_h	Solution approximation (water potential)
ψ_L	Leaf water potential
ψ_R	Root water potential
θ	Volumetric moisture content
θ_h	Solution approximation (water content)
θ_r	Residual moisture content
θ_s	Saturated moisture content
a	Relative diffusivity of water vapor with respect to CO_2
a_1	Photosynthetic parameter
a_2	Photosynthetic parameter
A_c	Term comprising stiffness and mass matrices in the saturated example
A_{cano}	Projected canopy area
A_{xylem}	Xylem area
$b_1(\Theta_h)$	Gravitational term flux
b_2	Neumann boundary conditions flux
$b_3(\Theta_h)$	Flux due to plant activity
c	Vulnerability curve coefficient
$c*_a$	Reference CO_2 concentration
c_a	Ambient CO_2 concentration
c_{cp}	CO_2 compensation point
c_{ic}	Inter–cellular CO_2 concentration
$C_{o,a}$	O_2 concentration in air
$c_{p,25}$	CO_2 compensation point at 25 °C
D	Jacobian matrices in Taylor series approximation
d	Vulnerability curve coefficient
E_l	Elements in Ω
$g_{i,j}$	Soil–to–root conductance
g_r	Root membrane conductance
g_{st}	Bulk leaf conductance
g_s	Soil conductance
g_x	Xylem conductance
$H(\Theta_h)$	Flow stiffness matrix
H_c	Stiffness matrix in the saturated example
h_{cano}	Plant height
K_r	Relative hydraulic conductivity
K_s	Saturated hydraulic conductivity
$K_{c,max25}$	Michealis constant for CO_2 fixation at 25 °C
$K_{o,max25}$	Michealis constant for O_2 fixation at 25 °C
LAI	Leaf area index
N	Nodes in Ω
n	van Genuchten curve exponent
$P(\Theta_h)$	Mass stiffness matrix
P_c	Mass matrix in the saturated example
PAR	Photosynthetically active radiation

q_N	Nodes in Ω
$q_s(\psi)$	Source and sink term
S_s	Elastic storage
S_w	Water saturation
t	Time
T_j	Transpiration rate
u	Vector of three–dimensional coordinates
$V_{c,max25}$	Maximum carboxylation capacity at 25 °C
VPD	Vapor pressure deficit
$w(u)$	Linear basis function
z_L	Height of leaf potential evaluation
z_R	Trunk base elevation

Abstract

***

The Earth's critical zone (ECZ) is the near–surface domain that regulates the availability of most life–sustaining resources. Among all the subdomains of the ECZ, a crucial role is played by the Soil–Plant continuum (SP), as it is a major performer of the exchanges of mass and energy between soil and plants (and then atmosphere). However, despite its importance and its strong interconnection with human activity, the characterization of this subdomain is still in an early stage, mainly because of the lack of spatial and temporal information regarding the occurring processes. To overcome this issue, we present the combination of geophysical measurements and hydrological modeling in the framework of a hydrogeophysical approach, with the aim of characterizing the active root zone, i.e. the portion of the root system involved in the water uptake. In fact, the water uptake is performed by root hair, the microscopic cell outgrowths whose location is difficult (if not impossible) also after the removal of the root system from the soil. Nevertheless, determining its position is fundamental not only for merely scientific purposes, but most of all for practical applications, as it affects the performing of precision irrigation. Therefore, in this work I propose the identification of the active root zone on the basis of its main effect, i.e. the reduction of soil water content over time. This is achieved by means of 3–D small–scale electrical resistivity tomography (ERT) carried out combining superficial and borehole electrodes. We monitored the processes occurring in the root zone of three orange trees located in south–eastern Sicily. These trees are drip irrigated according to different deficit irrigation techniques to improve the exploitation of the water resource, while the plants' transpiration is monitored thanks to sap flow and eddy covariance measurements. More in detail, in the first case study ERT measurements before and after the cut of the tree are compared, while in the second case study the ERT monitoring is focused on two orange trees drip irrigated with different treatments (i.e. full irrigation and partial root drying). The datasets thus obtained provide interesting insights into the root system activity, given their abundance of information regarding both atmospheric and underground phenomena (i.e. transpiration and root water uptake, respectively). In particular, the ERT time–lapse approach well highlights the portions subject to a decrease in water content, which can be related to the water uptake put in place by the plants. Nevertheless, the interpretation of the resistivity patterns, although combined with agronomic information, can be rather intricate. A proper hydrological modeling pro-

vides a solution to this problem, even if choosing the most suitable approach requires a specific mathematical analysis. To do this, we developed a synthetic case study with two identical hydrological models, one of which describing also the activity of an orange tree. These models resemble the real datasets provided by the ERT measurements, without all the uncertainties introduced by the geophysical acquisition and the model calibration. The location of the active root zone is reconstructed from the combination of these two models by means of Taylor series expansion, with particular reference to the effects of the approximation thus introduced. The final aim is to evaluate the proposed numerical procedure for a future application on one of real case study presented in this work.

Sommario

***

La Earth's critical zone (ECZ) rappresenta la porzione più esterna del pianeta Terra ed è sede di numerosi processi che regolano la disponibilità della maggior parte delle sostanze necessarie alla vita. Tra i vari sottodomini in cui essa può essere suddivisa, il continuum Suolo–Pianta (SP) svolge un ruolo cruciale, in quanto è uno dei maggiori regolatori degli scambi di massa ed energia tra suolo e piante (e quindi atmosfera). Nonostante la forte interconnessione con l'attività umana, la caratterizzazione del SP è ancora in una fase embrionale, principalmente legata alla mancanza di informazioni sia spaziali che temporali riguardo ai processi che lo caratterizzano. In questo lavoro presentiamo quindi una combinazione di tomografia di resistività elettrica (ERT) e modellazione idrologica secondo l'approccio idrogeofisico, con l'obiettivo di caratterizzare la "active root zone", ossia la porzione del sistema radicale coinvolta nel processo di assorbimento di acqua dal suolo. Più nel dettaglio, questo processo è messo in atto dai peli radicali, delle microscopiche estroflessioni la cui localizzazione è difficile (se non impossibile) anche in seguito alla rimozione del sistema radicale dal suolo. Ciononostante, la sua localizzazione è fondamentale soprattutto da un punto di vista agronomico, poiché necessaria per una corretta applicazione delle tecniche di irrigazione di precisione. In questo lavoro presento quindi due casi studio in cui l'active root zone è identificata sulla base del suo effetto principale, ossia la diminuzione di contenuto idrico del suolo. I casi studio presentati comprendono tre alberi d'arancio situati nel sud–est della Sicilia ed irrigati mediante diverse tecniche di microirrigazione (nota anche come "irrigazione a goccia"). In particolare, nel primo caso studio sono comparate misure ERT acquisite prima e dopo il taglio della pianta, mentre nel secondo caso studio il monitoraggio ERT è focalizzato su due aranci irrigati con diverse tecniche (piena irrigazione e disseccamento parziale delle radici). Il monitoraggio ERT dei processi in atto è effettuato sulla piccola scala (cioè sulla singola pianta) grazie alla combinazione di elettrodi superficiali ed in pozzo, permettendo così una acquisizione ed una rappresentazione tridimensionale del dato geofisico. Parallelamente ha luogo anche il monitoraggio agronomico, grazie al quale la traspirazione è determinata mediante misure di sap flow e di eddy covariance. I dati così ottenuti forniscono molte informazioni rispetto ai diversi processi in atto, sia atmosferici (traspirazione), che nel sottosuolo (assorbimento di acqua dal suolo). In particolare, il monitoraggio ERT in time–lapse è in grado di mostrare quali porzioni del dominio investigato siano soggette ad una diminuzione del contenuto idrico, la

quale può essere collegata all'attività radicale. Nonostante la quantità e qualità dei dati a disposizione, l'interpretazione dei risultati (specialmente in termini quantitativi) risulta comunque piuttosto complessa. Una soluzione può essere fornita da un'appropriata modellazione idrologica, sebbene la scelta dell'approccio migliore richieda una specifica analisi matematica. Sotto quest'ottica abbiamo sviluppato un caso sintetico costituito da due modelli idrologici identici, dove uno quali descrive anche l'attività di una pianta d'arancio. Questi modelli hanno lo scopo di ricreare dei dataset riconducibili all'output delle misure ERT, senza però tutte le incertezze introdotte dall'acquisizione geofisica e dalla calibrazione del modello. La ricostruzione della "active root zone" è quindi ottenuta dalla combinazione di questi due modelli mediante l'espansione in serie di Taylor, con particolare attenzione alle approssimazioni così introdotte. L'obiettivo finale è quello di valutare questa procedura numerica per una futura applicazione ad uno dei casi studio reali presentati in questo lavoro.

1

Introduction

***

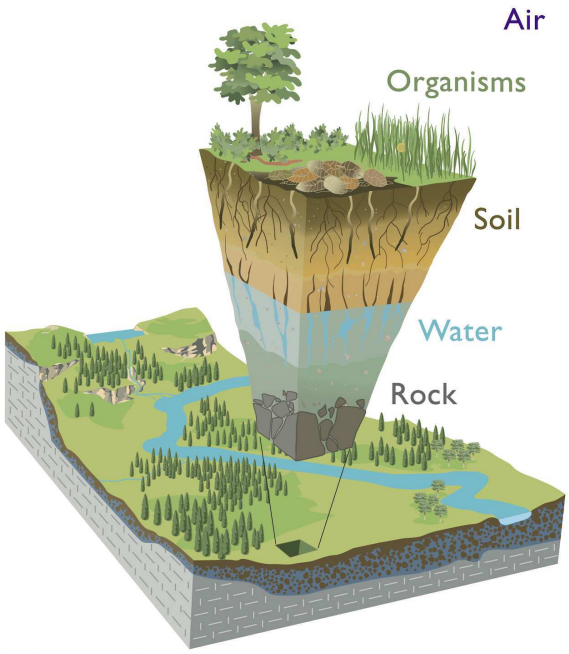

Fig. 1.1: Earth's critical zone representation. Modified from Chorover et al. [2007]

The *Earth's critical zone* (ECZ) is defined by the National Research Council [2001] as the thin outer layer of planet Earth, where the interactions between air, biota, soil, water, and rock occur. In other words, this domain ranges from the top of the vegetation to the bottom of aquifers, as shown in Fig. 1.1, and therefore comprises atmosphere, biosphere, as well as hydrosphere, pedosphere, and lithosphere. The ECZ is location for several interacting processes that operate on second–to–eon timescales and atomic–to–global space scales (e.g. geological evolution, climatic changes, water cycle, etc.) [Brantley et al., 2007]. In fact, this interfacial domain regulates the availability of most life–sustaining resources and is also strongly interconnected with human activity. In particular, ECZ and human activity have strong feedbacks, as they modify each other [Richter and Mobley, 2009]. Moreover, the U.S. NSF National Program [2016] states that 30-50% of global land surface and 50% of freshwater have been used by humans, while croplands and pastures are now overcoming forest cover as major biome on Earth. Along with the increase in human population, the ECZ is subject to an intensification of the operating stressors,

especially in terms of exploitation of the water resource, production of food, and use of the energy sources, with strong effects on their sustainability and development [National Research Council, 2001]. In particular, in the next four decades, the need for food and fuel is assumed to duplicate, while the demand for clean water shall increase of 50% [Banwart et al., 2013].

The importance of the Earth's critical zone is therefore unquestionable and the understanding of the interactions of the ECZ's many components represents a significant scientific challenge [National Research Council, 2001; Richter and Mobley, 2009]. To achieve this goal, a wide range of disciplines (e.g. hydrology, geochemistry, soil science, etc.) is currently involved and operates at different scales by means of an interdisciplinary approach, where theory and (often only punctual) observations are integrated [Richter and Mobley, 2009; Lin, 2010; Banwart et al., 2013]. Even if the Earth's critical zone is the only domain easily accessible to direct observations [National Research Council, 1991] and despite all the efforts made so far, the characterization of this system still requires further improvements. In particular, many questions regarding the coupling of physical, chemical, and biological processes and their spatial and temporal occurrence are still unanswered [U.S. NSF National Program, 2016]. To face these crucial issues, a major step forward may be provided by the application of non– (or minimally–)invasive geophysical techniques. These cost–effective and relatively fast methodologies allow the monitoring of the domain of interest at different scales both in time and space. Moreover, the data thus obtained can be linked to the information supplied by other disciplines through an appropriate modeling process, so as to apply a holistic approach (e.g. Hinnell et al. [2010]; Camporese et al. [2015]; Rossi et al. [2015]).

To test this idea, we decided to focus on three subdomains of the Earth's critical zone: (i) the hyporheic zone (HZ, Orghidan [2010]) of an alpine river, (ii) an artificial embankment, reconstructed after its collapse during a flood event, and (iii) the Soil–Plant continuum in orange trees. Since this last subdomain is the most interesting and challenging ECZ subsystem, among those investigated during my Ph.D. work, we deemed it necessary to focus on it in this dissertation. Nevertheless, some of the results obtained in the other case studies can be found as attachments to this work (see A.1 and A.2, respectively).

1.1 Outline: the Soil–Plant continuum

The *Soil–Plant–Atmosphere continuum* (SPA, Fig. 1.2) is the subdomain of the Earth's critical zone defined by the movement of water from the soil to the atmosphere through plants [Ritchie, 1981; Lambers et al., 2008a]. Recently, this system has experienced an increasing interest from several scientific communities (e.g. hydrologists, ecologists, etc.) [Rodriguez-Iturbe and Porporato, 2004], mainly because of the strong impact of plants on the water cycle, due to evapotranspiration (ET) and root water uptake (RWU) [Porporato et al., 2002]. In particular, the Soil–Plant subsystem (SP) is location of fundamental exchanges of both mass and energy [Pinton et al., 2007], whose understanding has crucial consequences on eco–hydrology, precision agriculture, and sustainable water management, as well as modeling of soil

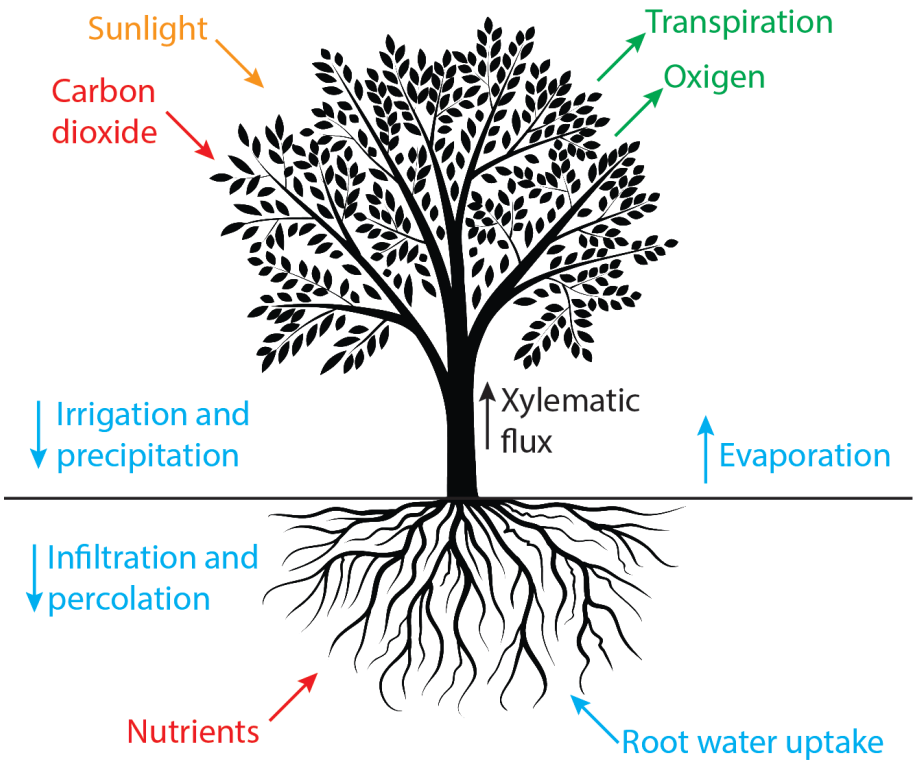

Fig. 1.2: Schematic representation of the main processes characterizing the Soil–Plant–Atmosphere continuum.

and atmosphere processes [Lynch, 1995].

The SP subsystem is a rather complex domain, where plant metabolism, plant physiology, and plant gross morphology are influenced mainly by the role of water at different scales (e.g. water availability in the soil, water loss through stomata, etc.) [Passioura, 1982]. Particular interest relies on the role of soil as a water reservoir, and on the plant stress arising from a deficient water supply in the root zone [Ritchie, 1981]. This last condition may be a consequence of the soil properties or resulting from the application of deficit irrigation techniques, which consist in providing an amount of water lower than full crop–water requirements [Fereres and Soriano, 2007].

Therefore, the RWU patterns result from the combination of different parameters, such as plant root distribution, type of irrigation, soil texture, and hydraulic conductivity variability [Ritchie, 1981; Cohen et al., 1983; Pinton et al., 2007]. In particular, the application of different irrigation treatments, combined with a fixed plant spacing and cultural activities (e.g. pruning, picking, the use of fertilizers, etc.), could influence the actual extent and location of the active root zone, i.e. the portion of the root system responsible for the root water uptake. More in detail, the RWU is put in place by the root hair [e.g. Pinton et al., 2007; Segal et al., 2008], i.e the microscopic cell outgrowths responsible for water and nutrients collection from the soil. Given the root hair dimensions, it is very difficult, if not impossible, to observe it experimentally, also after the removal of the root system from the soil. Therefore, the RWU patterns can be difficult to capture even with dense networks of point sensors [Jayawickreme et al., 2014]. Thus, there is a growing

demand for near–surface observing technologies for soil characterization, especially for the improvement of precision irrigation techniques [Van Alphen and Stoorvogel, 2000; Sadler et al., 2005]. In this framework, applied geophysics provides useful tools to monitor, e.g., the movement of water in the vadose zone (e.g. Binley et al. [2002]; Deiana et al. [2007]). As a matter of fact, typically applied methodologies are based on punctual measurements that cannot supply spatial information regarding the investigated domain. On the contrary, electrical resistivity tomography (ERT) is probably the most suitable technique, as it is capable of investigating the soil in both two (2–D) and three dimensions (3–D) modes [Binley and Kemna, 2005; Binley, 2015] and, above all, ERT is a minimally invasive approach. Moreover, the key parameter of ERT is resistivity, which is strongly dependent on several factors, but mainly on water and solute content (variations) [Archie, 1942; Binley and Kemna, 2005; Binley, 2015]. Therefore, the active root zone may be located on the basis of its effects (i.e. soil water content variations) on a three–dimensional scale, by means of ERT measurements.

The literature provides several examples describing the application of ERT to the Soil–Plant continuum, demonstrating the potential of this emerging research area, [e.g. Jury et al., 2011]. Werban et al. [2008] and Zanetti et al. [2011] opted for a 2–D set–up on small–scale laboratory samples, focusing on diurnal soil–water redistribution and on differentiation of root samples of trees rooted in dikes, respectively. Still choosing a 2–D approach, Amato et al. [2008] applied ERT to the field, in order to determine the root biomass distribution along tree rows. Jayawickreme et al. [2008] targeted their 2–D measurements on determining subsurface soil moisture changes, instead. A step forward to the three–dimensional set–up is presented by Amato et al. [2009], which use a superficial distribution of electrodes on plastic containers filled with soil and alfalfa grass. A real 3–D instrumentation distribution is employed by Garré et al. [2011], since their investigated domain consists of a lysimeter equipped with electrodes on the lateral surface, with a focus on soil water content variations and on root length density, while other authors opted for the combination of several geophysical techniques [al Hagrey, 2007; Vanderborght et al., 2013]. A full 3–D ERT approach is used by Boaga et al. [2013] and al Hagrey and Petersen [2011], who combine superficial and borehole electrodes at the decimetric scale. More in detail, Boaga et al. [2013] based their work on a field application in an apple orchard, while al Hagrey and Petersen's work [2011] is based on a forward modeling approach. These studies show the adaptability of ERT to the characterization of the Soil–Plant continuum, even if difficulties in the interpretation of the measured electrical resistivity patterns remain (especially when dealing with field studies). Still, some guidelines can be gathered, in order to optimize the application of ERT to the SP domain: (i) choose a decimetric scale, to better deal with the spatial variability of RWU patterns [Michot et al., 2003], (ii) adopt a time–lapse scheme (i.e. observe the variations taking place with respect to a background condition) to reduce the impact of the factors influencing the bulk resistivity [Michot et al., 2003], and (iii) conduct the time–lapse acquisitions with a high temporal frequency, in order to avoid temporal aliasing [Koestel et al., 2009].

Although these works provide useful and promising insights into the application of electrical resistivity tomography for the characterization of the SP continuum,

a complete exploitation of the obtainable information could be carried out only through appropriate modeling processes, where all available data (e.g. geophysical data, micrometeorological data, hydrological data, etc.) are combined [Hinnell et al., 2010; Camporese et al., 2015]. This integrated approach belongs to the field known as *hydrogeophysics* [e.g. Rubin and Hubbard, 2005; Vereecken et al., 2006; Binley et al., 2010, 2015], which is aimed at coupling geophysical data with hydrological models. One of the most evident advantages of this *modus operandi* is the possibility of including spatial information provided by ERT into models describing the movement of water in the vadose zone. In this way, the limited information content provided by punctual measurements can be overcome (e.g. Hinnell et al. [2010]). However, to the best of our knowledge, a combination of ERT and hydrological modeling has never been applied to locate the active root zone, except for a first one–dimensional attempt by Cassiani et al. [2015], even if the exact position of the active root zone plays a pivotal role in precision agriculture (e.g. Srayeddin and Doussan [2009]). In fact, many authors focus on other aspects of the SP continuum modeling, like choosing the best approach to describe RWU, i.e. considering it as a chain process based on resistance laws [Schneider et al., 2010] or relying on potential transpiration rates and stress functions [Jarvis, 2011], while other authors move to the micro–scale and model the rhizosphere from X–ray or synchrotron images (e.g. Schmidt et al. [2012] and Keyes et al. [2013]).

In this dissertation we present two case studies where small–scale 3–D ERT is applied on different drip–irrigated orange trees located in south–eastern Sicily, to characterize their active root zone. Our main goals comprise the assessing of field applications of small–scale 3–D ERT, in terms of both qualitative description of SP interactions and location of active root zone dynamics, as well as improving the SP continuum characterization thanks to the combination of the ERT data with numerical models. In the first example (chap. 3), we carry out ERT measurements on a single tree, combining acquisitions while the tree is living and then after its cutting. Thus, we can monitor the same domain both with and without the activity of the orange tree. In the second example (chap. 4), we concentrate on two 8–year old trees watered by means of deficit precision irrigation. More in detail, one tree is fully irrigated, while the other one is watered with half of water lost by means of evapotranspiration. In both cases, the datasets obtained are rather complex (in terms of resistivity patterns) but are also rich of information and their comparison highlights differences that may be related to the different irrigation treatments. Finally, in chap. 5 and chap. 6 we develop a synthetic case study to assess the applicability of a 3–D approach to detect the location of the active root zone. Given the novelty of this procedure, we focus on the development of both mathematical and numerical features, necessary for a future application to a real case study.

2

Electrical resistivity tomography

***

Electrical resistivity tomography (ERT) is a non–invasive active geophysical method that provides insights regarding an investigated domain on the basis of its electrical properties. Nowadays, this technique is state of the art in the field known as Hydrogeophysics [e.g. Rubin and Hubbard, 2005; Vereecken et al., 2006; Binley et al., 2010, 2015], given its strong dependance on water content (variations) as well as on water chemistry. The aim of this chapter is to provide a concise description of this methodology with the definition of some fundamental concepts.

2.1 Founding principles

ERT, as other geophysical direct current (DC) methods, is based upon Ohm's law

$$V = I\ R \tag{2.1}$$

where V is the electric voltage [$L^2\ M\ T^{-3}\ A^{-1}$], I is the injected current [A], and R is the resistance [R]. This last parameter is related to other material and geometric properties. In fact, if we consider a cylinder with length L [L], cross–section C_S [L^2] and we apply a potential V to it to allow the flowing of a current I, we have:

$$R = \frac{\rho L}{C_S} \tag{2.2}$$

where ρ is the *electrical resistivity* [R L]. Electrical resistivity can also be defined as the inverse of electrical conductivity σ ($\rho = \sigma^{-1}$). It is important to underline that electrical resistivity is a property of the considered material and, therefore, it does not depend on current intensity or electrode array geometry (see sec. 2.2). In fact, resistivity is particularly suitable for measuring variations in soil water content, ionic content of the pore water, and other parameters, given its dependence on them (for further details see Archie [1942]; Binley and Kemna [2005]; Binley [2015]).

As described by Binley and Kemna [2005] and Binley [2015], if we consider an isotropic three–dimensional (3–D) electrical resistivity distribution $\rho(x, y, z)$, we can describe the 3–D electric potential $V(x, y, z)$ due to the injection of a current I at a known position using Poisson's equation

$$\nabla \cdot \left(\frac{1}{\rho} \nabla V \right) = -I\delta(x) \tag{2.3}$$

where $\nabla = \dfrac{\partial}{\partial x}, \dfrac{\partial}{\partial y}, \dfrac{\partial}{\partial z}$ is the nabla operator and δ is the Dirac delta function. The boundary conditions to eq. (2.3) can be described as follows

– Dirichlet boundary conditions:

$$V(r \to \infty) = 0 \tag{2.4}$$

where

$$\begin{cases} r = \sqrt{x^2 + y^2 + z^2} \\ z \leq 0 \end{cases} \tag{2.5}$$

– Neumann boundary conditions:

$$\sigma \frac{\partial V}{\partial x}\bigg|_{x=x_0} = I_0 \tag{2.6}$$

where r is the distance from the current source [L] and I_0 is the imposed current flux at the boundary [A].

The first solution to eq. (2.3) can be obtained considering two current electrodes injecting current I from ground surface, with one of them located at an infinite distance (Fig. 2.1). If we also assume a homogeneous resistivity distribution and a current sink at infinity we have

$$V(r) = \frac{I\rho}{2\pi r} \tag{2.7}$$

Note that the domain is here considered to be semi–infinite for $z \leq 0$ (see eq. (2.5)).

However, the typical geoelectrical acquisition employs a combination of four electrodes, called *quadrupole*, with two current electrodes (C_+ and C_-, used for the current injection) and two potential electrodes (P_+ and P_-, used for the potential measurement) (see sec. 2.2). Given the linearity of eq. (2.1), in this case the voltage V can be determined using the superposition principle, thus obtaining

$$\Delta V = \frac{I\rho}{2\pi} \left[\left(\frac{1}{r_1} - \frac{1}{r_3} \right) - \left(\frac{1}{r_2} - \frac{1}{r_4} \right) \right] \tag{2.8}$$

where r_1 is the distance between C_+ and P_+, r_2 is the distance between C_- and P_+, r_3 is the distance between C_+ and P_-, and r_4 is the distance between C_- and P_- (see, for example, Fig. 2.3).

The use of four electrodes is a consequence of the physical properties of both soil and electrodes [Daily et al., 2004]. The soil is actually an ionic conductor, while the electrodes are electronic conductors, as they are usually metallic. Therefore, a high contact resistance may arise (up to 10^4 Ω), thus hindering the current flux from the electrodes to the soil. If only two electrodes are used (Fig. 2.2(a)), both contact

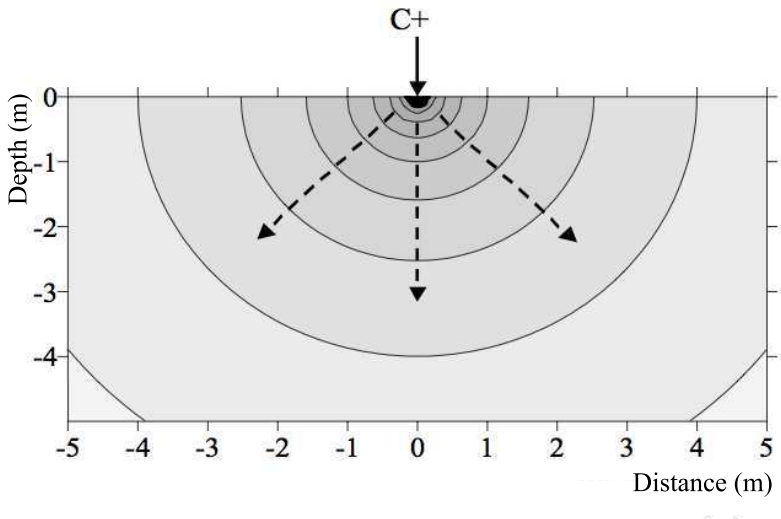

Fig. 2.1: 2–D scheme representing current injection in a homogeneous half space. C_+ is the current electrode, with C_- located at an infinite distance. Both current–flow lines (dotted lines) and equipotential lines (bold lines) are represented. Image taken from [Binley and Kemna, 2005].

resistances and soil resistance would be in series. As a consequence, the measured value would be the sum of these contributions. On the contrary, if we take advantage of four electrodes (Fig. 2.2(b)), we can ignore the contact resistances of C_+ and C_- (even if it is still present), since only the injected current is measured. V is measured using electrodes P_+ and P_-, for which the contact resistances are still present, but are non influential, as there is no current flux across them. This is guaranteed by the high internal impedance of the voltmeter used to measure V. Therefore, the use of four electrodes allows the measurement of the sole soil resistance.

Apparent resistivity

It is possibile to rewrite eq. (2.8) in terms of resistivity:

$$\rho_a = \frac{k\Delta V}{I} \tag{2.9}$$

where k is a term called *geometric factor* that depends on the chosen array (see sec. 2.2.1), since it can be expressed as

$$k = 2\pi\left[\left(\frac{1}{r_1} - \frac{1}{r_3}\right) - \left(\frac{1}{r_2} - \frac{1}{r_4}\right)\right]^{-1} \tag{2.10}$$

The resistivity expressed in eq. (2.9) is called *apparent resistivity*, as it is the value corresponding to the real resistivity ρ if we were considering a homogeneous, flat earth domain [Binley, 2015].

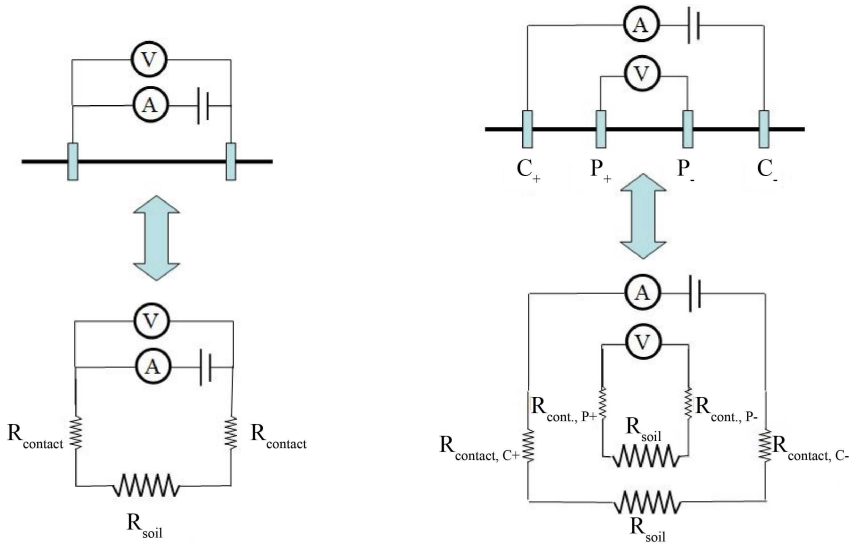

(a) Two electrodes (b) Four electrodes

Fig. 2.2: Acquisition schemes represented as electrical networks: (a) two electrodes and (b) four electrodes.

2.2 In situ measurements

As already described above, the general approach consists in injecting a current into the soil using two current electrodes and then measuring the generated voltage drop using two other ones. Several configurations (known as *arrays*) are available, each with different pros and cons. In addition to this, the survey planning should take into account also other factors, like the objective of the study, the depth of investigation, site access, and instrument limitations.

2.2.1 Electrode arrays

An electrode array is a geometric configuration describing the relative position of current and potential electrodes in a quadrupole [Binley and Kemna, 2005]. The most commonly used electrode arrays are represented in Fig. 2.3.

Each configuration has its advantages and disadvantages, therefore they should be chosen according to the specific application and to the expected signal strength [Seidel and Lange, 2007]. More in detail, Wenner and Schlumberger arrays have relatively stronger signals with respect to dipole–dipole, as the potential electrodes are located within the current electrode pair. Moreover, when using a dipole–dipole array with high electrode pairs separation, the resulting voltage gradients may be rather low.

Another useful indicator is the *sensitivity*, which "gives a measure of how the observed apparent resistivity is sensitive to changes in variation of resistivity of the subsurface" [Binley, 2015], and can be defined as follows

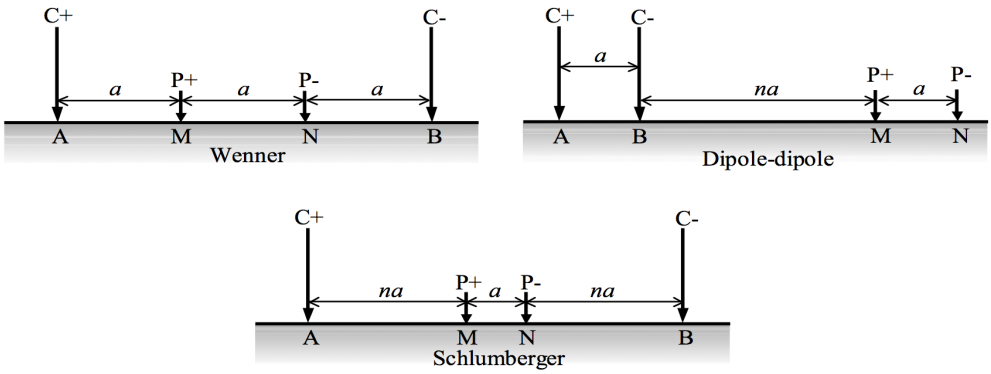

Fig. 2.3: Example of the three most commonly used electrode arrays: Wenner, Dipole-dipole, and Schlumberger. Image taken from [Binley and Kemna, 2005].

$$S = \frac{\partial \log(\rho_a)}{\partial \log(\rho)} \tag{2.11}$$

The Wenner array has average sensitivity to lateral and vertical variability, a good vertical resolution, but reaches small depths of investigation. The Schlumberger array is the most sensitive to lateral variations, so it is useful when exploring vertical variability of the resistivity field. Finally, dipole–dipole has the highest depth of investigation and is highly suitable for lateral profiling, since the vertical resolution is rather low [Binley and Kemna, 2005].

2.2.2 Non-homogeneous soil

The equations described in sec. 2.1 have been developed considering a homogeneous system but, as can be easily imagined, this is not the situation when dealing with a natural environment. Even if the spatial distribution of the electrical resistivity is neither homogeneous nor isotropic, the linearity of Ohm's law is still guaranteed, therefore eq. (2.8) can be applied also in this case [Seidel and Lange, 2007].

If we consider a two–layer domain (as schematised in Fig. 2.4), we can see how the current–flux lines are modified given the resistivity variation with depth (compare with Fig. 2.1). From the comparison of these two pictures (i.e. Fig. 2.1 and Fig. 2.4), we can gather another important piece of information. If we increase the length of the array, the current lines penetrate deeper. Thus, when the length is short, the current paths investigate only the upper part of the subsurface domain and therefore may not explore the lower layer. This means that as the array length increases, the depth (and volume) of investigation expands. Consequently, the apparent resistivity is influenced as well, since it depends on the electrical features of both layers.

This principle can be extended to a domain with a higher number of layers and other heterogeneities, showing how apparent resistivity varies according to both vertical and lateral variations in subsurface resistivity. Considering the definition given in sec. 2.1, in this case we would have that ρ_a is not equal to the real resistivity distribution, as it is referred to a nonhomogeneous domain. Therefore, an appropriate

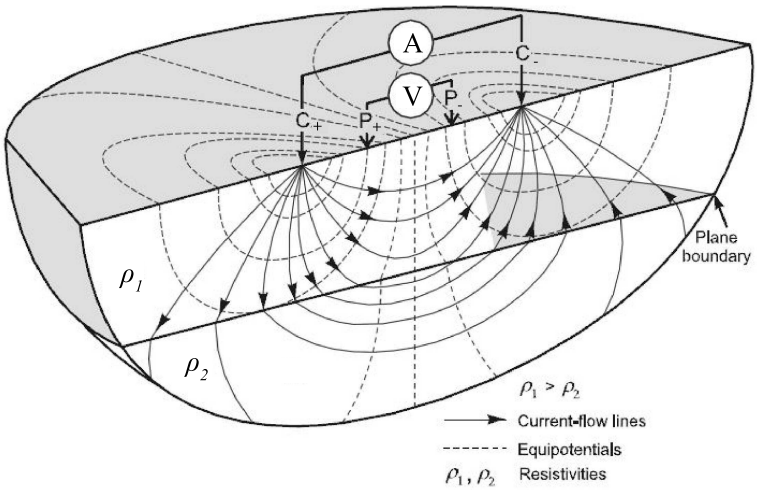

Fig. 2.4: 3–D scheme representing a 4–electrode measurement in a nonhomogeneous system. C_+ and C_- are the current electrodes, P_+ and P_- are the potential electrodes, ρ_1 is the resistivity of the upper layer, and ρ_2 is the resistivity of the lower layer, with $\rho_1 > \rho_2$. Both current–flow lines and equipotential lines are represented. Image taken from [Seidel and Lange, 2007].

data processing, called *inversion process*, is mandatory to assess the real resistivity structure (see sec. 2.4) [Binley and Kemna, 2005].

2.3 Survey configuration for electrical resistivity tomography

Electrical resistivity tomography applies the principles described in the previous sections to multi–electrode systems, leading to two– and three–dimensional images of the subsoil. This technique is widely applied given its large adaptability to the requirements of each case study, as it allows both surface and borehole measurements (or, as in our case study, a combination of them). Furthermore, ERT is also cost–effective, fast to apply, and can be considered a non–invasive method.

2.3.1 2–D imaging: surface surveys

One of the typical applications of ERT is from the ground surface, where several electrodes (e.g. 48, 72, or 96) are placed along a straight line to acquire a so–called 2–D cross–section. Location and spacing of these electrodes are chosen according to the objectives of the survey. The measurement takes place using a *resistivity meter*, which automatically switches between current and potential electrodes according to the chosen sequence thanks to a multiplexer. This instrument also measures and stores the resulting potential for each quadrupole, as well as other parameters chosen by the operator. The electrodes are linked to the resistivity meter thanks to one or more multicore cables. The literature provides many examples of ERT 2–D surveys in a wide range of conditions (see e.g. [Griffiths and Turnbull, 1985; Kemna et al., 2002; Busato et al., 2016]).

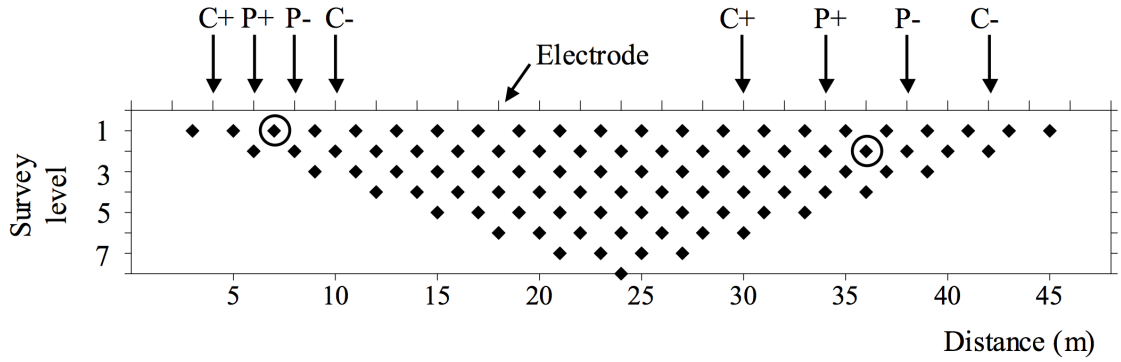

Fig. 2.5: Building of a pseudosection using a Wenner array. The different survey levels correspond to a specific electrode spacing. The circles represent the position of the assigned measurement for each of two represented spacings. Image taken form [Binley and Kemna, 2005].

The first result of a 2–D survey is a *pseudosection*, which is a plot of apparent resistivity as a function of location along the profile and electrode separation. It has been developed for the first time by Hallof [1957] using a dipole–dipole array. An example of the construction of a pseudosection is given in Fig. 2.5: Each point represents a value of ρ_a , whose position depends on the quadrupole location along the survey line and on the spacing between electrodes. As a result, the bigger is the distance between electrodes, the higher is the survey level and, therefore, the higher is the pseudodepth of the apparent resistivity value (in analogy with what described in sec. 2.2 regarding the depth of investigation). Here we consider only a Wenner array, but this approach can be easily extended to the other quadrupole configurations.

Even if the pseudosection is a useful measurement output, it is important to underline once again that it does not correspond to the real resistivity distribution, which can be obtained only through an appropriate inversion process (see sec. 2.4). In other words, the pseudosection only represents, in a suitable form, the raw data.

2.3.2 3–D imaging: surface and borehole surveys

Two–dimensional surveys can be easily expanded in the third dimension, thanks to the increasing availability of multichannel instruments and more powerful computational tools (both hardware and software).

A first example is provided by quasi 3–D imaging (e.g. Cassiani et al. [2006]), where multiple 2–D transects are combined to gather a 3–D representation. This approach requires less resources in terms of instrumentation and computational efforts if compared to the real three–dimensional imaging but, as a consequence, shows low sensitivity to ρ variations in the direction normal to the survey lines.

To perform a real three–dimensional ERT imaging we can use either a surface configuration or borehole electrodes (or, as in our case study, a combination of them, see subsec. 3.2.2 and subsec. 4.2.2). In the first case, electrodes cover a superficial two–dimensional grid, as described, for instance, by Nyquist and Roth [2005], while the second case requires an ad hoc instrumentation setup.

More in detail, the borehole instrumentation usually consists of a plastic pipe around which the electrodes (e.g. consisting of metallic bands) are wrapped. Each electrode is then linked to the resistivity meter thanks to a multicore cable. Since each borehole is equipped with a pipe, the instrumentation placement needs to be carefully handled, as an appropriate coupling between the electrodes and the soil is crucial. This process is easier when the pipe is located below the water table, while in the vadose zone it requires particular care, especially when dealing with a very dry soil. In fact, below the water table a free electrode cable can be used if submerged in water, provided that the casing is fully slotted.

Also in this case it is possible to compute a pseudosection, even if the boundary conditions are different from what described in sec. 2.1. As described by Binley [2015], the computation of the apparent resistivity has to account for the noninfinite surface boundary if the electrodes placement is superficial. Therefore, if we consider an infinitely deep electrode, eq. (2.7) becomes

$$V = \frac{I\rho}{4\pi r} \tag{2.12}$$

We can also modify eq. (2.8) considering a current electrode at depth z_{C_+}, a potential electrode at depth z_{P_+}, and accounting for the surface boundary at $z = 0$. As a result we obtain

$$V = \frac{I\rho}{4\pi}\left[\frac{1}{|z_{C_+} - z_{P_+}|} + \frac{1}{z_{C_+} + z_{P_+}}\right] \tag{2.13}$$

Likewise, it is possible to describe the geometric factor considering a borehole quadrupole (see Binley [2015]).

A three–dimensional borehole imaging takes place employing more than two boreholes and all arrays described before can be applied. Resolution and sensitivity do not depend only on the electrode spacing, but also on the distance among boreholes. In general, the highest sensitivity will be close to the boreholes themselves and will decrease with the distance from them, therefore this approach is usually applied on relatively small domains.

2.4 Processing, inversion, and interpretation

The ERT data described in the previous sections need an appropriate elaboration to be turned into the corresponding resistivity spatial distribution. This process requires several steps, from error assessment to data inversion, which have to be handled with particular care.

2.4.1 Measurement errors

ERT measurements are affected by errors that need to be properly considered, as they could influence and invalidate the inversion process [Daily et al., 2004], leading to inversion artefacts or heavy smoothing. These errors arise as a consequence of several physical phenomena:

– Poor soil–electrode contact, which results in systematic errors on particular electrodes.;

– Low input voltage and high geometric factors that may lead to low voltage levels at the potential electrodes, close to the instrumentation resolution;

– Unstable natural self–potentials over time;

– Other random external effects.

An appropriate measurement error assessment is therefore mandatory, in order to properly consider its effects on the inversion procedure. There are two possible approaches: The first is based on the measurements repeatability using several injection cycles, but this does not allow the removal of systematic errors; the second makes use of the so–called *reciprocals* [Parasnis, 1988; Binley et al., 1995]. This latter approach is based on the assumption that the switching of the current source (C_+) with the current sink (C_-) should give an identical measure with reversed polarity. The same should happen when exchanging positive and negative potential electrodes. Even if there are eight possible combinations, usually the reciprocals are determined switching current and potential electrodes. The two transfer resistances thus measured should theoretically be identical, but this does not happen when dealing with real data. Therefore, the difference between these two values can be considered as an error estimate

$$E = R_d - R_r \tag{2.14}$$

with E being the error for that measurement pair, R_d the direct measure, and R_r the reciprocal measure.

Since each transfer resistance pair has its own reciprocal error, it is possible to set an error threshold to remove all the bad measurement pairs. This limit can be evaluated assuming a Gaussian error model, where the magnitude of the reciprocal error increases with the magnitude of the resistance:

$$|e| = a + b|R| \tag{2.15}$$

where a is the minimum error level and b is the error increase with R [Binley et al., 1995].

2.4.2 Forward modeling

Forward modeling is a fundamental part of the inversion process and consists in computing the measurement results starting from a certain distribution of the electrical properties in the considered domain. In other words, forward modeling allows determining the measured data (e.g. transfer resistance) given a certain model, where the spatial variation of resistivity is known [Binley and Kemna, 2005]. Kemna [2000] gives a thorough description of the forward model solution, which can be summarized as follows.

If we consider a two–dimensional distribution of resistivity (i.e. constant along the y direction), it is possible to rewrite eq. (2.3) as

$$\frac{\partial}{\partial x}\left(\frac{1}{\rho}\frac{\partial \tilde{v}}{\partial x}\right)+\frac{\partial}{\partial z}\left(\frac{1}{\rho}\frac{\partial \tilde{v}}{\partial z}\right)-\frac{\tilde{v}k^2}{\rho}=-\frac{I}{2}\delta(x)\delta(z) \tag{2.16}$$

with $\tilde{v}$ being the transformed potential, described using the Fourier transform

$$\tilde{v}(x,k,z)=\int_0^\infty V(x,y,z)\cos(ky)\,dy \tag{2.17}$$

where k is the wave number. The solution of eq. (2.16) for $\tilde{v}$ has then to be transformed using an inverse Fourier transform to obtain $V(x,y,z)$ (see also LaBrecque et al. [1996]).

A solution to eq. (2.3) in terms of apparent resistivity is available also when considering a flat layered earth model. When using the Schlumberger array, the so–called Stefanescu integral provides the following apparent resistivity [Kemna, 2000]

$$\rho_a\left(\frac{\overline{C_+C_-}}{2}\right)=\left(\frac{\overline{C_+C_-}}{2}\right)^2\int_0^\infty T(\lambda)J_1(\lambda r)\lambda\,d\lambda \tag{2.18}$$

where $\frac{\overline{C_+C_-}}{2}$ is the semi–distance between the current electrodes, J_1 is the Bessel function of the first kind and order 1, the kernel $T(\lambda)$ is a function of both layer thickness and resistivity, and λ is the integration variable (i.e. the wavenumber).

The solution to the forward problem when considering a 2–D or 3–D resistivity distribution requires the employment of numerical methods (i.e. finite element, FE, or finite difference, FD), which are based on a representation of the domain realized by means of a grid or a *mesh*), made of a number of nodes and elements. Thus, the solution representing the potential field is provided at each node (or at each element centroid). A more detailed description of the development of the numerical methods for the solution of the geoelectrical problem is provided by Binley [2015].

2.4.3 Inverse modeling

Contrary to forward modeling, the inverse problem is aimed at computing the real resistivity distribution starting from a dataset made of electrical measurements (in our case, transfer resistances). Nevertheless, the numerical approach is still based on the principles of forward modeling, since its final aim is to determine a model m reproducing the real data d within a specified uncertainty (error) level [Binley and Kemna, 2005; Seidel and Lange, 2007], where

$$m=\{m_j\}=\{\ln\sigma_j\}\qquad(j=1,...M) \tag{2.19}$$

is a vector representing the electrical properties distribution to be determined, discretized into a set of parameters, and

$$d=\{d_i\}=\{-\ln R_i\}\qquad(i=1,...N) \tag{2.20}$$

is the set of measured transfer resistances. In both cases, the logarithms account for the wide range of values that describe both parameters, while the minus symbol in eq. (2.20) is due to the physical dimensions used in eq. (2.19).

The resistivity inversion problem is notoriously affected by innate non–uniqueness, as several (if not infinite) models lead to the same response, within the same error level. If we also consider that the real dataset d is often incomplete, it is clear that an appropriate model restriction is mandatory to obtain a solution with physical and practical significance.

This is commonly achieved through the application of the "Occam's razor" principle, as described by Constable et al. [1987], which consists in considering as the best solution the smoothest model agreeing with the data within their error level. This approach is based on solving the inverse problem as a regularized optimization problem [Tikhonov and Arsenin, 1977], where a given *objective function*

$$\Phi(m) = \Phi_d(m) + \alpha\Phi_m(m) \tag{2.21}$$

has to be minimized. In eq. (2.21) Φ_d is the data misfit defined as

$$\Phi_d(m) = ||W_d[(d) - f(m)]||^2 \tag{2.22}$$

where $||\cdot||$ is the Euclidean norm, f is the forward model operator, and W_d is the diagonal data weighting matrix, and $\Phi_m(m)$ is a stabilizing objective function

$$\Phi_m(m) = ||W_m(m - m_{ref})|| \tag{2.23}$$

used to add some model constraints relative to a reference model m_{ref}, based on a certain weighting matrix W_m. Finally, α regulates the exchanges between the data misfit and the model objective function during the inversion.

The minimization of eq. (2.21) can be computed adopting the Gauss–Newton approach, which leads to the following iterative scheme [Binley, 2015]

$$(J^T W_d^T W_d J + \alpha R) = \Delta m = J^T W_d^T (d - F(m_k)) - \alpha R m_k \tag{2.24}$$

where J is the Jacobian $\left(J_{i,j} = \left\{\frac{\partial d_i}{\partial m_j}\right\}\right)$, m_k is the parameter set at iteration k, and Δm is the parameter set update at iteration k, so as to have

$$m_{k+1} = m_k + \Delta m \tag{2.25}$$

At each step k, α is reduced until convergence is reached. Finally, the solution is achieved (i.e. the iteration process is stopped) when the data misfit reaches a value of 1. To do this, the data error has to be known, but this is possible thanks to the approach described in subsec. 2.4.1. More details are provided, e.g., by Kemna [2000].

3–D inverse modeling

The solution of a three–dimensional inverse problem requires significant computational effort. Some important steps forward have been made thanks to the development of finite element algorithms based on *unstructured meshes*, which allow a variation of the element dimensions in the inversion domain. The main idea is that the area with the highest resolution is characterized by more nodes and therefore

more (tiny) elements (so–called refined grid), while the outer domain (where an exact solution is not required) is described by bigger elements. This allows not only a better adaptation to the problem geometry (thanks also to the different 3–D elements geometry available - e.g. tetrahedra or parallelepipedes), but also reduces the mesh's dimensions (in terms of nodes and elements), resulting in a lower computational inversion time.

2.4.4 Time–lapse inversion

The solution of a 2–D or 3–D ERT inversion problem consists in producing a resistivity distribution representing the investigated domain at the measurement time. But the electrical resistivity tomography is capable of showing the variations in resistivity also over time, with respect to a background condition. This approach is called *time–lapse inversion* and has been developed by Daily et al. [1992]. It is based on the following equation

$$R_{TL} = \frac{R_t}{R_0} R_{hom} \tag{2.26}$$

where R_{TL} is the resistance ratio, R_t is the transfer resistance of the acquisition at time t, R_0 is the background resistance, and R_{hom} is the transfer resistance resulting from a homogeneous resistivity distribution model. Eq. (2.26) is computed for each measurement belonging to a common–set, which comprises the measurements made only from the quadrupoles present, and accurate within a given error level, at all acquisition times.

The resulting, new dataset is then inverted, leading to $T - 1$ (with T = total number of acquisitions) images, each representing the variations in terms of resistivity between the background acquisition ($t_0 = 0$) and the current acquisition (t), expressed as *resistivity ratio %*. This parameter shows an increase in resistivity over time when reaches values bigger than 100%, while indicates a decrease in resistivity for values lower than 100%. It follows that a resistivity ratio % equal to 100% denotes no resistivity variations from t_0 to t.

3

Bulgherano field site: data acquisition and analysis

***

In this chapter I present the first case study, consisting of an orange tree located in an orange orchard in south–eastern Sicily. Here, we took advantage of small–scale 3D electrical resistivity tomography combining superficial and borehole electrodes to characterize and monitor the active root zone (i.e. the part of the root system that performs the root water uptake) during the scheduled irrigation. This site is equipped with an eddy covariance (EC) tower and sap flow probes, to monitor the tree activity also from an agronomic point of view. Our ERT measurements took place in two different periods, October 2013 and June 2014, which correspond to two different conditions of the orange tree. In October the plant was active, so we followed the scheduled irrigation repeating our measurements at regular intervals. In June, on the contrary, the tree had been cut, since it was affected with *Citrus Tristeza virus*. However, the whole root system and the geophysical instrumentation were left in place, thus allowing a new irrigation test in the same location of the previous campaign.

The part of this chapter describing the monitoring of the living tree has been published by Cassiani et al. [2015], who used this dataset to develop a one–dimensional model aimed at determining the extent of the active root zone, with particular attention to the location of the drip irrigators. In this work, I reconsider the 2013 material and add it to the inversion and analysis of the 2014 measurements, as the whole dataset (i.e. comprising both measurement campaigns) is particularly suitable for a three–dimensional hydrological model developed to locate the active root system. Thus, this case study is appropriate for an application of the procedure described in chap. 5 to real data.

The main aim of these experiments is to study the applicability of small–scale 3D ERT to characterize and monitor the active root zone of an orange tree, with particular reference to the occurring phenomena (e.g. root water uptake). This is possible thanks to the strong dependence of electrical resistivity on soil water content variations (among other parameters, see sec. 2.1). In particular, the combination of two different irrigation tests, carried out before and after the cut of the orange tree, give us different insights into same domain in two different conditions, i.e. with and without the activity of the tree, respectively.

3.1 Site description

The studied plant is a 20 year–old orange tree (*Citrus sinensis; cv Tarocco Ippolito*) planted in an orange orchard in south–eastern Sicily (Lentini, SR – lat. 37°16' N, long. 14° 53' E). This orchard has an extension of 20 ha and lies in a semi–arid climate, with average annual precipitation of 550 mm, dry summers (average air temperature of 28 °C), and wetter winters (average air temperature of 7 °C). Here, the tree spacing is equal to 4.0 m within each row, while the spacing between rows is 5.5 m to allow cultural operations (e.g. pruning and picking). The irrigation takes place thanks to a drip irrigation system (see e.g. Dasberg and Or [1999]) consisting of four in–line drippers per plant, spaced 1 m. The water discharge per dripper is equal to 4 l h^{-1} (i.e. 0.73 mm h^{-1}), so the total amount of water provided to each tree is 16 l h^{-1}. Irrigation is supplied every day for five hours from May to October.

A thorough description of the soil properties is provided by Aiello et al. [2014] and is based on a subdivision of the orchard into smaller domains, each with an area of 18 × 32 m^2. Here, 64 undisturbed soil samples (from 32 sampling points) were collected at depth ranges of 0–0.05 m and 0.05–0.10 m. These undisturbed samples allowed the determination of soil bulk density, ρ_b [M/L^3], and initial water content, θ_i [L^3 L^{-3}]. Soil textural properties have been ascertained thanks to 32 disturbed soil cores collected at depth ranging between 0 and 0.05 m. This assessment is based on the conventional methods consisting in eliminating the organic matter and deflocculating the clay fraction [Gee and Bauder, 1986]. Then, the soil classification is carried out according to the USDA (United States Department of Agriculture) standard via both textural and hydraulic laboratory analysis [Gee and Bauder, 1986], taking into account three textural fractions: clay (0–2 μm), silt (2–50 μm), and sand (50–2000 μm). The results show sandy loam textures for most samples (27 out of 32) and loamy sand textures for the remaining ones. Finally, Aiello et al. [2014] determined also the van Genuchten water retention model parameters [van Genuchten and Nielsen, 1985] on the basis of Burdine [1953] conditions. To do this, they considered the 32 most superficial undisturbed cores and used stainless steel cylinders with an inner volume of 10^{-4} m^3. For each sample, the volumetric soil water content at 11 pressure heads were determined by means of a sandbox and a pressure plate apparatus.

The site is also equipped with water content reflectometers (TDR) probes, aimed at measuring soil water content variations over time in the portion of soil belonging to each orange tree. Therefore, each location is equipped with four sensors, two inserted vertically at 0.20 m and 0.45 m below ground level, and two inserted horizontally at 0.35 m depth, with 0.20 m spacing in between: the former provide information on the first 0.20–0.-25 m of soil, while the latter were used to detect the passing of the water plume. The sensors consists of two stainless steel rods connected to a printed circuit board. More in detail, calibrated Campbell Scientific CS616 water content reflectometers (±2.5% of accuracy) were installed to hourly monitor the changes of volumetric soil water content ($\Delta\theta$).

This orchard has mean leaf area index (LAI) of about 4 m^2 m^{-2}, rather constant in time (referred to the ERT measurement campaign – see subsec. 3.2.2), while the mean photosynthetic active radiation (PAR) light attenuation is 50% between rows

and 80% within rows.

The plant we chose for our monitoring, however, was effected by *Citrus Tristeza virus*, a pathogen that infects several commercial varieties of *Citrus* on rootstock [Moreno et al., 2008]. The symptoms vary according to several factors and, usually, lead to a quick decline of the plant [Moreno et al., 2008]. For this reason, the tree was cut during spring 2014, while the root system has been left in place. This allowed us to carry out the ERT measurements while the plant was living (i.e. while RWU was taking place), and after the death of the tree (see subsec. 3.2.2).

3.2 Data acquisition

The characterization of this site is carried out from two different points of view, agricultural and geophysical.

3.2.1 Micrometeorological and sap flow measurements

The orchard considered in this case study is equipped with an eddy covariance (EC) tower that measures turbulent fluxes in the low atmosphere by means of high frequency measurements of several parameters, such as water vapour, CO_2, three–dimensional wind speed, and temperature variations. More in detail, this micrometeorogical tower is equipped with two CNR 1 Kipp & Zonen (Campbell Scientific Ltd.) net radiometers at a height of 8 m to measure the net radiation (R_n, [J/T]), three soil heat flux plates (HFP01, Campbell Scientific Ltd.) located 0.05 m below ground level to measure the soil heat flux density (G, [(J L^2)/T]), two sonic anemometers (Windmaster Pro, Gill Instruments Ltd., at 4 m above ground level, and CSAT, Campbell Sci., at 8 m) to estimate the three wind speed components, two fine wire thermocouples to measure air temperature at heights equal to 4 m and 8 m, a gas analyzer (LI–7500, LI–COR) installed at 8 m and acquiring values at a frequency of 10 Hz. In addition, also low–frequency measurements are taken for air temperature (HMP45C,Vaisala), humidity (HMP45C,Vaisala), atmospheric pressure (CS106, Campbell Scientific Ltd.), and wind speed and direction (05103 RM Young). These sensors are located at 4, 8, and 10 m above ground level. Both the EC system and the EC data analysis are based the EUROFLUX standard defined by Aubinet et al. [1999].

In addition to micrometeorological measurements, also hourly meteorological data are available. This service is provided by the Agrometeorological Service of the Sicilian Region (SIAS), thanks to an automatic weather station located 7 km from the orchard. Thus rainfall, incoming short–wave solar radiation, air humidity, air temperature, and wind speed data are supplied. Moreover, the fetch for the dominant wind directions is larger than 550 m, while for the other sectors the minimum fetch is equal to 400 m.

On the considered tree, sap flow is measured using the heat pulse velocity (HPV) technique [Swanson and Whitfield, 1981], which is based on the measurement of temperature variations produced by a heat pulse of short duration (1–2 s). This is possible thanks to two temperature probes installed asymmetrically on both sides

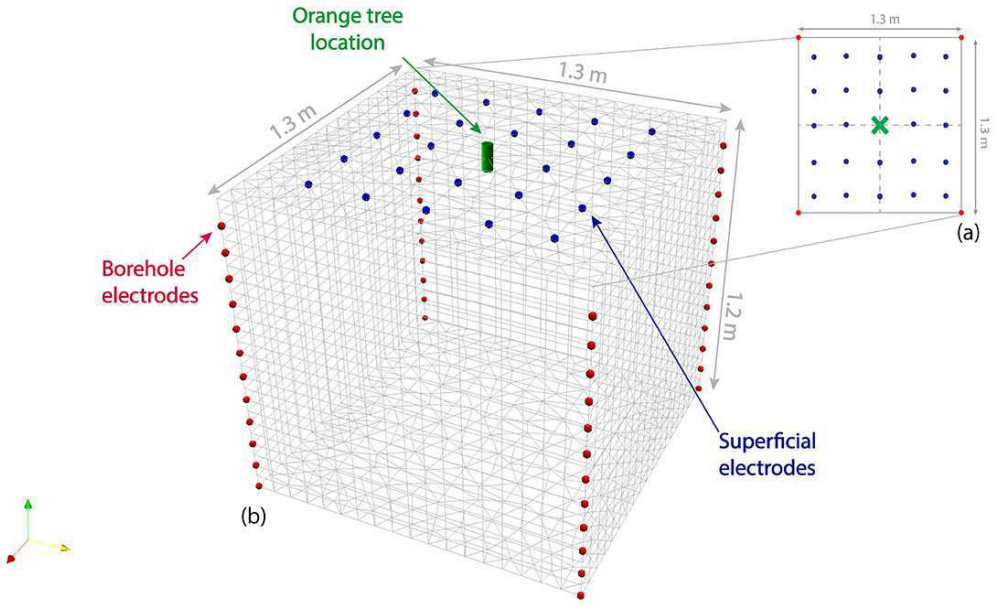

Fig. 3.1: 3–D instrumentation set–up for small–scale ERT measurements at the Bulgherano field site: (a) view in plant and (b) three–dimensional representation. The red circles locate the four boreholes, the blue circles indicate the superficial electrodes, and the green cross pinpoints the trunk of the tree. Image taken from Cassiani et al. [2015].

of a linear heater inserted into the trunk. More in detail, here we used two 4 cm sap flow probes with four thermocouples embedded (Tranzflo NZ Ltd., Palmerston North, New Zealand). These probes are located on the north and south sides of the tree, 0.5 m above ground level, and wired to a data logger (CR1000, Campbell Sci., USA). The thermocouples are therefore located 5, 15, 25, and 45 mm within the trunk, while the sampling interval is 30 minutes. The data processing took place according to Green et al. [2003] and consisted in integrating sap flow velocity over the whole sapwood area. The combination of eddy covariance and sap flow measurements, with particular reference to *Citrus sinensis* trees, is described, e.g., by Motisi et al. [2012].

3.2.2 Small–scale 3–D ERT acquisitions

The ERT monitoring is aimed at characterizing the active root zone of this orange tree. Therefore, we took advantage of a 3–D small–scale set–up, where superficial and micro–borehole electrodes are combined. More in detail, 24 stainless steel superficial electrodes cover a grid with spacing of about 0.21 m, centered on the orange tree. The edges of this superficial grid correspond to the location of four micro–boreholes (i.e. a square with side equal to 1.3 m, Fig. 3.1(a)), each one containing 12 electrodes spaced 0.1 m (Fig. 3.1(b)). These electrodes consist of a metallic band 0.03 m high wrapped around a plastic pipe with diameter equal to 1 in (Fig. 3.3(a)). Thus, the deepest electrodes are located 1.2 m below ground level. The plastic pipe is made of 13 waterproof segments to allow an internal wiring, as shown in Fig.

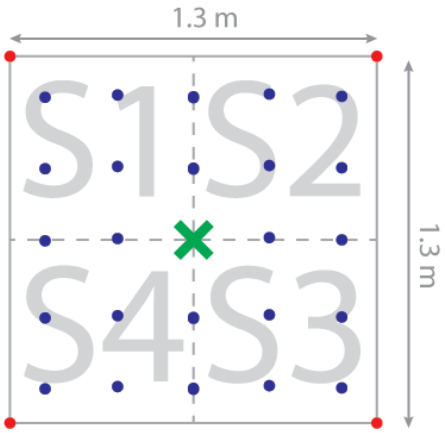

Fig. 3.2: Sector subdivision for irrigation test at the Bulgherano field site. The red circles locate the four boreholes, the blue circles indicate the superficial electrodes, and the green cross pinpoints the trunk of the tree. Image taken from Cassiani et al. [2015].

3.3(b).

(a) Pipeline with electrodes (b) Internal wiring

Fig. 3.3: Pipeline with borehole electrodes. (a) The 12 electrodes (metallic bands) are spaced 0.1 m, for a total length of 1.2 m, and (b) the wiring is completely internal.

The first measurement campaign took place in October 2013 and lasted for two days during irrigation, as summarized in Tab. 3.1. It is important to underline that during the previous 15 days irrigation had been suspended, therefore choosing acquisition 00 as background survey (i.e. prior to the beginning of irrigation, see Tab. 3.1) allows referring all variations due to irrigation and RWU to this relatively dry condition.

The second measurement campaign was actually an irrigation test, performed after the cut of the tree canopy. We subdivided the superficial grid into four smaller sub–sectors (Fig. 3.2), each one irrigated with 25 l of water. We alternated irrigation on each sector (from S1 to S4) and measurements on the whole domain, as described in Tab. 3.2.

For each ERT survey we opted for a dipole–dipole skip–0 acquisition scheme (i.e., the distance between electrodes forming each dipole is equal to the electrode spacing, see Fig. 2.3). This array has maximum spatial resolution but poor signal–to–noise ratio at large separations between potential and electrode pairs (see sec. 2.2.1). However, given the small–scale we are working at, this last issue is not crucial. The

Date	Acquisition number	Starting time	Ending time	Irrigation schedule
2^{nd} October 2013	00	10:40	11:00	11:30 to 16:30 $4\ l\ h^{-1}$ ($0.73\ mm\ h^{-1}$) from each dripper
	01	12:00	12:20	
	02	13:00	13:20	
	03	14:15	14:35	
	04	15:00	15:20	
	05	16:00	16:20	
	06	17:00	17:20	
3^{rd} October 2013	07	10:15	10:35	07:00 to 12:00 $4\ l\ h^{-1}$ ($0.73\ mm\ h^{-1}$) from each dripper
	08	11:05	11:25	
	09	12:00	12:20	
	10	13:00	13:20	
	11	14:00	14:20	
	12	15:00	15:20	
	13	15:45	16:05	

Tab. 3.1: ERT acquisitions and irrigation schedule at the Bulgherano field site in October 2013, while the plant was still living. All times are referred to the local time zone.

Irrigation		Acquisitions		
Sector	Starting time	Label	Starting time	Ending time
		M0	11:10	11:30
S1	11:30	M1	11:40	12:00
S2	12:05	M2	12:15	12:35
S3	12:40	M3	12:50	13:10
S4	13:15	M4	14:33	14:53

Tab. 3.2: ERT acquisitions at the Bulgherano field site on 9^{th} June 2014, after the cut of the tree canopy. S1, S2, S3, and S4 indicate the corresponding sector, as shown in Fig. 3.1. M0 is the background acquisition for this irrigation test. All times are referred to the local time zone.

sequence used includes all 72 electrodes and 4885 measurements, obtained combining direct and reciprocal measurements (see subsec. 2.4.1) and so–called "dummy quadrupoles" for acquisition efficiency using the resistivity meter's 10 physical channels. The instrument is an IRIS Syscal Pro resistivity meter. Moreover, the pulse duration was fixed at 250 ms and the potential minimal reading was set normally at 50 mV. Prior to each acquisition, we checked the electrical contact between electrodes and soil, in order to verify that the coupling was good enough to allow the current injection. Each ERT survey lasted 20 minutes.

3.3 ERT data inversion and results

The ERT data at our disposal call for two different types of inversion. The first one leads to the representation of the absolute resistivity distribution, which allows the

description of the state of the domain at the survey time, while the latter aims at highlighting how resistivity varies with respect to a background condition. For all inversions we used R3t software [Binley, 2013] and a triangular prism mesh, with 27020 nodes and 51068 elements.

3.3.1 Living orange tree

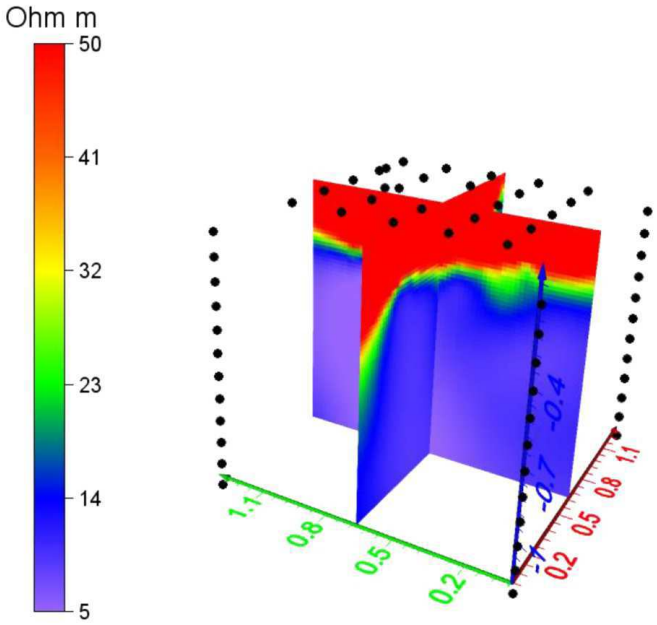

Fig. 3.4: Absolute inversion of the background measurement (2^{nd} October 2013, 11:00 LT). The variation in resistivity is mainly one–dimensional with depth. Image taken from Cassiani et al. [2015]

First of all, we concentrated on acquisition 00 (2^{nd} October 2013, see Tab. 3.1), representing the relatively dry conditions at the field site before the beginning of irrigation. The first step consisted in removing all measurement pairs (i.e. direct and reciprocal) with an error higher than 10%, on the basis of the approach described in subsec. 2.4.1. This value, 10%, is also the error level for the absolute inversion. The result shows that the upper 0.4 m of the soil has average resistivity of about 40–50 Ωm, while in the lower part resistivity is one order of magnitude smaller, about 5 Ωm (Fig. 3.4). It is reasonable to attribute this contrast to differences in soil water content and to the presence of the root system, as the characterization of the soil showed a rather homogeneous condition (see sec. 3.1).

Resistivity variations over time, with respect to acquisition 00, can be highlighted thanks to the time–lapse approach. In this case, the error level for the inversions has been lowered to 2%, in agreement with other examples in literature (e.g. Cassiani et al. [2006]). The dataset has been analyzed according to the steps described in subsec. 2.4.4. The results for two selected times (i.e. acquisitions 01 and 07) are shown in Fig. 3.5(b). The main variations are localized in the top 0.4 m of the soil and, for a matter of clarity, can be split into the two main components: (i) resistivity

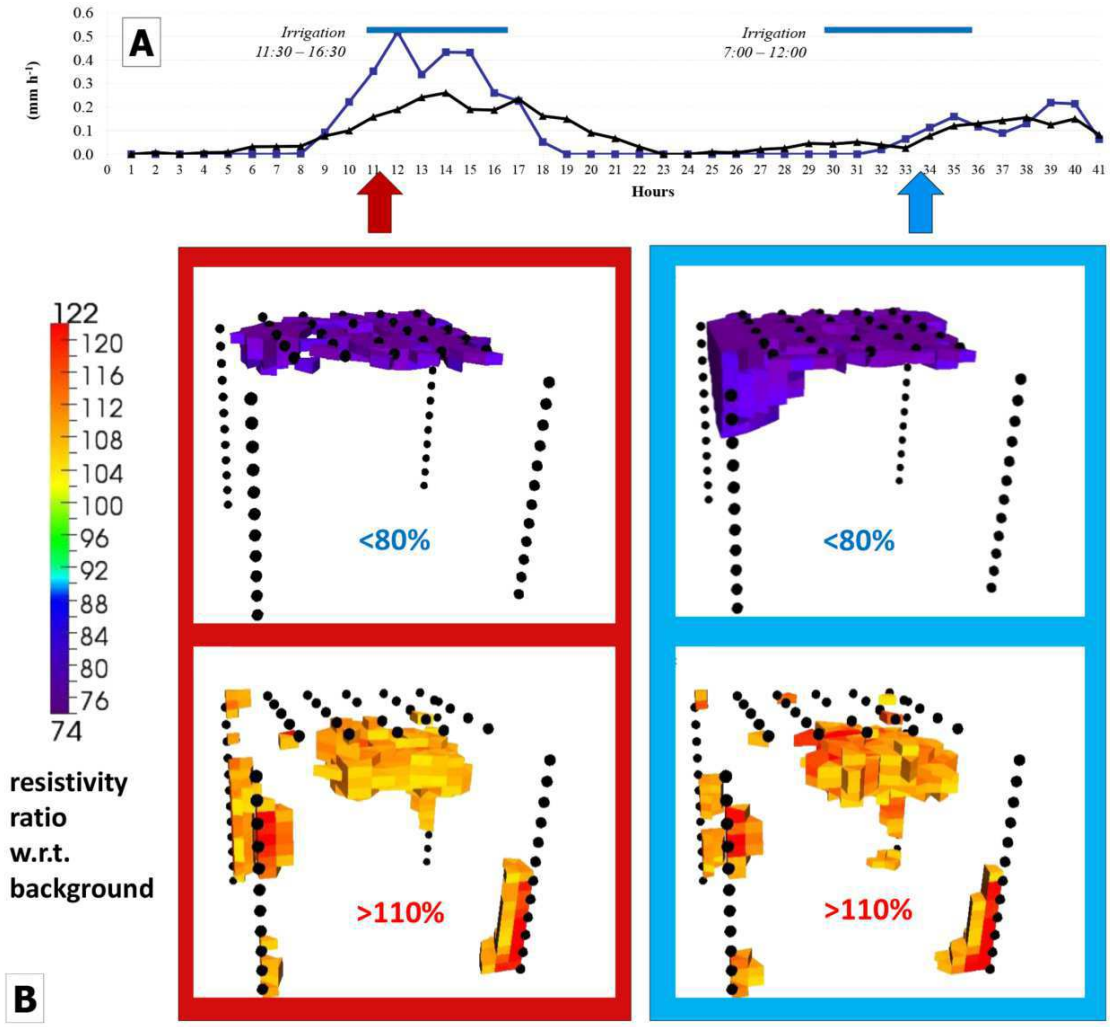

Fig. 3.5: (a) Variation of sap flow (black line) and EC–derived evapotranspiration (blue line) over time, from midnight of 2^{nd} October 2013. The light blue segments indicate the scheduled irrigation. Both sap flow and evapotranspiration are nomalized in millimeters, assuming an area of 20 m^2 pertaining to the considered tree. (b) Time–lapse inversion results of two selected times, with respect to the background condition. For clarity, the upper panels show the areas affected by a decrease in resistivity over time (i.e. resisitivity ratio <80%), while the lower ones show only the portions where resistivity increase (i.e. resistivity ratio >110%). Image taken from Cassiani et al. [2015].

decrease, which takes place in the upper 10–20 cm (i.e., resistivity ratio <80%) and (ii) resistivity increase, which, on the other hand, occurs at a depth between 20 and 40 cm (i.e., resistivity ratio >110%).

Fig. 3.5(a) represents the evolution of both sap flow (black line) and EC–derived evapotranspiration (blue line) during the ERT monitoring campaign. In particular, these values have been normalized in millimeters assuming an area of 20 m^2 pertaining to the tree subject to our geophysical measurements. If we focus on the first day (2^{nd} October 2013), the maximum sap flow and total evapotranspiration seem to occur during the irrigation phase. Actually, this is not true, as these two

phenomena are mainly driven by meteorogical forcing variables (e.g. temperature, humidity, and so on), if the amount of water provided is equal. This is more clear on the second day (3^{rd} October 2013), as the irrigation is moved up (from 7:00 to 12:00 LT), while sap flow and total evapotranspiration maxima occur slightly after.

During these first ERT measurements, the electrical conductivity of soil porewater and irrigation water was monitored as well and in both cases showed rather high values, of the order of 1300 μS cm^{-1}, which explain the relatively low resistivity characterizing this site (e.g. Fig. 3.4).

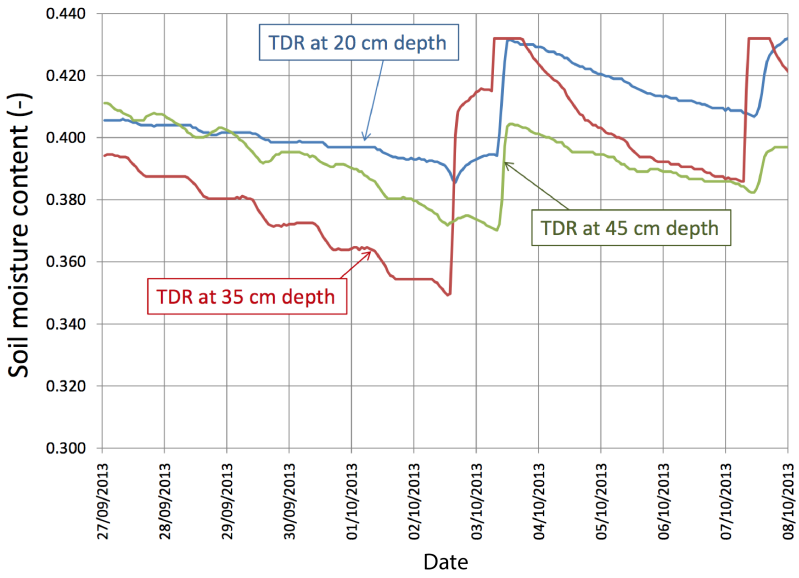

Fig. 3.6: Soil water content variations at Bulgherano field site measured by means of TDR probes located about 1.5 m from the monitored tree. The peak, well identified by all probes, is due to the irrigation experiment, which took place after to weeks of non–irrigation. Image taken from Cassiani et al. [2015].

Finally, also the soil water content was monitored by means of three TDR probes located at different depths (i.e. 0.20 m, 0.35 m, and 0.45 m below ground level), about 1.5 m far from the considered tree. As shown in Fig. 3.6, during the first days all probes show a certain decrease in soil water content (with pauses during the night), more pronounced on the TDR located 0.35 m below ground level (i.e. about the depth of the bottom of the RWU zone). On 2^{nd} October 2013, all probes show an increase in soil moisture content, which is due to the irrigation experiment that took place after two weeks of non–irrigation. This is particularly clear since these probes are located near a drip irrigator outside the monitored domain. In general, the moisture content is much higher than that measured in the ERT–controlled block. Likely, this is a consequence of the low (or absent) root water uptake outside the monitored domain. However, it is interesting to notice that all probes registered a decrease in soil water content from $3rd$ October 2013 till $7th$ October 2013, which can be considered as a consequence of the lateral movement of water put in place by the strong capillary forces exerted by the dry fine grained soil in the active root zone closer to the tree.

3.3.2 Dead orange tree

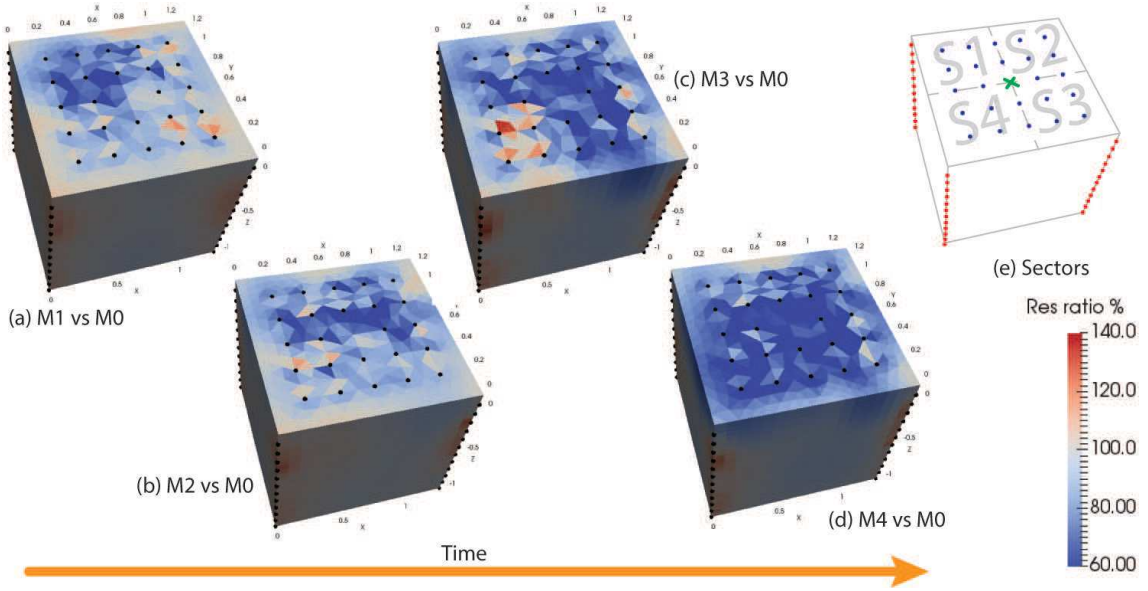

Fig. 3.7: Time–lapse inversion results of the irrigation test performed on 9^{th} June 2014 after the cut of the tree. M0, M1, M2, M3, and M4 are the acquisition labels, as described in Tab. 3.2. (a) Shows the variations with respect to the background (M0) after the irrigation of the first sector S1, (b) represents the variations are after the irrigation of the sector S2, (c) displays the variations after the irrigation of sector S3, and (d) shows the variations after the irrigation of the last sector, S4. (e) is a representation of the sector location provided for comparison (already shown in Fig. 3.2).

After the cut of the tree, we performed an irrigation test aimed at gathering information regarding the same portion of soil investigated before. The absence of the canopy avoids the occurrence of all the phenomena induced by the plant activity (in particular, transpiration and root water uptake). Furthermore, the root system has been left in place, as well as all the geophysical instrumentation, thus the soil has been left unaltered between October 2013 and June 2014.

Fig. 3.7 shows the results of the time–lapse inversion process, performed with the inversion error at 2% (as for the time–lapse inversion described in the previous section). In this case too, the steps followed to obtain these results are those described in subsec. 2.4.4. The variations in terms of resistivity are rather explanatory, as they clearly locate the different irrigated sectors during the test (i.e. S1, S2, S3, and S4), moving from Fig. 3.7(a) to Fig. 3.7(d). The infiltration test consisted in 25 l of water per sector, provided in ten minutes prior the beginning of the ERT measurement. The aim of this test is to obtain a dataset for the calibration of a hydrological model focused on representing the water infiltration plume, therefore we deemed not necessary monitoring the variation in electrical conductivity of the soil pore water, as practically only the infiltration timing matters. However, the water used for this infiltration test is the same water used during normal irrigation procedures.

3.4 Discussion

Given the possible influence due to the borehole placement, which may have disturbed the surrounding soil, we decided to concentrate our analyses and discussion only on the internal areas.

The ERT measurements that took place while the plant was active well show (both from the absolute and the time–lapse point of view) that the main activity occurs in the shallow part of the domain, within the first 0.4 m below ground level. The resistivity distribution resulting from the absolute inversion process (Fig. 3.4) is likely to be the consequence of the strong RWU taking place during summer, whose effects are intensified by the lack of irrigation in the 15 days prior to the ERT measurements. The higher resistivity (50 Ωm on average) can therefore be related to a rather dry soil, where the water content is reduced to a minimum by the plant activity. The time–lapse inversion results confirm the evidence of the absolute inversion, since all variations occur in the upper part of the domain as well. In particular, the decrease in resistivity over time takes place in both cases (i.e. at the two represented times, see Fig. 3.5) only in the first 20 cm below ground level. This decrease, however, is not as strong as expected, given the relatively high conductivity of the irrigation water (i.e. about 1300 μS cm^{-1}). This may be due to the RWU already occurring, which manages to limit the resistivity decrease down to only 20% of the background conditions. This strong root water uptake is also able to further increase resistivity at depths ranging between 0.2 m and 0.4 m, making the soil even drier.

This interpretation is consistent with evidences shown by Tenhunen et al. [2013], who stated that a decrease in soil water content may be an effect of the root water uptake. This reduction can be easily detected (also over a three–dimensional domain) as an increase in resistivity over time. However, to accept this assumption, it is necessary to exclude all other factors that may modify resistivity. In particular, the monitoring of porewater and irrigation water electrical conductivity allows us to conclude that the observed variations in resistivity over time are not influenced by porewater conductivity effects, as porewater and irrigation water have similar electrical conductivities. Furthermore, the small interval of time between the background ERT measurements and the other acquisitions (see Tab. 3.1) lets us to assume root growth negligible. Moreover, the effects of the presence of the root system on the resistivity patterns are eliminated thanks to the time–lapse approach (i.e. they can be considered constant over time, thus leading to a resistivity ratio of 100%).

The irrigation test performed after the cut of the tree provided a dataset particularly useful, as it gave information regarding the sole water infiltration, without any effects related to the orange tree. Cassiani et al. [2015] used the dataset to develop a one–dimensional model aimed at determining the extension of the active root zone. However, the combination of the two datasets (i.e. October 2013 and June 2014), is suitable also for a three–dimensional modeling, with particular reference to data assimilation techniques (e.g. Rossi et al. [2015]), which may exploit this dataset for calibration procedure.

4

Palazzelli field site: data acquisition and analysis

***

In this chapter I describe the Palazzelli case study, which comprises two orange trees located in an orange orchard in south–eastern Sicily. These plants are drip irrigated with two different treatments, full irrigation and partial root drying, which are aimed at better exploiting the available water resources. It is reasonable to assume that the different irrigation treatments lead to different root water uptake patterns, therefore this dataset is particularly suitable for comparing the effects of a deficit irrigation technique against full irrigation. This also plays a crucial role given the increasing application of deficit irrigation techniques, especially in those regions affected by semi–arid climates [Fereres and Soriano, 2007].

In our sicilian field site, we performed two different monitoring surveys, one ranging from June to September 2014 with acquisitions performed every month (called long–term monitoring), and the other focused on the variations occurring during the daily irrigation process (called short–term monitoring). Furthermore, also in this case study we combined electrical resistivity tomography and sap flow measurements. Therefore, our goals comprise: (i) studying the feasibility of root zone monitoring by time–lapse 3–D ERT at the small (decametric) scale, (ii) improving the identification of root–zone water dynamics by integrating ERT with transpiration sap flow data, and (iii) assessing the value of ERT data for a qualitative description of soil–plant–atmosphere interactions in two different irrigation treatments (i.e. full and deficit irrigation). Once again, we will assume that the increase (or decrease) of resistivity over time, with respect to a background condition, is due to a decrease (or increase) in soil water content. This strong assumption holds under specific circumstances (e.g. monitoring the modifications in electrical conductivity of the pore water and measuring temperature variations), first of all considering the root growth negligible in the short time considered during the short–term monitoring. On the other hand, the long–term monitoring is mainly focused on highlighting the resistivity patterns at the measurement time (i.e. absolute inversion).

The content of this chapter has been submitted for publication to the *Journal of Hydrology*:

Vanella D., Consoli S., Cassiani G., **Busato L.**, Boaga J., Barbagallo S., Binley A., 2016. The use of small–scale electrical resistivity tomography to identify trees root water uptake patterns. *Submitted*.

My contribution to this work concerns the analysis and inversion of the ERT data, with particular reference to the raw data analysis, the merging of the different datasets, the creation and assessment of the mesh, and finally the inversion *sensu stricto*.

4.1 Site description

The site chosen for this case study is an experimental orange orchard belonging to the Citrus and Mediterranean Crops Research Center of the Italian Council for Agricultural Reseacrh and Agricultural Economics Analyses (CRA–ACM, Acireale), located in Palazzelli (Lentini, SR, eastern Sicily – 37° 20' N, 14° 53' E) and planted with 8–year–old [*Citrus sinensis* (L.) Osbeck] cv "Tarocco Sciara" grafted on Carrizo citrange rootstock [*Poncirus trifoliata* (L.) Raf. × *C. sinensis* (L.) Osbeck].

Analyses of texture and bulk density were conducted at the experimental site.The soil is fairly uniform (in the top 0.1 m) and is classified as sandy–loam, with 69.7% of sand, 10.5% of clay, and 19.8% of silt, while 1.25% of the volume is made up of organic matter [Consoli et al., 2014]. Further analyses of texture and bulk density were conducted on soil samples collected at different depth (i.e. 0.2, 0.4 and 1.0 m). The bulk density is circa 1.32 g/cm^{-3} and the average water contents at field capacity (pF=2.5) and wilting point (pF=4.2) were 28% and 14%, respectively.

The orange trees composing this grove are spaced 6 m × 4 m, with mean leaf area index (LAI) equal to 4.5 m^{2}m^{-2} and mean photosynthetically active radiation (PAR) light interception of 75%. These plants undergo several agronomic practices, like fertilization (three times per year), pruning, harvesting, minimum tillage between rows, and weed control by herbicides [Consoli et al., 2014]. Given the constant water scarcity affecting Sicily and the need of improving water use efficiency, among all these agronomic operations, particular attention must be paid to the four irrigation treatments applied. In detail, the experimental field is subdivided into twelve blocks with an extent of circa 600 m^2 each. Every block is irrigated with one of the four irrigation treatments, thus each treatment is replicated three times in a randomized modality, and comprises 24 plants (three rows with 8 trees each). A representation of the irrigation randomized blocks is shown in Fig. 4.1. These treatments are based on crop evapotranspiration (ET$_c$), eventually adjusted by rainfall. ET$_c$ is obtained by multiplying the reference ET (ET$_0$, also known as evaporative demand of the atmosphere or reference evapotranspiration rate), obtained by the Penman–Monteith approach [Allen et al., 1998, 2006], by the seasonal crop coefficient (K$_c$) for orange orchard (i.e. 0.7 according to FAO–56). ET$_c$ is further adjusted for a reduction coefficient, which depends on the canopy size with respect to the area pertaining to each tree (within both row and line) in the field [Consoli et al., 2014]. From June to October 2015, irrigation was supplied three times per week, in the early morning. The different irrigation treatments consist of:

– T1: control treatment. The amount of water provided to each plant is equal to total evapotranspiration (ET$_c$), using two surface lateral pipes per row close

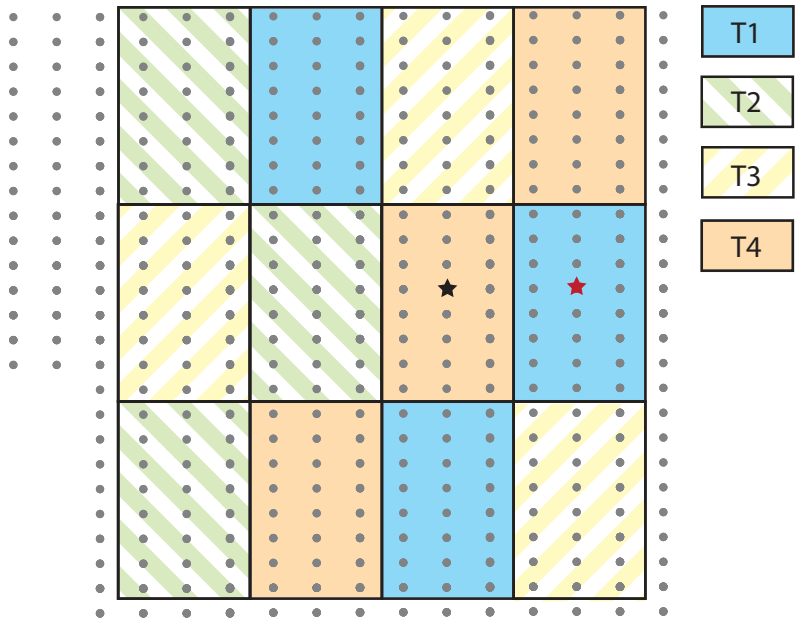

Fig. 4.1: Randomized block design of irrigation treatments at Palazzelli field site. T1, control treatment: trees are irrigated with an amount of water equal to 100% of total evapotranspiration; T2, a sustained deficit irrigation: trees are watered with 75% of total evapotranspiration; T3, regulated deficit irrigation: the amount of water per tree is equal to 50% or 100% of total evapotranspiration according to the phenological stage; T4, partial root drying treatment: each plant is irrigated with 50% of total evapotranspiration on one side of the tree (the other is kept dry). The black and red stars indicate the location of the two considered orange trees.

to the trunks. Each tree is drip irrigated thanks to six 4 l h^{-1} (i.e. 1 mm h^{-1}) emitters spaced 0.62 m;

- T2: sustained deficit irrigation treatment. Each tree is irrigated with 75% of total ET_c using buried lateral pipes emitting 6 l h^{-1} (subsurface drip irrigation);
- T3: regulated deficit irrigation treatment (RDI). The water supplied varies from 50% to 100% of total ET_c depending on crop phenological phases, while the irrigation apparatus is identical to T1;
- T4: partial root drying (PRD). The plants are watered with an amount of water equal to 50% of ET_c on the west side of the tree, while the east side is kept dry. Fortnightly, the dry and wet sides are switched. The irrigation pipe is located 0.35 m from the tree trunk and has the same features described for T1.

The water used for irrigation had medium salinity ($EC_{25°C}$ of 2.02 dS m^{-1}), pH equal to 7.30, and alkaline reaction. At the end of the 2015 irrigation season, the total amount of water supplied by the control treatment (T1) was equal to 266.4 mm, while T4 provided 158.2 mm, with a percentage of water saving of about 41%.

The CRA–ACM orchard is equipped with an automated meteorological station surrounded by grass, which measures and logs global radiation, relative humidity,

wind speed and direction, and air temperature on hourly basis. The climate is semi–arid, with warm and dry summers and wet winters. From June to October 2015 the total rainfall was 100 mm (from a few episodic events), ET_0 was 697 mm, the average daily temperature was 25 °C (± 5.8 °C), and the mean relative humidity was 70% (± 26%). The maximum daily temperature reached peaks of 40 °C.

The dynamics of soil water content (SWC, $m^3\ m^{-3}$) distribution were monitored using soil moisture sensors (ECH_2O probe, Decagon, Inc.) calibrated against the gravimetric method. Sensors were installed at a depth of 0.3 m from the soil surface. In the T4 treatment, soil moisture probes were installed at both eastern and western side of the trees trunk to provide information on water dynamics of the two sides of the root–zone system.

At the experimental site, the soil temperature was measured by soil thermocouple probes (TVAC, Campbell Sci.) located at 0.1 and 0.8 m below ground level. The soil temperature variation was, on average, 2 °C during the ERT acquisitions period (June–October 2015). Considering that the electrical resistivity is influenced only by 2% from temperature changes of 1°C [Friedman, 2005], in our case the temperature effect was neglected because it was low compared to SWC induced changes [Nijland et al., 2010].

4.2 Data acquisition and analysis

For our measurements, we considered two orange trees, one fully irrigated and one located in a block where PRD is applied (see the red and black stars in Fig. 4.1, respectively).

4.2.1 Tree transpiration measurements

As described in the previous case study, also here sap flow is measured by means of the HPV technique. A 4 cm sap flow probe with two ultra–thin thermocouples embedded (Tranzflo NZ Ltd., Palmerston North, NZ) was inserted on the southern side of each trunk, at 0.2 m from the ground, and wired to a data–logger (CR1000, Campbell Sci., USA). Thus, the thermocouples are located 5 mm and 15 mm into the trunk. The sampling interval was 30 minutes and the measurements lasted the whole ERT acquisition period. Also in this case, the data thus obtained have been processed according to Green et al. [2003].

4.2.2 Small–scale 3–D ERT acquisitions

The monitoring of the root zone activity is carried out by means of small–scale 3–D electrical resistivity tomography. For each tree we applied the instrumentation set–up represented in Fig. 4.2, which is based on previously tested schemes (see e.g., Boaga et al. [2013] and chap. 3) and comprises both superficial and borehole electrodes. More in detail, we took advantage of nine micro–boreholes equipped with 12 electrodes each, made up of stainless steel bands wrapped around a plastic pipe and spaced 0.10 m (i.e. till a depth of 1.2 m). These boreholes pinpoint the edges of four squares of side 1.3 m (named C1–C2–C3–C4 and Q1–Q2–Q3–Q4 for T1

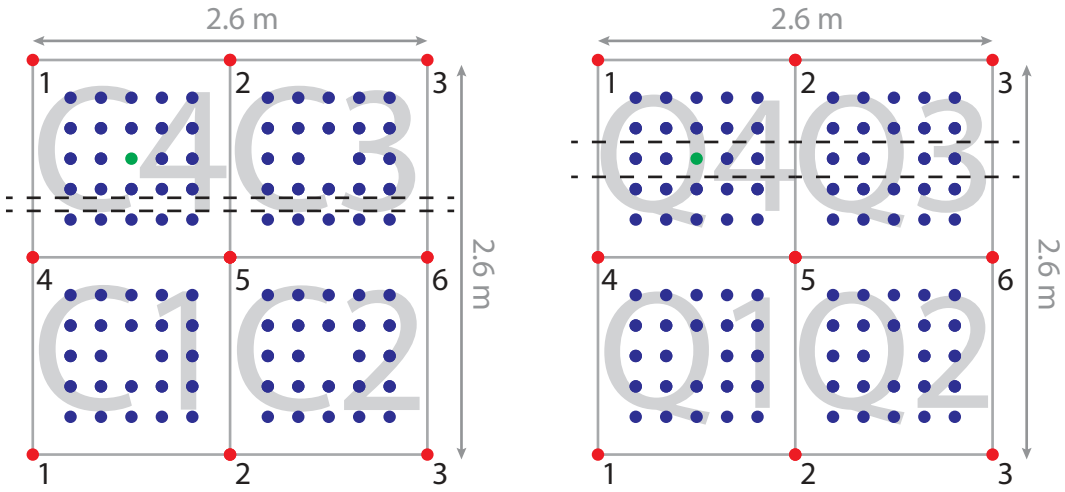

(a) Treatment T1 (b) Treatment T4

Fig. 4.2: Electrodes layout for (a) control treatment T1 and (b) PRD treatment T4 . Each set–up comprises four quadrants, with 96 superficial electrodes and 108 borehole electrodes. The red circles indicate the position of each borehole, the blue circles locate the superficial electrodes, and the green circles pinpoint the orange trees. The black dashed lines correspond to the irrigation pipe lines, depending on the different treatments (T1 and T4).

and T4, respectively, see Fig. 4.2), one of which is centered on the orange tree (C4 for T1 and Q4 for T4). Each square is equipped with 24 stainless steel electrodes covering a superficial grid of 0.26 m spacing. Thus, our instrumentation as a whole comprises 108 borehole electrodes and 96 superficial electrodes. A three–dimensional representation of the instrumentation set–up is shown in Fig. 4.3.

To better detect root water uptake patterns in our monitored root zones, we carried out both long–term and short–term monitoring, from June to September 2015. The ERT long–term monitoring comprises measurements taken before the irrigation period (ERT1, June 8^{th}–10^{th}), one month after the beginning of the irrigation (ERT2, July 14^{th}–17^{th}), and at the end of the irrigation season (ERT3, September 21^{st}–24^{th}). In this case, for each orange tree we considered all four quarters. On the contrary, the short–term monitoring is focused only on C4 and Q4, i.e. the quarters containing the trees. In fact, even if we acquired our ERT datasets before and after irrigation on all sectors for both trees, only C4 and Q4 have been considered for measurements during the scheduled irrigation. So, since these latter measurements are focused on the irrigation process, they took place on a hourly basis only during ERT2 and ERT3. A summary of all 48 acquisitions can be found in Tab. 4.1

Each survey was carried out using a SYSCAL Pro resistivity meter (IRIS Instruments) with the following parameters:

– Ten–channel receiver;

– Pulse duration of 250 ms;

– Potential reading at 50 mV;

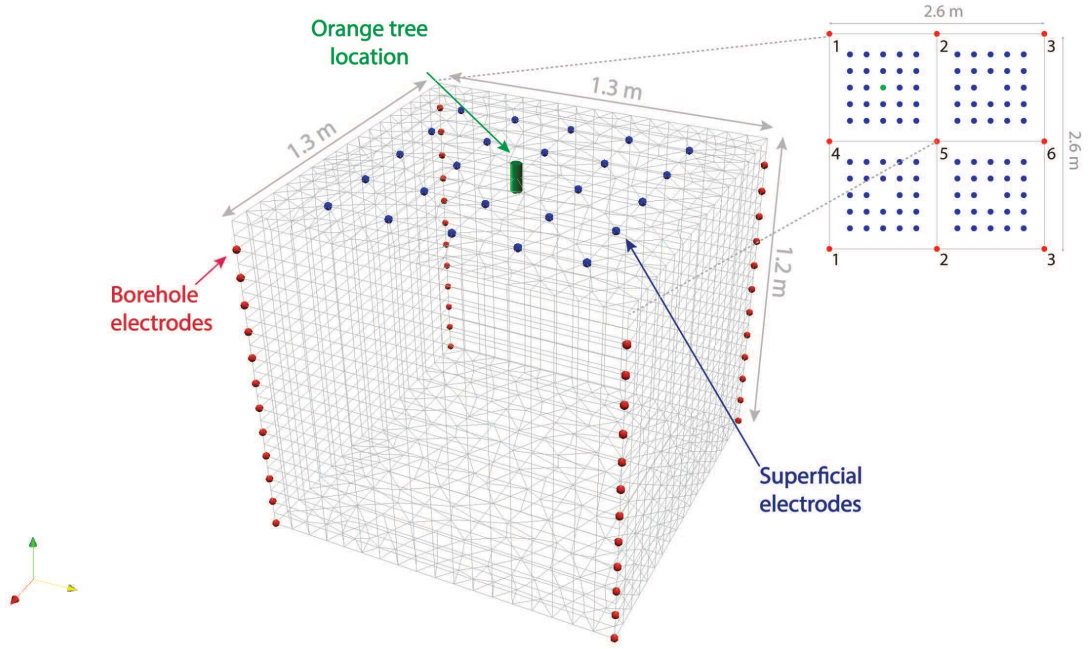

Fig. 4.3: Example of rectangular parallelepiped defined by four micro–boreholes and 24 superficial electrodes, in blue (plant sector). Each micro–borehole hosts 12 stainless steel electrodes, in red (i.e., 48 electrodes for each rectangular parallelepiped). The green cylinder indicates the location of the tree. The set-up is the same for both plants.

We adopted a complete dipole–dipole skip–0 scheme, which shares all the features described in the previous case study. The sequence used includes 72 electrodes (i.e. one quarter at a time) and 4885 measurements, optimized combining direct and reciprocal measurements with dummy–quadrupoles (see subsec. 3.2.2). Prior to each acquisition, the contact resistances were tested to check their suitability to inject current and to measure potential differences. This preliminary step showed that almost all electrodes had a good contact with the ground, even when the soil was relatively dry. Each acquisition lasted 25 minutes.

During this ERT monitoring, also the soil pore solution was sampled, thanks to ceramic suction lysimeters (Soil Solution Access Tube, SSAT by IRROMETER Company, Inc.) located 0.30 m below ground surface. The electrical conductivity of the pore water was measured in laboratory by means of a conductivity meter (HD2106.2, delta OHM Italy). The electrical conductivity of the irrigation water was monitored as well.

4.2.3 Inversion of the ERT data

After removing all the measurements pairs (direct and reciprocal) with an error higher than the fixed threshold (see subsec. 2.4.1), we determined the geometric factor of each quadrupole to delete those with unsuitable values (e.g. infinite or not–a–number). Then, all electrodes have been renumbered in order to combine the acquisitions on different quarters into the same mesh, considering also that

	Treatment T1			Treatment T4		
	ERT1	ERT2	ERT3	ERT1	ERT2	ERT3
Time00 (pre–irrigation)	C1, C2 C3, C4	C1, C2 C3, C4	C1, C2 C3, C4	C1, C2 C3, C4	C1, C2 C3, C4	C1, C2 C3, C4
Time01 (during irrigation)		C4	C4		C4	C4
Time02 (during irrigation)		C4	C4		C4	C4
Time03 (post–irrigation)		C1, C2 C3, C4	C1, C2 C3, C4		C1, C2 C3, C4	C1, C2 C3, C4

Tab. 4.1: Summary of ERT measurements at Palazzelli site for both treatments and both types of monitoring (i.e. long–term and short–term). C4 and Q4 are the sectors containing the orange trees. The whole dataset comprises 48 acquisitions.

some boreholes are shared among neighboring sectors. This also allowed checking and averaging duplicates, i.e. measurements that are present in adjacent sectors. Subsequently, particular attention has been paid to the mesh construction and to the evaluation of the model error of the forward solution. To do this, several unstructured tetrahedral meshes were generated using Gmsh software [Geuzaine and Remacle, 2009]. We chose this type of mesh, instead of structured triangle prism discretization, for their capacity to enhance computational efficiency and for the facilitation of refining grids within distinct regions (outer and inner zones). The mesh choice is based on the assessment of the forward model error and on the forward model performance in terms of computation time. In particular, the forward model percent error E_{fw} was calculated as

$$E_{fw} = \frac{\rho_a - \rho_m}{\rho_a} \cdot 100 \tag{4.1}$$

where ρ_m is the resistivity distribution output from the forward model and ρ_a is equal to 100 Ωm on the whole domain. The selected mesh is composed of two zones, the inner zone (with 57.000 tetrahedral elements and 10.527 nodes), and the outer zone (with 79.529 tetrahedral elements and 12.551 nodes).

The next step consisted in the inversion *sensu stricto*. As already described in sec. 3.3 for the previous case study, also for the Palazzelli site it is possible to take advantage of both absolute and time–lapse inversions. Thus, first of all, we inverted alla quarters together, when available (see Tab. 4.1), with error level fixed at 10% and 16%. Then, we applied the principles described in subsec. 2.4.4 for the time–lapse inversion. Firstly, we considered all sectors together, assuming the acquisition prior to the beginning of irrigation as background measurement. Here we fixed the error level at 10%. Secondly, we focused only on the quarters containing the trees (C4 and Q4, Fig. 4.2), where also measurements during the irrigation are available (Tab. 4.1). The background condition corresponds to the measurement taken before the beginning of the irrigation and the error level is fixed at 5%.

We performed both forward model error assessment and ERT data inversion

thanks to R3t code [Binley, 2013].

4.3 Results

4.3.1 Soil moisture dynamics during the monitoring campaign

In conjunction with our ERT measurements, also laboratory analyses of both soil pore solution and irrigation water took place. For this site, the results show a moderate salinity, with $EC_{25°C}$ values in the range of 2–3 dS m^{-1}. The observed variability of electrical conductivity should not cause major alterations in the ERT monitoring, thus resistivity variations can be considered as mainly related to changes in SWC. Additionally, also daily average transpiration fluxes have been measured, reaching 1.9 mm d^{-1} for T1 and 0.9 mm d^{-1} for T4, compared to a rate of ET_c of 2.1 mm d^{-1}. During the hottest daily hours (i.e., from 12:00 a.m. to 04:00 p.m. LST), sap flow fluxes were fairly steady due to tree capacitance and physiological control mechanisms [Motisi et al., 2012].

The variation of soil water content over time is shown in Fig. 4.4 and is compared against field capacity (0.28 m^3 m^{-3}), wilting point (0.14 m^3 m^{-3}) , rainfall, and irrigation rates. Furthermore, also the ERT measurement times are indicated. Regarding T1 (i.e. the control treatment – curve with green triangles), the SWC is rather constant during the considered period and close to field capacity, except for the first 5–6 days, when it was closer to the wilting point. On the contrary, the variation of SWC in T4 is characterized by an alternating trend on both probes (curve with yellow triangles for the eastern probe and curve with orange triangles for the western probe), thus perfectly agreeing with the drying–and–wetting cycle typical of the PRD treatment (see sec. 4.1). In particular, during ERT1 the soil water content was well below the filed capacity in both treatments, even if a rainfall event of 23 mm (i.e. effective rainfall) occurred on DOY (day of the year) 160, allowing an increase of the SWC. During ERT2, the SWC remained fairly close to field capacity in T1 and slightly lower than this on the T4 west side, while SWC on the east side remained fairly steady and slightly higher than the permanent wilting point (as expected). Finally, during ERT3, the condition was opposed to that described for T4 during ERT2, while T1 still presented a high SWC.

4.3.2 Long–term ERT monitoring

The ERT dataset acquired during the long–term monitoring were analyzed in absolute terms (i.e. considering one dataset only at the time). Even if the average reciprocal errors for the whole quarters in T1 and T4 were respectively of 2.6% (±1%) and 2.9% (±0.9%) (i.e. rather low), the assumed data error in the inversion procedure varied from 10% to 16%. In fact, most inversions converged after an acceptable number of iterations (i.e. 6–8) with the error fixed at 10%. Nevertheless, in some cases the error has been increased up to 16% in order to get smoother images or, in other words, to reduce the spacial variability of resistivity in our sections.

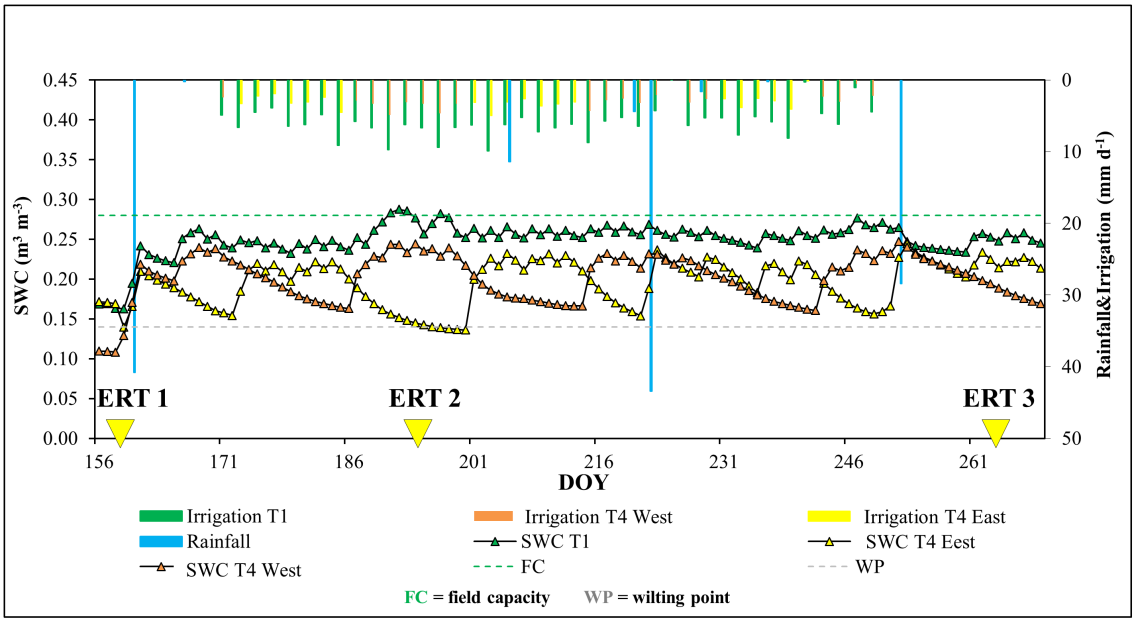

Fig. 4.4: Soil water content variations over time for both treatments T1 and T4, measured by means of soil moisture sensors located at a depth of 0.3 m below ground level. The values are compared against field capacity, wilting point, rainfall, and irrigation rates.

With this higher error, most dataset converged in less than 5 iterations. Finally, the computational time increased with the number of quadrupoles, which grows from ERT1 to ERT3, probably because the electrodes–soil contacts improved during the irrigation season due soil settling around the boreholes.

Fig. 4.5(a) and Fig. 4.5(b) show the results of these first inversions for T1 and T4, respectively. In particular, these cross–sections show the resistivity distribution at different depths for the background dataset (i.e. initial condition) collected during ERT1, ERT2 and ERT3. These images well show different spatial and temporal patterns of ρ. Since soil textures at the investigated layers in T1 and T4 results quite homogeneous, with a prevalent sandy–loam composition (see sec. 4.1), the observed electrical resistivity variations should depend, for the most part, on changes in soil water content that are caused by a combination of irrigation and root water uptake dynamics. However, it is important to underline that it is not possible to discern the effects of the root system from those related only to SWC spatial variations on the resistivity distribution. This is a strong limit of the ERT absolute inversion, which can be overcome by integrating other information regarding the root system (e.g. previous knowledge on the whole root system extension from other orange trees removed from the soil). Unfortunately, this type of information is not directly available for this case study, even if it is reasonable to assume a rather shallow root distribution, as seen, e.g. in chap. 3.

If we focus on ERT1 in both treatments, it is possible to notice that it is characterized by higher resistivity with respect to ERT2 and ERT3, especially at depth bigger than 0.4 m. These high–resistivity areas are progressively smeared and reduced in magnitude as a consequence of the irrigation process. Nevertheless, these

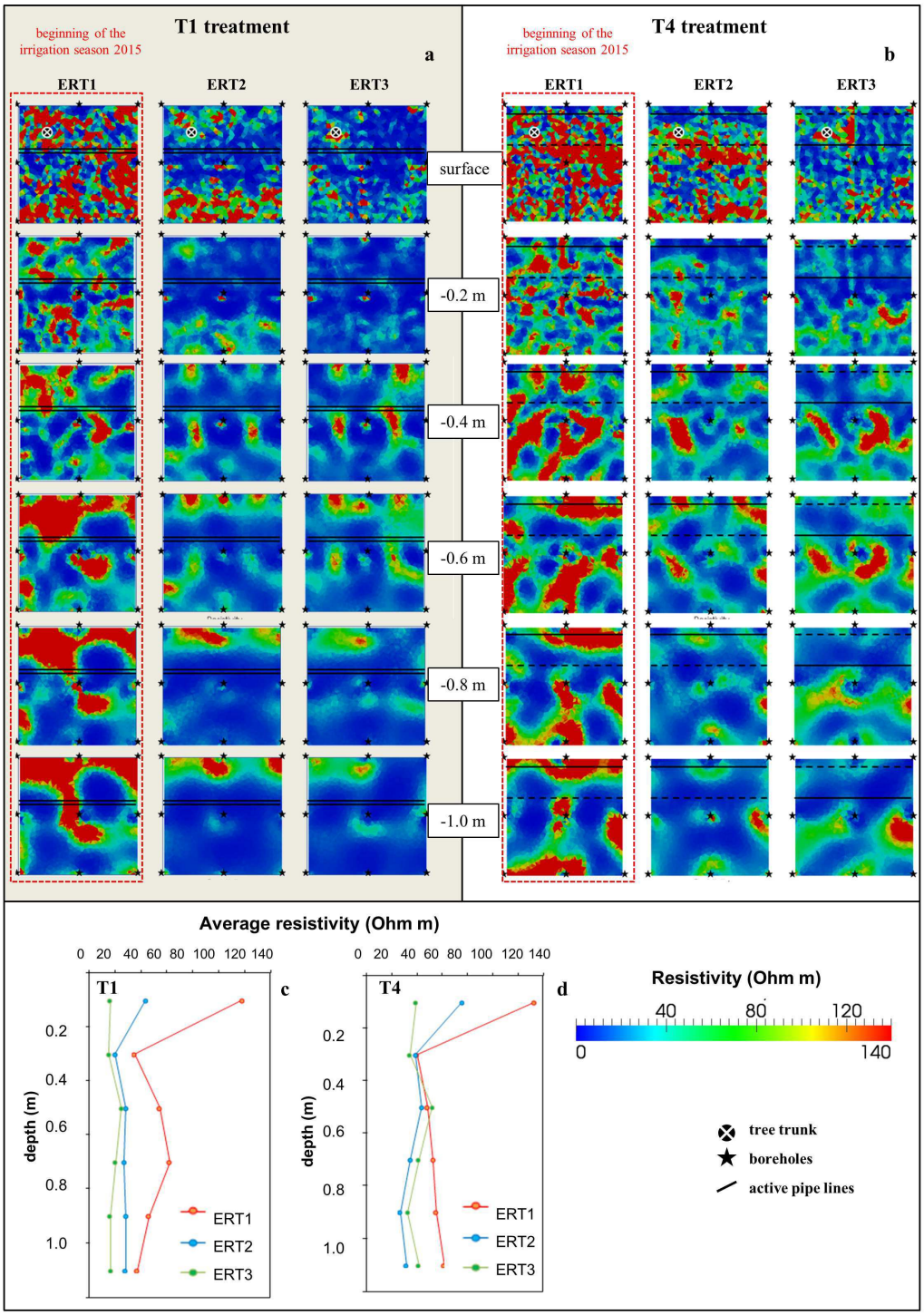

Fig. 4.5: Absolute inversions of background acquisitions collected during the long–term monitoring at Palazzelli field site: (a) full irrigation, T1, and (b) partial root drying, T4. Subfigures (c) and (d) show how average resistivity varies with depth, for T1 and T4, respectively. The black lines represent the irrigation pipes (if the line is dashed, the pipe is not active).

features are not erased in the following time steps and maintain their general structure. If compared to the electrical conductivity of pore water (see sec. 4.1), the

resistivity of these domains can be considered as relatively high (>100 Ωm). So it is plausible to assume that these areas are related to strong unsaturated conditions. How such very resistive features can exist at localized locations at depth is not easy to explain if not calling into play local RWU that would reasonably be intense at depth during the long period of time (November to May), when the crops are not irrigated.

In addition, resistivity has been averaged along z, in order to obtain the profiles represented in Fig. 4.5(c), for T1, and Fig. 4.5(d), for T4. These profiles show more clearly the average decrease in resistivity taking place from June (ERT1) to October (ERT3) 2015. In particular, the greatest variations belong to the upper part of the soil, where mean resistivity values vary from 118 to 16 Ωm in T1 and from 139 to 39 Ωm in T4. This is most likely due to the adopted superficial micro–irrigation system and in the case of T4 (PRD) also due to the irrigation shift between either sides of the plant root system.

4.3.3 Short–term ERT monitoring

Fig. 4.6 displays the results of the inversion process in terms of resistivity ratio (in %) considering all sectors together, where 100% indicates that resistivity is equal to that in the background condition, values >100% show an increase in resistivity, while values <100% indicate a decrease in resistivity over time (see subsec. 2.4.4). For a comparison, the background is showed in Fig. 4.5.

The resistivity variations in these cross–sections highlight complex patterns that are the result of the interacting processing occurring in the domain of interest, i.e. the infiltration of the irrigation water and the soil drying due to root water uptake. It is important to underline that what is shown in Fig. 4.6 is the result of the cumulative effects of irrigation and evapotranspiration occurred in the entire time–lapse, therefore it is rather difficult, if not impossible, to identify the contribution of the single processes. Moreover, the root growth con be considered negligible in the short amount of time considered (i.e. on a daily base). Hence, only a qualitative description is achievable. Nevertheless, it is possible to identify some clear phenomena:

- Resistivity tends to decrease in specific areas of the domain, i.e. in correspondence of the drippers and below them, creating very consistent patterns extending from the surface to the bottom of the monitored soil volume (approximately 1 m below ground);

- Other areas, on the contrary, experience an increase in resistivity over time. This is likely related to the evapotranspiration taking place, since during the hottest days it exceeds the amount of irrigated water. As a consequence, soil water content is likely to be lower in the afternoon with respect to the early morning situation. The same was observed e.g. by Cassiani et al. [2015], also in an orange orchard. It is important to underline that some resistivity increasing areas are located at depth, in correspondence of the deepest roots. This is more evident comparing the areas with higher absolute resistivity in

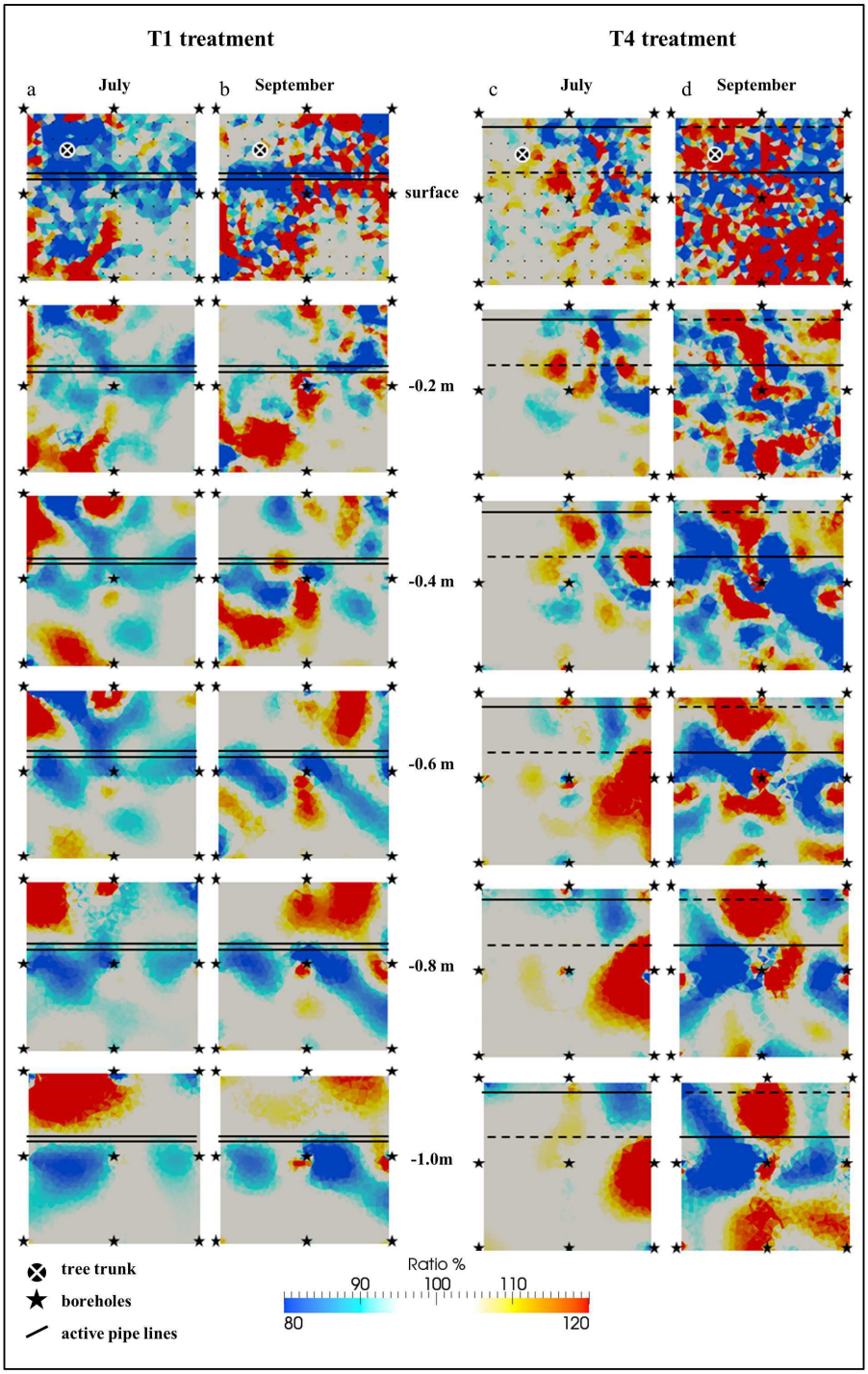

Fig. 4.6: Time–lapse inversions on all sectors of both trees, collected during the short–term monitoring at the Palazzelli field site. For the two considered treatments, T1 and T4, July and September results are shown ((a), (b) for T1 and (c),(d) for T4, respectively). These cross–sections display how resistivity has varied after the end of the irrigation with respect to the background condition.

Fig. 4.5 (ERT1) with the portions with increasing resistitivity over time in Fig. 4.6;

– As described in sec. 4.1, the quantity of water provided to each tree varies according to the different treatments. In particular, the amount of water used in T1 is higher than in T4 (i.e. 100% ET_c vs 50% ET_c, respectively). As a consequence, the decrease in resistivity in T1 is more evident, with respect to T4. This is more visible in July, when apparently the amount of water irrigated in T4 was totally transpired nearly at all depth.

Sectors containing the trees

As described before, the short–term monitoring is aimed also at exploring more in detail the sectors containing the tree, i.e. C4 for T1 and Q4 for T4 (see Tab. 4.1). In fact, comparing only pre– and post–irrigation conditions limits the amount of information regarding the cumulative changes occurred during the irrigation/evapotranspiration time. On the contrary, more frequent measurements, albeit limited to one sector, should lead to a better understanding of the occurring phenomena.

The results of the time–lapse inversions for sector C4, treatment T1, are displayed in Fig. 4.7. Here, all tree times (inverted with respect to the background condition) are represented. More in detail, Fig. 4.7(a) refers to 36 minutes after the beginning of the irrigation, Fig. 4.7(b) shows the variations 89 minutes after the beginning of the irrigation, and Fig. 4.7(c) represents the changes at the end of the irrigation, 236 minutes after its beginning. These measurements took place on July 15^{th} 2015.

As time increases and irrigation takes place (from Fig. 4.7(a) to Fig. 4.7(c)), a decrease in resistivity occurs with respect to the initial condition, as an effect of the soil wetting caused by the infiltration front. At the beginning, this decrease is more pronounced in the upper part of the domain, near the irrigation lines, and at the end reaches a depth of 1.2 m below ground level. Specifically, at Time01 the decrease in resistivity involves 4% of the whole monitored volume and at time 02 affects 10% of the same volume. On the contrary, after the end of irrigation (time 03, 4.7(c)), 7% of the whole C4 volume shows a resistivity increase. The maximum increase in resistivity is observed from 0.60 to 0.80 m depth of the soil profile, where the most root activity is expected to make the soil drier. At the same time, the RWU rate was at a maximum, as observed by the transpiration fluxes (Fig. 4.7(d)).

If we move to sector Q4 (treatment T4), we can see that the investigated domain shares the same features described above (Fig. 4.8). The results here represented correspond to the measurement campaign carried out on September 24^{th} 2015 and comprise three acquisition times as well, in addition to the background measure: Time01 (Fig. 4.8(a)), taken 47 minutes after the beginning of irrigation, Time02 (Fig. 4.8(b)), measured 93 minutes after the beginning of irrigation, and Time03 (Fig. 4.8(c)), acquired at the end of the irrigation, 283 minutes after its beginning. The infiltration of the water plume is highlighted by the decrease in resistivity occurring below the active irrigation pipeline. Here, the volume involved is smaller if compared to C4, as the amount of water is considerably lower (see sec. 4.1). Furthermore, also the regions where resistivity increases are close to the irrigation lines, and both are located in the upper part of the soil (0.0–0.4 m below ground level). More in detail, at Time01 the decrease in resistivity involves 5% of the upper 0.4 m of the domain, while at Time02 affects 13% of the same volume. After the end of

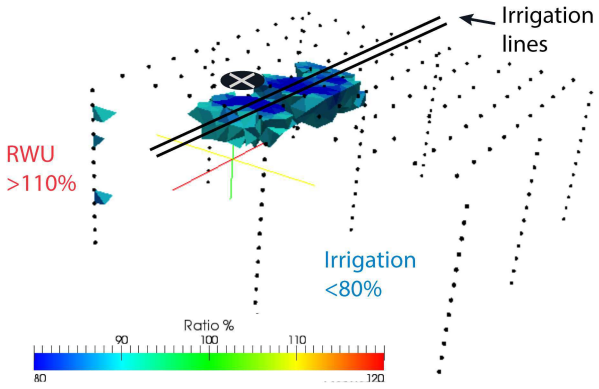

(a) Time01 vs Time 00

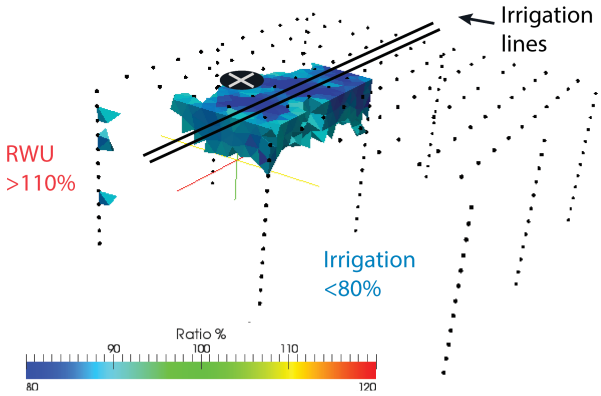

(b) Time02 vs Time00

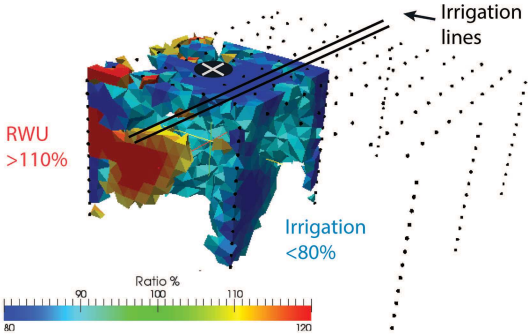

(c) Time03 vs Time00

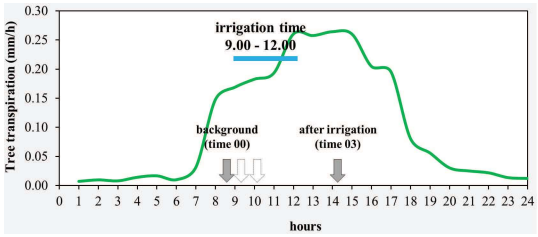

(d) Tree transpiration rate

Fig. 4.7: Time–lapse ERT results on C4 (treatment T1): (a) Time01 vs Time 00, (b) Time02 vs Time00, and (c) Time03 vs Time00. Time01 is acquired 36 minutes after the beginning of irrigation, Time02 after 89 minutes, and Time03 after 236 minutes. Panel (d) shows tree transpiration rate (mm h^{-1}), irrigation and ERT surveys timing in function of time. The black circle with the cross locates the tree.

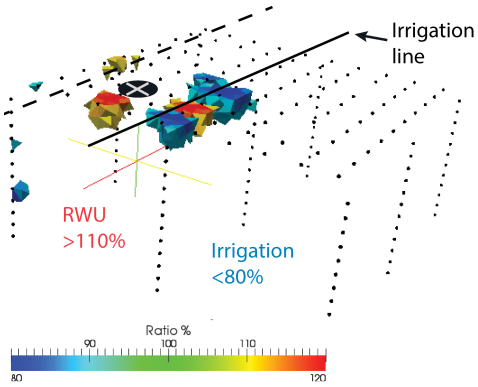

(a) Time01 vs Time 00

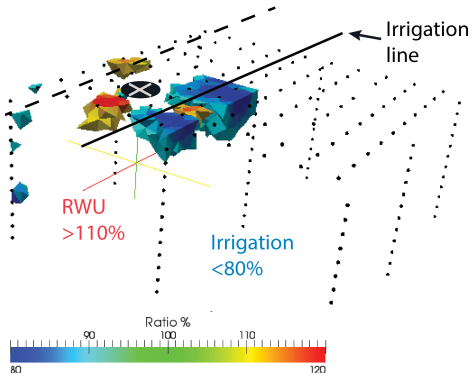

(b) Time02 vs Time00

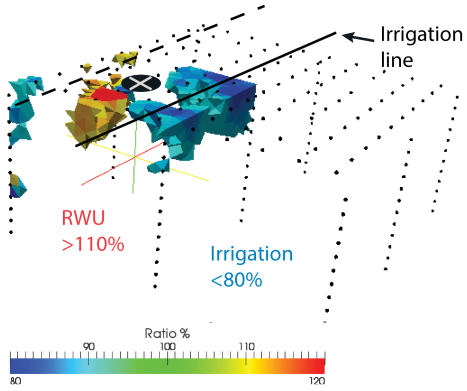

(c) Time03 vs Time00

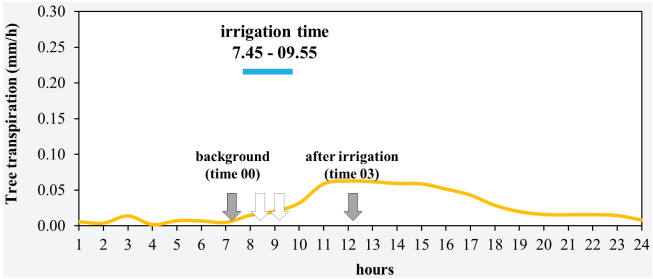

(d) Tree transpiration rate

Fig. 4.8: Time–lapse ERT results on Q4 (treatment T4): (a) Time01 vs Time 00, (b) Time02 vs Time00, and (c) Time03 vs Time00. Time01 is acquired 47 minutes after the beginning of irrigation, Time02 after 93 minutes, and Time03 after 283 minutes. Panel (d) shows tree transpiration rate (mm h^{-1}), irrigation and ERT surveys timing in function of time. The black circle with the cross locates the tree.

irrigation (Time03, 4.8(c)), 3% of the upper part of sector Q4 shows a resistivity increase that can be correlated to root water uptake, since also here the measurement time corresponds to the transpiration maximum. However, ET is lower than in the previous case, as expected (compare Fig. 4.7(d) and Fig. 4.8(d)).

4.4 Discussion

Orange trees irrigated by micro–irrigation tend to have a shallow root system [Department of Agriculture and Food, Government of Western Australia, 2016]. In particular, sweet orange [*Citrus sinensis* (L.) Pers.] cv. Mosambi aged 8 years budded on Rangpur lime (C. *limonia* Osbeck) has bulk active roots (70-90%) located in the top 0.3 m soil during different seasons, while the maximum root activity (65-81%) is confined to radial distance of 1.2 m [Kotur and Keshava Murthy, 1998].

Some authors (e.g., al Hagrey [2007]; Amato et al. [2010]; Rossi et al. [2011]) associated areas of larger resistivity with trees roots location, since plant cells are poor conductors of electric current. So, from a wider point of view, rooted soil may be viewed as a complex of conductive soil volumes interacting with a resistive matrix, which is continuous and branched, and may be able to redirect the slow–down electrical charges because of its spatial arrangement more than to the actual occupied volume [Mancuso, 2011]. Amato et al. [2008] gave a more quantitative approach for the study of the distribution of woody roots, showing how the resistivity of a rooted soil can increase of several hundreds of Ωm. Furthermore, this author also demonstrated that even low density herbaceous roots can increase the resistivity distribution, even if this effect is comparable to that of variations in grain size or water content [Amato et al., 2009]. However, this last effect is likely to be predominant at our site.

Tenhunen et al. [2013] stated that a reduction of soil water content may be considered as an indicator of the root activity. Therefore, it is possible to indicate the observed increase in resistivity as an effect of both evaporation and root water uptake in the short–term monitoring. It is reasonable to assume evaporation as a rather superficial process that does not affect the lowest part of the domain investigated by means of ERT. As a consequence, water depletion from subsurface soil layers can be attributed to root activity. Furthermore, changes in the intensity of RWU and its pattern of distribution are caused by variations in water content in the soil profile and shoot–growth activity [Kotur and Keshava Murthy, 1998]. Hence, the variations highlighted both in absolute and in relative terms (Fig. 4.5, 4.6, 4.7, and 4.8) could be related to the different responses of the active roots as a function of irrigation operations (timing and regime).

As already mentioned, the interpretation of our ERT results is not so straightforward. Attention must be paid to variations in temperature and pore water conductivity, as they affect the measured bulk resistivity (see e.g. Ursino et al. [2014]). Thanks to the continuous monitoring carried out during the ERT campaign, it is possible to attribute the temporal and spatial resistivity patterns to variations in soil water content, since pore water conductivity showed quite stable values. Furthermore, our measurements took place at the same hour, so also the effects of

temperature are negligible.

Finally, a quantitative analysis aimed at turning resistivity variations into SWC changes is possible, e.g. using classical Archie's law [Archie, 1942] or more general empirical relationships (e.g. Waxman and Smits [1968]; Brovelli and Cassiani [2011]. But if also the location of the active root zone is required, one should take advantage of a more complicated approach, which is based on hydrological modeling, where all the available information can be merged (see chap. 5 and chap. 6).

5

Numerical procedures for the localization of the active root zone

***

5.1 Introduction

In the second part of this dissertation, we develop a numerical approach for the estimation of the spatial and temporal distribution of the active root zone (i.e. the part of the root system performing root water uptake) on the basis of ERT measurements analogous to those described in the previous chapters.

The development of the root system is a process driven by different factors, which can be subdivided into two main groups [Schiefelbein and Benfey, 1991]: (i) internal, basically related to plant genetics and (ii) environmental, comprising all the external forcings from atmosphere and pedosphere. Even if the internal factors regulate the main aspects of root morphology (e.g. root hair, root cap, root diameter, etc. [Lynch, 1995]), the main influencers of root architecture and distribution are actually the environmental stressors, including gravity, adjacent roots, temperature, and aeration [Schiefelbein and Benfey, 1991]. Among all these external agents, a crucial role is played by water and nutrient availability [Lynch, 1995], since root density tends to expand where the available mass of nitrates and phosphates, as well as water, are higher [Schiefelbein and Benfey, 1991]. Anyhow, all these adaptations are mainly a consequence of the plant transpiration demand [Lambers et al., 2008b], which is ultimately regulated by meteorological and atmospheric components [Nilson and Assmann, 2007]. From a wider point of view, it is possible to consider these actions as optimization processes aimed at reducing energy waste, while balancing resource exploitation and transpiration needs [Chapin et al., 1987]. We may assume that the adaptation of the root system to the local environmental states proceeds by developing root hair, which are energetically optimal as they maximize the ratio between allocated root biomass and root surface available for the osmotic exchange with the surrounding soil. However, root hair is extremely difficult, if not impossible, to observe experimentally. For this reason, instead of looking at single roots, we look at root density distributions, an approach which is consistent also with Darcy's law (i.e. from a "macroscale" point of view), which governs water flow in soils. Thus the goal here is to identify the dynamical behavior of the root density in space by

means of ERT measurement.

The numerical procedure that we introduce is based on the optimality processes described above. However, some simplifications still need to be accounted for. The orange tree we are considering is assumed to be an adult plant, whose transpiration is driven and maximized mainly by atmospheric forcings, as the amount of nutrients and soil water content are supposed to be sufficient to avoid stress in the plant. All water uptaken by roots is transpired by the tree, since no water storage is taking place within the plant system. Additionally, the main energy losses occur in the soil and at the soil–root interface, so as to ignore all other energy losses affecting the plant system (e.g. due to the movement of water in the trunk). Finally, it is reasonable to assume that the root mass variation is negligible in the short time considered. It is important to underline that these strong assumptions do not fully represent the typical conditions in the field. Nevertheless, it is necessary to rely on them in this phase, so as to simplify the numerical procedure in this first development.

The application of electrical resistivity tomography for the characterization of the root zone is described by several examples in literature, as mentioned in the previous chapters. Its peculiar advantage is the capability of detecting variations in water content, whose decrease can be considered in our case as an effect of the water uptake carried out by root hair [Tenhunen et al., 2013]. Nevertheless, the interpretation of the resulting resistivity distribution is rarely straightforward, as it represents the cumulative effects of all the occurring phenomena. In order to properly take advantage of the information content in the ERT data, an appropriate planning of the measurement campaign is mandatory, especially if a further application in a hydrological model is intended. In this respect, a good example is illustrated in chap. 3, where a combination of different soundings both with and without the active orange tree is available. In particular, it is possible to exploit these surveys within three different steps of the modeling procedure:

1. Experiment 1: The infiltration test performed after the cut of the tree allows the calibration of the hydrological model, assuming negligible the small activity still put in place by the roots. In other words, this first step provides a representation of the spatial and temporal patterns of soil water content without the activity of the plant, patterns thus depending solely upon the soil hydraulic structure;

2. Experiment 2: The time–lapse monitoring during the scheduled irrigation supplies spatial and temporal variations of soil water content distribution, as a consequence of water infiltration and root water uptake;

3. The comparison of these two models should give an assessment of the location of the active root zone and provide a quantitative estimate of the transpiration fluxes.

5.1.1 Outline of the numerical procedure

It is possible to express the procedure outlined above in a formal manner. The numerical model that describes the dynamics of the soil water content driven by

external forcings can be represented formally by a system of N (i.e number of the mesh nodes) nonlinear equations, which we write as:

$$f(\theta) = L(\theta) - b(\theta) = 0 \tag{5.1}$$

where $f(\theta) : \mathbb{R}^N \to \mathbb{R}^N$ represents the numerical discretization of Richards equation and θ is the N–dimensional solution vector that contains the nodal values of water content. In other words, the i–th component θ_i is the calculated water content at all computational times t^k. Thus, θ_i is a function of time, but we do not write it explicitly to simplify the notation. In eq. (5.1), $L(\theta)$ comprises the stiffness and mass matrices and $b(\theta)$ is a known term that represents the action of the external forcings (e.g. irrigation and plant transpiration). We can think $b(\theta)$ formed by the sum of a term $\tilde{b}(\theta)$ representing the irrigation fluxes on each node of the mesh and $b_T(\theta)$, which represents the plant activity. With these notations, the soil water distribution in Experiment 1 is given by θ_1, where θ_1 is solution to

$$L(\theta) - \tilde{b}(\theta) = 0 \tag{5.2}$$

Note that we have not included the effects of the plant, in agreement with the description of Experiment 1. Similarly, θ_2 is the soil water distribution of Experiment 2, where θ_2 is solution to

$$L(\theta) - \tilde{b}(\theta) - b_T(\theta) = 0 \tag{5.3}$$

with $b_T(\theta)$ being the contribution of the plant activity (i.e. plant transpiration). It is important to underline that $b_T(\theta)$ is a vector whose components contain the information on the known spatial distribution of the root density and the unknown root transpiration fluxes. Thus, the spatial distribution of plant transpiration, as represented by $b_T(\theta)$, is the identification goal of our effort. At this point, we would like to remark that both eq. (5.2) and eq. (5.3) are solved in the CATHY [e.g. Camporese et al., 2010] time stepping procedure at the common times $t^1, t^2, \cdots, t^{final}$. Moreover, to obtain $\theta_i(t^{k+1})$, we need to start from $\theta_i(t^k)$. The ERT measurements are taken at times t_j, with $j = 1, 2, \cdots, T_{ERT}$, with the ERT time step sizes different from the time step sizes of the numerical simulation. Hence, it is impossible to use the water content derived from the ERT measurements as $\theta(t^k)$ to obtain, via the numerical scheme, $\theta(t^{k+1})$. This is the reason why we need to derive a procedure that combines numerical modeling and ERT measurements. In other words, we are using this procedure as a sort of "interpolation" from the ERT times t_j to the simulation times t^k, to enable the determination of b_T by comparison.

It is possible to define the difference in terms of soil water content between the two Experiments as

$$\hat{\theta} = \theta_2 - \theta_1 \tag{5.4}$$

which can be rewritten as

$$\theta_2 = \hat{\theta} + \theta_1 \tag{5.5}$$

It is important to underline that the simple difference between the two model solutions (i.e. eq. (5.4)) is not sufficient to locate which areas of the root system are active during root water uptake. This is a consequence of the interacting processes taking place (i.e. irrigation and transpiration), whose effects are combined and cumulated over time.

Rearranging eq. (5.3), plant transpiration can be expressed as a function of the other terms:

$$b_T(\theta_2) = L(\theta_2) - \tilde{b}(\theta_2) \neq 0 \tag{5.6}$$

However, this calculation is not directly feasible, as Experiment 2 comprises only ERT measurements that furnish soil water content distributions at certain times (i.e. survey times). In other words, this estimation would be possible only if a hydrological model describing the Soil–Plant–Atmosphere continuum with the considered tree was available. Thus, since the plant transpiration is not readily computable (especially in terms of temporal evolution and spatial distribution in the soil), we can approximate b_T as follows. By substituting eq. (5.5) into eq. (5.6), it is possible to resort to another definition of plant transpiration, namely the reconstructed transpiration b_T^R:

$$b_T^R(\theta_2) = L(\theta_2) - \tilde{b}(\theta_2) = L(\hat{\theta} + \theta_1) - \tilde{b}(\hat{\theta} + \theta_1) \tag{5.7}$$

Still, in eq. (5.7), $L(\hat{\theta} + \theta_1)$ is not obtainable, since the water content distribution over time is not available at each time–step of the hydrological model. This is due to the fact that the ERT monitoring is usually performed on a hourly basis, while the time–step size of the hydrological model is of order of seconds or minutes. To overcome this problem, it is possible to expand eq. (5.7) by means of Taylor series, so as to approximate b_T^R:

$$b_T^R(\hat{\theta}_2) = L(\theta_1) + J_L(\theta_1)\hat{\theta} - \tilde{b}(\theta_1) - J_{\tilde{b}}(\theta_1)\hat{\theta} + \cdots \tag{5.8}$$

where J is the Jacobian, i.e. the matrix of all first–order partial derivatives with respect to θ. Considering eq. (5.2), which is equivalent to $L(\theta_1) - \tilde{b}(\theta_1) = 0$, and omitting the higher order terms, eq. (5.8) can be rewritten as:

$$b_T^R(\hat{\theta} + \theta_1) \simeq J_L(\theta_1)\hat{\theta} - J_{\tilde{b}}(\theta_1)\hat{\theta} = J_f(\theta_1)\hat{\theta} \tag{5.9}$$

This approximation is accurate as long as $\hat{\theta}$ is sufficiently small.

5.1.2 Synthetic case study outline

To evaluate the procedure described so far, a synthetic case study is developed, so as to have complete control over all aspects of the modeling phase. This synthetic example comprises three different steps as well, with some particular adjustments that allow a deeper understanding of all features of the proposed approach. In particular:

i. Model 1. Experiment 1 is substituted by an infiltration model, where all parameters (e.g. irrigation fluxes, soil water retention curve, water table depth, etc.) are not representative of the test cases discussed in chap. 3 and chap. 4. Rather, they are chosen to design a realistic but completely synthetic experiment (i.e. they do not refer to a real case study). This synthetic model gives the spatial and temporal distribution of soil water content as a consequence of irrigation in a scenario where the plant is not active;

ii. Model 2. The water content distribution obtained from the ERT measurements in Experiment 2 is replaced by the result of a hydrological model describing the activity of a orange tree. So the soil water content distribution that should result from the resistivity patterns (i.e. by means of a petrophysical relationship, e.g. Archie [1942]), is now represented by the outputs of the plant model, which are considered at specific times, so as to resemble the time–lapse nature of the ERT data collection. This model is identical to that developed at point i., except for the presence of the tree, whose parametrization is based on real data and literature information;

iii. The third step is aimed at evaluating the reconstructed transpiration b_T^R by means of eq. (5.9), i.e. on the basis of the soil water distributions obtained from point i. and point ii.

The main goal of this synthetic case study is to provide insights into the proposed numerical procedure, with particular respect to the influence of the approximation performed in eq. (5.9), in order to evaluate the effects of the omission of the higher order terms. This is finalized to a future application on a real case study (e.g. the example in chap. 3), which will be affected by different types of uncertainties, namely numerical, from the ERT measurements, and related to the Taylor series approximation. The best framework to face these issues is certainly provided by data assimilation techniques, as shown, for instance, by Rossi et al. [2015].

In the following, I introduce CATHY, the hydrological model chosen for the development of the synthetic case study, necessary to evaluate the numerical procedure for the location of the active root zone in terms of plant transpiration. The details of the approximation procedure, necessary to determine the spatial and temporal evolution of the plant transpiration fluxes, are described in terms of Taylor series approximation and Newton–Raphson and Picard iteration schemes. After examining the mathematical aspects of the reconstruction of plant transpiration, I will finally move to the synthetic case study, which comprises the infiltration model, the plant model, and the estimation of the reconstructed plant transpiration on the basis of Taylor series approximation.

5.2 Model description: CATHY

CATHY (CATchment HYdrology) is a distributed physically–based three–dimensional hydrological model that describes and represents the interactions between surface and subsurface water flow. To do this, CATHY couples a finite element solver for

the three–dimensional Richards equation and a finite difference solver for the one–dimensional convection–diffusion equation that describes surface flow propagation [Camporese et al., 2010]. This allows the model to describe several hydrological processes, such as ponding, Horton and Dunne runoff generation, return flow, water reinfiltration, and soil moisture distribution. However, in this work, we are considering only the processes occurring in the subsoil. Therefore, the mathematical model describing soil moisture variations (in a partially saturated porous medium) is given by the following partial differential equation [Paniconi and Wood, 1993; Paniconi and Putti, 1994; Orlandini and Rosso, 1996]:

$$S_s S_w(\psi)\frac{\partial \psi}{\partial t} + \phi \frac{\partial S_w(\psi)}{\partial t} = \nabla \cdot [K_s K_r(\psi)(\nabla \psi + \eta_z)] + q_s(\psi) \tag{5.10}$$

where S_s is the elastic storage term [L^{-1}], $S_w(\psi) = \theta/\phi$ is water saturation [–], θ is the volumetric moisture content [–], ϕ is the porosity [–], ψ is the soil water potential [L], t is time [T], ∇ is the gradient operator, K_s is the saturated hydraulic conductivity [$\mathrm{L\ T}^{-1}$], $K_r(\psi)$ is the relative hydraulic conducitivity [–], $\eta_z = (0, 0, 1)^T$ is the gravitational potential energy gradient with z (the vertical coordinate, directed upward), and q_s comprises both distributed sources and sink terms. The nonlinear dependance of both saturation and relative hydraulic conductivity upon pressure head (i.e., $S_w(\psi)$ and $K_r(\psi)$) can be modeled using either Brooks and Corey [1964], Huyakorn et al. [1984], or van Genuchten and Nielsen [1985].

In this work we employ the version of CATHY developed by Manoli et al. [2014], which not only accounts for soil moisture dynamics, but also for root water uptake, hydraulic redistribution (i.e. the movement of water from roots to soil, HR) whole plant transpiration, and leaf–level photosynthesis. Hence, eq. (5.10) is conveniently modified to consider the plant activity, since here the source/sink term q depends also on leaf water potential ψ_L [L]. Thus, the soil water dynamics is coupled with the root–plant system [Manoli et al., 2014]:

$$S_s S_w(\psi)\frac{\partial \psi}{\partial t} + \phi \frac{\partial S_w(\psi)}{\partial t} = \nabla \cdot [K_s K_r(\psi)(\nabla \psi + \eta_z)] + q_s(\psi, x, y, z, t, \psi_L) \tag{5.11}$$

More in detail, as extensively described by Volpe et al. [2013] and Manoli et al. [2014], the movement of water within the Soil–Plant–Atmosphere continuum is modeled by means of a series of conductances, specifically: soil conductance g_s, root membrane conductance g_r, xylem conductance g_x, and CO_2 stomatal conductance g_{st}. First of all, each plant is associated to a node j, with j ranging from 1 to the total number of plants in the model, and the total root water uptake per unit soil volume from node i (q_i) is given by the sum of the contribution of each single plant j having non–zero root biomass on node i. The connection between root system and soil is realized thanks to a soil–to–root conductance $g_{i,j}$, which represents "the water flux from the soil to the root (or viceversa) crossing the root membrane per unit area of the membrane and per unit difference of the total water potential between the soil and the root" [Manoli et al., 2014]. More in detail, $g_{i,j}$ is given from two conductances in series, the soil conductance ($g_{s,i}$) and the root membrane conductance ($g_{r,i}$) [Volpe et al., 2013; Manoli et al., 2014]

$$g_{i,j} = (g_{s,i} \cdot g_{r,i})/(g_{s,i} + g_{r,i}) \tag{5.12}$$

The occurrence of RWU or HR depends on the energy gradient between the soil and the plant xylem, which, in turn, determines the sign of $q_{i,j}$ (i.e. the soil water uptaken by the roots of plant j at node i, per unit soil volume). The movement of water due to RWU causes a secondary process, the Darcian redistribution, which is properly computed from eq. (5.11). Finally, a fundamental parameter is the plant transpiration rate T_j [L^3 T^{-1}], which is computed for each plant j and depends on the potential energy gradient between the trunk base and the leaf [Manoli et al., 2014]:

$$T_j = -g_{x,j}[(\psi_{L,j} + z_{L,j} - (\psi_{R,j} + z_{R,j})]A_{x,j} \tag{5.13}$$

where $g_{x,j}$ is the xylem conductance, $\psi_{L,j}$ is the leaf water potential, $z_{L,j}$ is the elevation at which the leaf water potential is evaluated [L], $\psi_{R,j}$ is the root water potential, $z_{R,j}$ is the elevation of the trunk base [L], and $A_{x,j}$ is the xylem cross–sectional area [L^2].

A second mathematical model describes the plant–atmosphere interactions [Volpe et al., 2013; Manoli et al., 2014]. To do this, the plant canopy is divided into horizontal layers that allow representing the light attenuation regime as a function of leaf angle distribution and solar zenith angle. Is it important to underline that only the light attenuation regime is considered, as other fundamental parameters like air temperature, water vapor, and CO_2 concentration are assumed to be uniform within the canopy (though time dependent). Therefore, for each canopy layer r, the leaf–scale transpiration is computed based on the CO_2 stomatal conductance $g_{st,j,r}$ [N L^{-2} T^{-1}] [Manoli et al., 2014]:

$$f_{w,j,r}(\psi_{L,j}) = a g_{st,j,r}(\psi_{L,j}) VPD \epsilon_w \tag{5.14}$$

where $a = 1.6$ is the relative diffusivity of water vapor with respect to CO_2, VPD is the vapor pressure deficit, and ϵ_w is a function of molar weight and density of water.

The leaf photosynthesis at canopy layer r is described by a biochemical demand function [Manoli et al., 2014] which takes into account the influence of both light and Rubisco, the CO_2 compensation point, and stomatal conductance [Volpe et al., 2013]:

$$f_{c,j,r} = \frac{a_{1,r}}{a_2 + c_{ic,r}}(c_{ic,r} - c_{cp}) \tag{5.15}$$

with a_1 and a_2 are photosynthetic parameter chosen according to the parameter limiting photosynthesis (i.e. light or Rubisco, respectively), c_{cp} is the CO_2 compensation point, and c_{ic} is the inter–cellular CO_2 concentration. A temperature correction is applied to all the photosynthetic parameters, while the stomatal conductance is optimized for maximum carbon gain at a given water loss. Moreover, the nocturnal stomatal conductance is considered as well and depends on sap flow and VPD, so as to model also the nighttime transpiration. Finally, a nonlinear closure equation is obtained as a consequence of the flux continuity across the soil–plant system [Manoli et al., 2014]:

$$T_j(\psi, \psi_{L,j}) - \sum_r f_{w,j,r}(\psi_{L,j}) \cdot LAI_{j,r} \cdot A_{c,j} = 0 \tag{5.16}$$

where $A_{c,j}$ is the canopy projected area [L^2] and $LAI_{j,r}$ is the leaf area index at canopy layer r [L^2 L^{-2}].

Further details can be found in Volpe et al. [2013], Manoli et al. [2014], and Manoli et al. [2015] (and references therein).

5.3 Taylor series expansion of a multi–variable vector–valued function

The aim of this section is to provide a brief introduction to Taylor series expansion, on which the reconstructed transpiration b_T^R is based.

Given a non–linear function $f(x) : \mathbb{R}^N \to \mathbb{R}^N$, with $x \in \mathbb{R}^N$ defined as $x = (x_1, x_2, ..., x_N)^T$, we can express $f(x) \in \mathbb{R}^N$ as a vector function

$$f(x) = \begin{bmatrix} f_1(x) \\ f_2(x) \\ \vdots \\ f_N(x) \end{bmatrix} \tag{5.17}$$

The Taylor expansion of $f(x)$, with $f(x)$ defined over a close interval $[x_0 - \delta x, x_0 + \delta x]$, $x_0 \in \mathbb{R}^N$, and infinitely differentiable, is:

$$f(x_0 + \delta x) = \sum_{i=0}^{M-1} \frac{f^{(i)}(x_0)}{i!} \delta x^i + R_M(\delta x) \tag{5.18}$$

with $R_M(\delta x)$ being the remainder of order M and $\delta x = (\delta x_1, \delta x_2, ..., \delta x_N)^T$.
If we expand eq. (5.18) up to $M = 3$ we get

$$f(x_0 + \delta x) = f(x_0) + J_f(x_0)\delta x + \frac{1}{2}\delta x^T H_f \delta x + R_3(\delta x) \tag{5.19}$$

where J_f is the Jacobian matrix of $f(x)$ and H_f is the Hessian matrix of $f(x)$.

5.3.1 Example 1: $f(x)$ linear function

If $f(x) : \mathbb{R}^N \times \mathbb{R}^N$ is a linear function, we have that both A and b do not depend on x, with $x \in \mathbb{R}^N$:

$$f(x) = Ax - b \tag{5.20}$$

Expanding eq. (5.20) in Taylor series in the range of x_0, i.e. $[x_0 - \delta x, x_0 + \delta x]$, with $\delta x \in \mathbb{R}^N$ and omitting the terms with order higher than 3, we have:

$$f(x_0 + \delta x) \simeq f(x_0) + J_f(x_0)\delta x + \frac{1}{2}\delta x^T H_f(x_0)\delta x \tag{5.21}$$

where the Jacobian $J_f(x_0)$ is:

$$J_f(x_0) = f'(x_0) = A \tag{5.22}$$

and the Hessian $H_f(x_0)$ is:

$$H_f(x_0) = J(J_f(x_0)) = f''(x_0) = 0 \tag{5.23}$$

since the derivative of a constant is 0. Therefore, substituting eq. (5.22) and eq. (5.23) we get:

$$\begin{aligned} &f(x_0 + \delta x) = f(x_0) + A\delta x + 0 = 0 \\ &A\delta x = -f(x_0) = b - Ax_0 \\ &A\delta x + Ax_0 = b \\ &A(x_0 + \delta x) = b \end{aligned} \tag{5.24}$$

5.3.2 Example 2: $f(x)$ non–linear function

If $f(x) : \mathbb{R}^N \times \mathbb{R}^N$ with $x \in \mathbb{R}^N$ is a non–linear function, the Jacobian and the Hessian matrices need to be properly defined.

The Jacobian J_f is the matrix of all first–order partial derivatives, that is to say

$$J_f(x) = [\nabla_x f_1, \nabla_x f_2, ..., \nabla_x f_n] = \begin{bmatrix} \frac{\partial f_1(x)}{\partial x_1} & \frac{\partial f_2(x)}{\partial x_1} & \dots & \frac{\partial f_n(x)}{\partial x_1} \\ \frac{\partial f_1(x)}{\partial x_2} & \frac{\partial f_2(x)}{\partial x_2} & \dots & \frac{\partial f_n(x)}{\partial x_2} \\ \vdots & \vdots & \ddots & \vdots \\ \frac{\partial f_1(x)}{\partial x_n} & \frac{\partial f_2(x)}{\partial x_n} & \dots & \frac{\partial f_n(x)}{\partial x_n} \end{bmatrix} \tag{5.25}$$

where $\nabla = \left[\frac{\partial}{\partial x_1}; \frac{\partial}{\partial x_2}; \cdots; \frac{\partial}{\partial x_N}\right]^T$ is the gradient operator. In compressed form the Jacobian can ben written as:

$$\{J_f(x)\}_{l,m} = \frac{\partial f_m(x)}{\partial x_l} \tag{5.26}$$

with l being the row index and m being the column index.

Similarly, the Hessian H_f can be expressed as the "three–dimensional" ($N \times N \times N$) matrix:

$$H_f(x) = J(J_f(x)) = \begin{bmatrix} \frac{\partial(\nabla f_1(x))}{\partial x_1} & \frac{\partial(\nabla f_2(x))}{\partial x_1} & \dots & \frac{\partial(\nabla f_N(x))}{\partial x_1} \\ \frac{\partial(\nabla f_1(x))}{\partial x_2} & \frac{\partial(\nabla f_2(x))}{\partial x_2} & \dots & \frac{\partial(\nabla f_N(x))}{\partial x_2} \\ \vdots & \vdots & \ddots & \vdots \\ \frac{\partial(\nabla f_1(x))}{\partial x_N} & \frac{\partial(\nabla f_2(x))}{\partial x_N} & \dots & \frac{\partial(\nabla f_N(x))}{\partial x_N} \end{bmatrix} \tag{5.27}$$

where, for istance:

$$\frac{\partial(\nabla f_1(x))}{\partial x_1} = \begin{bmatrix} \frac{\partial^2 f_1(x)}{\partial x_1^2} \\ \frac{\partial^2 f_1(x)}{\partial x_1 \partial x_2} \\ \vdots \\ \frac{\partial^2 f_1(x)}{\partial x_1 \partial x_N} \end{bmatrix} \tag{5.28}$$

Therefore, we can write the Hessian in a compressed form as well, where l is the row index, m is the column index, and p is the index in the third dimension:

$$\{H_f(\boldsymbol{x})\}^p_{l,m} = \frac{\partial^2 f_m}{\partial x_l \partial x_p} \tag{5.29}$$

We can conclude that the Jacobian is a two–dimensional matrix, while the Hessian is a three–dimensional matrix. A consistency check on the dimensions of each term of Taylor expansion is now useful:

- $f(x)$ is a vector with N elements: $f_l(x)$, with $l = 1, \cdots, N$;
- $J_f(x_0)\delta x$. $J_f(x_0)$ is a $N \times N$ matrix ($J_f(x_0) \in \mathbb{R}^{N\times N}$), while δx is an N–dimensional ($\delta x \in \mathbb{R}^N$). Therefore this term is a vector with N elements. We can rewrite the components of this second term as $\{J_f(x)\delta x\}_l = \sum_{k=1}^N \{J_f(x)\}_{l,k}\delta x_k$;
- $\frac{1}{2}\delta x^T H_f(x_0)\delta x$. $H_f(x)$ is a three–dimensional matrix ($H_f(x) \in \mathbb{R}^{N\times N\times N}$), while δx is a vector with N elements ($\delta x \in \mathbb{R}^N$). $\delta x^T H_f$ gives a $N \times N$ matrix and in components it can be written as $\{\delta x^T H_f\}_{l,m} = \sum_{k=1}^{N} \delta x_k \{H_f(x_0)\}^k_{l,m}$. Hence, $\delta x^T H_f(x_0)\delta x$ becomes a vector with N elements with components given by $\{\delta x^T H_f \delta x\}_l = \sum_{j=1}^{N} \left(\sum_{k=1}^{N} \{H_f(x_0)\}^k_{l,j}\delta x_k \right) \delta x_j$

So, each term is a vector with N elements, i.e. $f(x) \in \mathbb{R}^N$, $J_f(x_0)\delta x \in \mathbb{R}^N$, and $\frac{1}{2}\delta x^T H_f(x_0)\delta x \in \mathbb{R}^N$.

A quasi–linear example

In this example we want determine the Jacobian of the quasi–linear system

$$f(x) = A(x)x - b(x) \tag{5.30}$$

where $f(x) : \mathbb{R}^N \to \mathbb{R}^N$, $x \in \mathbb{R}^N$. Note that this is the general form of the nonlinear system solved at each time step in the CATHY model. First of all, to compute the Jacobian of $f(x)$ we can consider a single element:

$$\frac{\partial f_m}{\partial x_l} = \frac{\partial}{\partial x_l}[-b_m(x) + (A(x)x)_m] = -\frac{\partial b_m(x)}{\partial x_l} + \frac{\partial (A(x)x)_m}{\partial x_l} \tag{5.31}$$

with

$$(A(x)x)_m = \sum_{j=1}^{N} [A(x)]_{m,j} x_j = \sum_{j=1}^{N} a_{m,j}(x) x_j \tag{5.32}$$

Therefore

$$\frac{\partial (A(x)x)_m}{\partial x_l} = \sum_{j=1}^{N} \frac{\partial [a_{m,j}(x)x_j]}{\partial x_l} = \sum_{j=1}^{2} \left\{ \left[x_j \frac{\partial a_{m,j}(x)}{\partial x_l} \right] + a_{m,l}(x) \right\} \tag{5.33}$$

As a result, the Jacobian J_f is given in a more general way by

$$J_f(x) = A(x) + J_A(x)x - J_b(x) \tag{5.34}$$

where $J_A(x)x$ is a matrix

$$[J_A(x)x]_{l,m} = \sum_{j=1}^{N} \frac{\partial(a_{m,j}(x))x_j}{\partial x_l} \tag{5.35}$$

5.4 Newton–Raphson and Picard iteration schemes

5.4.1 Numerical discretization

The solution to eq. (5.11) is obtained numerically by means of Galerkin Finite Element approach with linear ($\mathcal{P}_1$) basis functions [Paniconi and Putti, 1994]. Given a domain Ω discretized in E_l elements and N nodes, the solution pair (ψ, θ) is approximated by (ψ_h, θ_h) (see e.g. Scudeler et al. [2016]):

$$\psi(t,u) \simeq \psi_h(t,u) = \sum_{j=1}^{N} \psi_j(t) w_j(u) \tag{5.36}$$

$$\theta(t,u) \simeq \theta_h(\psi_h(t,u)) = \sum_{j=1}^{N} \theta_j(\psi_j(t)) w_j(u) \tag{5.37}$$

where $u \in \Omega$ is the vector of three–dimensional coordinates and $w(u)$ are the linear basis functions. It is possible to recast eq. (5.11) as its Finite Element Method (FEM) formulation:

$$\begin{aligned}\int_\Omega \frac{\theta_h(\psi_h)}{\phi} S_s \frac{\partial \psi_h}{\partial t} w_i \, du + \int_\Omega \frac{\partial \theta_h(\psi_h)}{\partial t} w_i \, du \\ + \int_\Omega K_r(\theta_h(\psi_h)) K_s(\nabla \psi_h + \eta_z) \cdot \nabla w_i \, du - \int_\Omega \tilde{q}_s \, w_i \, du + \int_{\Gamma_N} q_N w_i \, ds \\ - \int_\Omega q_p \, w_i \, du = 0 \quad \text{with} \quad i = 1, ..., N\end{aligned} \tag{5.38}$$

where q_N is the prescribed Neumann flux [$\mathrm{L}^3\ \mathrm{T}^{-1}$] and q_p is the flux due to plant activity [$\mathrm{L}^3\ \mathrm{T}^{-1}$] (i.e. $q_s = \tilde{q}_s + q_p$ in eq. (5.11)). The spatial linearization leads to a system of non–linear ordinary differential equations that is discretized by means of backward Euler finite difference scheme [Paniconi and Putti, 1994; Scudeler et al., 2016], yielding the following quasi–linear system in the form of eq. (5.1) and eq. (5.30):

$$\begin{aligned}F(\Theta_h^{k+1}) = \\ = H(\Theta_h^{k+1})\Psi_h^{k+1} + \frac{1}{\Delta t^{k+1}} P_1(\Theta_h^{k+1})\Psi_h^{k+1} + \frac{1}{\Delta t^{k+1}} P_2 \Theta_h^{k+1} + b_1(\Theta_h^{k+1}) \\ - \frac{1}{\Delta t^{k+1}} P_2 \Theta_h^{k} - \frac{1}{\Delta t^{k+1}} P_1(\Theta_h^{k+1})\hat{\Psi}^k + b_2 + b_3(\Theta_h^{k+1}) = 0\end{aligned} \tag{5.39}$$

where $\Theta_h = \Theta_h(\Psi_h^{k+1}) = \{\theta_i(\psi_i^{k+1})\}$ is the vector containing the nodal water contents, $\Psi_h^{k+1} = \{\psi_i^{k+1}\}$ is the vector containing the nodal pressure heads, $H(\Theta_h^{k+1}) = \{h_{ij}(\Theta_h^{k+1})\}$ with $i, j = 1, ..., N$ is the flow stiffness matrix where each coefficient is a nonlinear function of Θ_h^{k+1}, Δt^{k+1} is the time step size, k is the time step, $P_1(\Theta_h^{k+1}) = \{p_{1,ij}(\Theta_h^{k+1})\}$ and $P_2 = \{p_{2,ij}\}$ with $i, j = 1, ..., N$ are the flow mass matrices, $b_1 = \{b_{1,i}(\Theta_h^{k+1})\}$ is the vector accounting for the gravitational term with coefficients that are nonlinear functions of Θ_h^{k+1}, $b_2 = \{b_{2,i}\}$ is vector containing the boundary term, and $b_3 = \{b_{3,i}(\Theta_h^{k+1})\}$ is the vector accounting for the plant activity.

We can express each term of eq. (5.39) as:

$$h_{ij}(\Theta_h) = \int_\Omega K_r(\Theta_h) K_s \nabla w_j \cdot \nabla w_i \, du \tag{5.40}$$

$$p_{1,ij}(\Theta_h) = \int_\Omega \frac{\Theta_h}{\phi} S_s w_i w_j \, du \tag{5.41}$$

$$p_{2,ij}(\Theta_h) = \int_\Omega w_i w_j \, du \tag{5.42}$$

$$b_{1,i}(\Theta_h) = \int_\Omega K_r(\Theta_h) K_s \eta_z \cdot \nabla w_i \, du \tag{5.43}$$

$$b_{2,i} = \int_{\Gamma_N} q_N w_i \, ds \tag{5.44}$$

$$b_{3,i} = \int_\Omega q_p w_i \, du \tag{5.45}$$

The system of non–linear equations (5.39) is solved by means of Newton–Raphson and Picard iteration schemes, as illustrated in the following subsection and thoroughly described by Paniconi and Putti [1994]. Finally, the convergence of the highly non–linear processes occurring is guaranteed by time step adaptation, which enables the time step size to vary (increase, decrease, or, if not necessary, to be left unchanged) at each new time according to the number of Picard iterations required for convergence.

5.4.2 Newton–Rapshon and Picard iteration schemes

First of all, we would like to underline that eq. (5.39) is exactly eq. (5.1) and eq. (5.30), which represent the numerical model in sec. 5.1 and subsec. 5.3.2, respectively. However, CATHY solves for pressure head, using the assumption that the retention curve $\theta(\psi)$ is invertible, so that $\theta(\psi)$ or $\psi(\theta)$ is equivalent, up to the appropriate mathematical modifications of the equation. Thus, from here on we describe CATHY as it is, i.e. using $\psi(\theta)$.

The formulation of Newton–Raphson and Picard iteration schemes in CATHY can be obtained by means of Taylor series. It is possible to recast eq. (5.39) as:

$$F(\Psi_h) = A(\Psi_h)\Psi_h - b(\Psi_h) = 0 \tag{5.46}$$

where

$$A(\Psi_h^{k+1}) = H(\Psi_h^{k+1}) + \frac{1}{\Delta t^{k+1}} P(\Psi_h^{k+1}) \tag{5.47}$$

$$b(\Psi_h^{k+1}) = \frac{1}{\Delta t^{k+1}} P(\Psi_h^{k+1}) \Psi_h^k + \hat{q}(\Psi_h^{k+1}) \tag{5.48}$$

Newton–Raphson iteration scheme

If we expand eq. (5.46) up to the second order term (i.e. $M = 2$ in eq. (5.18)) using Taylor series we get:

$$\begin{cases} F(\Psi_h^{k+1,r} + \delta\Psi_h) = F(\Psi_h^{k+1,r}) + J_f(\Psi_h^{r+1,r})\ \delta\Psi_h + R_2(\delta\Psi_h) = 0 \\ \delta\Psi_h = \Psi_h^{k+1,r+1} - \Psi_h^{k+1,r} \end{cases} \tag{5.49}$$

where $R_2(\delta\Psi_h)$ is the remainder of order 2, r is the iteration index, and therefore $\delta\Psi_h$ is the difference between the solution Ψ_h at two different iterations at the same time step (analogous to $x_0 + \delta x$ in sec. 5.3). Assuming $R_2(\delta\Psi_h)$ negligible and rearranging, we get the formulation of Newton–Raphson iteration scheme:

$$\begin{cases} J_f(\Psi_h^{r+1,r})\ \delta\Psi_h = -F(\Psi_h^{k+1,r}) \\ \Psi_h^{k+1,r+1} = \Psi_h^{k+1,r} + \delta\Psi_h \end{cases} \tag{5.50}$$

with the Jacobian, $J_F(\Psi_h^{k+1,r})$, according to eq. (5.34), being equal to:

$$J_F(\Psi_h^{k+1,r}) = A(\Psi_h^{k+1,r}) + J_A(\Psi_h^{k+1,r})\Psi_h^{k+1,r} - J_b(\Psi_h^{k+1,r}) \tag{5.51}$$

The lm–th element of $J_A(\Psi_h^{k+1,r})$, with l being the row index ($l = 1, ..., N$) and m being the column index ($m = 1, ..., N$), is

$$[J_A(\Psi_h^{k+1,r})\Psi_h^{k+1,r}]_{l,m} = \sum_{j=1}^{N} \frac{\partial}{\partial \Psi_{h_l}} (a_{m,j}(\Psi_h^{k+1,r})\Psi_{h_j}^{k+1,r}) \tag{5.52}$$

while the lm–th element of $J_b(\Psi_h^{k+1,r})$ is simply:

$$[J_b(\Psi_h^{k+1,r})]_{l,m} = \frac{\partial b_m(\Psi_h^{k+1,r})}{\partial \Psi_{h_l}} \tag{5.53}$$

Picard iteration scheme

Eq. (5.50) defines Newton–Raphson iterative scheme but, if we do not consider the first order derivatives, it is possible to determine Picard iteration scheme instead. Therefore, if we rewrite eq. (5.51) as:

$$J_F(\Psi_h^{k+1,r}) = A(\Psi_h^{k+1,r}) \tag{5.54}$$

and substitute eq. (5.46) and eq. (5.54) into eq. (5.50) we obtain

$$\begin{cases} A(\Psi_h^{k+1,r})\ \delta\Psi_h = -(A(\Psi_h^{k+1,r})\Psi_h^{k+1,r} - b(\Psi_h^{k+1,r})) \\ \delta\Psi_h = \Psi_h^{k+1,r+1} - \Psi_h^{k+1,r} \end{cases} \tag{5.55}$$

Therefore, eq. (5.55) is equal to

$$A(\Psi_h^{k+1,r})\ (\Psi_h^{k+1,r+1} - \Psi_h^{k+1,r}) = -(A(\Psi_h^{k+1,r})\Psi_h^{k+1,r} - b(\Psi_h^{k+1,r})) \tag{5.56}$$

5.5 Estimation of plant transpiration

The estimation of plant transpiration takes place through the definition of b_T^R, i.e. the reconstructed transpiration. As introduced in sec. 5.1, we base this numerical procedure on two hydrological models that differ only for the presence of an orange tree in one of them, namely Model 1, sole irrigation (eq. (5.2)), and Model 2, with the orange tree (eq. (5.3)). These models are properly combined by means of Taylor series expansion, as we are about to describe. As introduced above, CATHY solves for pressure head. Nevertheless, we assume that the retention curve $\theta(\psi)$ is invertible, so that $\theta(\psi)$ or $\psi(\theta)$ can be used equivalently assuming that the proper mathematical transformations are performed. So the numerical procedure is here expressed in function of the soil water content, which is the most natural variable in this case. In particular, for a matter of clarity, we are going to use a simplified notation, i.e. $\theta_1^{k+1} = \theta_1$ and $\theta_2^{k+1} = \theta_2$, while θ at the previous time step k will be explicitly stated as θ_1^k and θ_2^k, respectively.

To determine b_T^R, it is useful to express the two models according to eq. (5.46), eq. (5.47), and eq. (5.48). Thus, for Model 1 we get:

$$f(\theta_{M1}, \theta_{M1}^k) = A(\theta_{M1})\theta_{M1} - \tilde{b}(\theta_{M1}, \theta_{M1}^k) = 0 \tag{5.57}$$

and for Model 2:

$$f(\theta_{M2}, \theta_{M2}^k) = A(\theta_{M2})\theta_{M2} - \tilde{b}(\theta_{M2}, \theta_{M2}^k) - b_T(\theta_{M2}) = 0 \tag{5.58}$$

where, once again, $f(\theta) : \mathbb{R}^N \to \mathbb{R}^N$, θ_{M1} is the soil water content distribution solution to Model 1, θ_{M2} is the soil water content distribution solution to Model 2, $\tilde{b}(\theta)$ accounts for the irrigation fluxes (see eq. (5.60) below), and $b_T(\theta)$ describes the plant transpiration that we want to approximate. Thus, the plant transpiration flux can be written as a function of the general water content θ at times $k+1$ and k:

$$b_T(\theta, \theta^k) = A(\theta)\theta - \tilde{b}(\theta, \theta^k) \tag{5.59}$$

with

$$\tilde{b}(\theta, \theta^k) = \frac{1}{\Delta t} P(\theta^k)\theta^k + b_{NG}(\theta) \tag{5.60}$$

where $b_{NG}(\theta)$ contains the contribution of the gravity term and the Neumann boundary conditions of Richards equation.

We remark once again that in a real experiment only θ_{M2} would be provided by the ERT measurements at time $t = k + 1$, while θ_{M1} and θ^k_{M1} would be calculated using the model calibrated without the plant transpiration. On the contrary, when considering the synthetic case study, both θ_{M2} and θ^k_{M2} are supplied by the model with the plant. This gives the chance to investigate the effects of the approximation of θ^k_{M2}, necessary in the real case study.

The deviation of Model 2 from Model 1 can be expressed in terms of difference in soil water content distribution, as already seen with eq. (5.4), at both times $t = k + 1$ and $t = k$, i.e.

$$\hat{\theta}_M = \theta_{M2} - \theta_{M1} \tag{5.61}$$

$$\hat{\theta}^k_M = \theta^k_{M2} - \theta^k_{M1} \tag{5.62}$$

Nevertheless, it is important to highlight that this simple difference is not sufficient to locate the active root zone or, in other words, to determine the spatial and temporal patterns of plant transpiration. This is strongly related to the fact that the variations taking place in the investigated subsoil are a summation of different nonlinear processes. Therefore, we should use eq. (5.61) to approximate plant transpiration by means of Taylor series around θ_1 with increment $\hat{\theta}$:

$$\begin{aligned} b_T(\theta_{M2}, \theta^k_{M2}) = b_T(\theta_{M1} + \hat{\theta}_M, \theta^k_{M2}) = \\ = A(\theta_{M1} + \hat{\theta}_M)(\theta_{M1} + \hat{\theta}_M) - \tilde{b}(\theta_{M1} + \hat{\theta}_M, \theta^k_{M2}) \end{aligned} \tag{5.63}$$

which can be expanded as

$$\begin{aligned} b_T(\theta_{M2}, \theta^k_{M2}) \simeq b^R_T(\theta_{M1} + \hat{\theta}_M, \theta^k_{M2}) = \\ = b^R_T(\theta_{M1}, \theta^k_{M1}) + D_\theta \Big[b^R_T(\theta_{M1}, \theta^k_{M1}) \Big] (\theta_{M1}, \theta^k_{M1}) \hat{\theta}_M \\ + D_{\theta^k} \Big[b^R_T(\theta_{M1}, \theta^k_{M1}) \Big] (\theta_{M1}, \theta^k_{M1}) \hat{\theta}^k_M \end{aligned} \tag{5.64}$$

where $D_\theta[b^R_T]$ and $D_{\theta^k}[b^R_T]$ denote the Jacobian matrices of eq. (5.59) with respect to the first argument θ and to the second argument θ^k, respectively. Furthermore, we neglect higher order terms.

The different terms of Taylor series are (see eq. (5.34) and eq. (5.59)):

- According to eq. (5.57) we get:

$$b^R_T(\theta_{M1}, \theta^k_{M1}) = A(\theta_{M1})\theta_{M1} - \tilde{b}(\theta_{M1}, \theta^k_{M1}) = 0 \tag{5.65}$$

- The second term is:

$$\begin{aligned} D_\theta \Big[b^R_T(\theta_{M1}, \theta^k_{M1}) \Big] (\theta_{M1}, \theta^k_{M1}) \hat{\theta}_M = \\ = A(\theta_{M1})\hat{\theta}_M + \Big[J_A(\theta_{M1})\theta_{M1} \Big] \hat{\theta}_M - J_{\tilde{b},\theta}(\theta_{M1}, \theta^k_{M1}) \hat{\theta}_M \end{aligned} \tag{5.66}$$

- The third term is:

$$D_{\theta^k} \Big[b^R_T(\theta_{M1}, \theta^k_{M1}) \Big] (\theta_{M1}, \theta^k_{M1}) \hat{\theta}^k_M = -J_{\tilde{b},\theta^k}(\theta_{M1}, \theta^k_{M1}) \hat{\theta}^k_M \tag{5.67}$$

Note that the known quantities in the above equations are: $b_T^R(\theta, \theta^k) = 0$, as it is the model without the plant activity (see eq. (5.57)), θ_{M1} and θ_{M1}^k, still provided by M1, θ_{M2} given by M2 (i.e. model with the plant activity or from ERT water content), $\hat{\theta}_M = \theta_{M2} - \theta_{M1}$, and the expression of the Jacobians. On the contrary, the value of $\hat{\theta}_M^k = \theta_2^k - \theta_1^k$ is unknown and must be approximated.

In this first application, the Jacobians are computed as follows:

(i) From eq. (5.66):

$$(J_A(\theta)\theta)_{i,j} \simeq \left(\frac{A(\theta^{k+1}) - A(\theta^k)}{||\theta^{k+1} - \theta^k||} \right)_{i,j} \tag{5.68}$$

(ii) From eq. (5.66) and eq. (5.67), the Jacobians $J_{\tilde{b}}(\theta_{M1}, \theta_{M1}^k)$ are approximated by a diagonal matrix, whose elements are given by:

$$(J_{b_{NG},\theta})_{i,i} \simeq \left(\frac{\tilde{b}_{NG_i}(\theta^{k+1}) - \tilde{b}_{NG_i}(\theta^k)}{||\theta^{k+1} - \theta^k||} \right)_{i,i} \tag{5.69}$$

and a sparse matrix:

$$(J_{bP,\theta^k})_{i,j} \simeq \frac{1}{\Delta t} \left(\frac{P_{i,j}(\theta^{k+1}) - P_{i,j}(\theta^k)}{||\theta^{k+1} - \theta^k||} \right)_{i,j} \tag{5.70}$$

Eq. (5.64) provides a spatial reconstruction of the active root zone locating the areas that activate during the plant transpiration. Note that we assume that all water uptaken by the tree is transpired, since there is no water storage in any part of the plant, as described in sec. 5.1. However, as a first approximation, we neglect the term described in eq. (5.67). Further studies will ascertain its effect on the reconstructed transpiration b_T^R by using an appropriate interpolation method to derive θ_M^k.

Finally, computing b_T^R requires another precaution. In order to apply eq. (5.64), it is necessary to consider the same times in both models, i.e. M1 and M2. This is easily achievable by fixing the time step size at the same value in M1 and M2 while its variation during the simulation needs to be avoided.

5.6 Example on a saturated domain

5.6.1 Introduction

In order to exemplify the procedure used to recover the transpiration fluxes, a saturated example is developed by means of the CATHY model. This examples comprises two identical hydrological models, namely E1 and E2, where the only difference lies is the prescribed Neumann flux. This variation in terms of boundary conditions substitutes the plant activity. In fact, even if these two processes differ in terms of order of magnitude and, most of all, sign (i.e. the chosen Neumann flux enters the domain while root water uptake removes water from the subsoil), they both modify $q_s(\psi)$ in eq. (5.11). Therefore, we use this example to reconstruct the difference between the

known terms of E1 and E2 starting from the calculated difference in pressure head (note, however, that pressure head and soil water content are assumed invertible, as described in sec. 5.5). This is comparable to the reconstruction of b_T that I will present in chap. 6, which, on the contrary, will take place only at determined times.

5.6.2 Modeling details

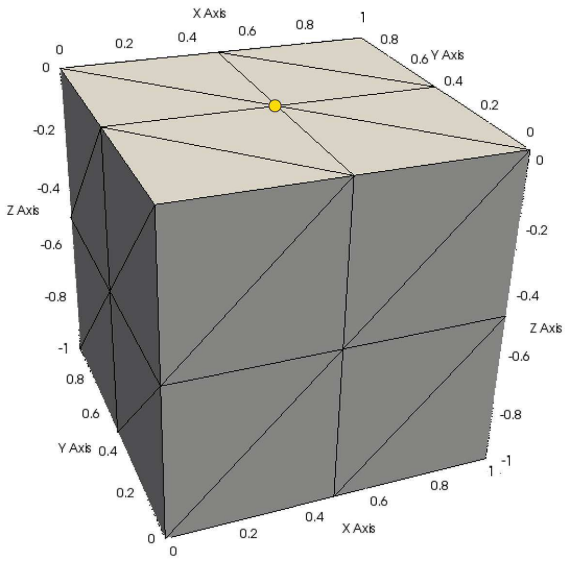

Fig. 5.1: Finite element mesh for the saturated example. It is made up of 27 nodes and 48 tetrahedral elements. The yellow circle locates the node where the Neumann boundary flux is imposed.

In this example, the mesh consists of 27 nodes and 48 tetrahedral elements divided in two layers, while the prescribed Neumann flux is imposed on one superficial node (Fig. 5.1). On all the other boundary nodes a Dirichlet condition with $\psi = 0$ is applied. We decided to consider a rather small domain so as to easily compare the real and reconstructed known terms differences on each node of the mesh. The prescribed Neumann flux is equal to 1.0E-03 m^3/s in E1 and to 1.0E-04 m^3/s in E2, while in both cases the soil is defined as a loamy–sand according to the parameters provided by Leij et al. [1996]. Finally, as already mentioned above, the whole domain is assumed to be saturated.

To guarantee a perfect match between the time steps in the two models, necessary to allow the reconstruction of the difference of known terms, time step adaptation does not take place, therefore the time step size is constant throughout both simulations and equal to 100 s. The total simulation time is equal to 5000 s.

5.6.3 Application of the numerical procedure

The reconstructed difference between the known terms of E1 and E2 is obtained by means of the approach described in sec. 5.5. However, some details need to be redefined. The two models E1 and E2 can be expressed in the form introduced with equations eq. (5.46), eq. (5.47), and eq. (5.48), i.e.

$$f(\theta_{E1}) = A(\theta_{E1})\theta_{E1} - \tilde{b}(\theta_{E1}) = 0 \tag{5.71}$$

and

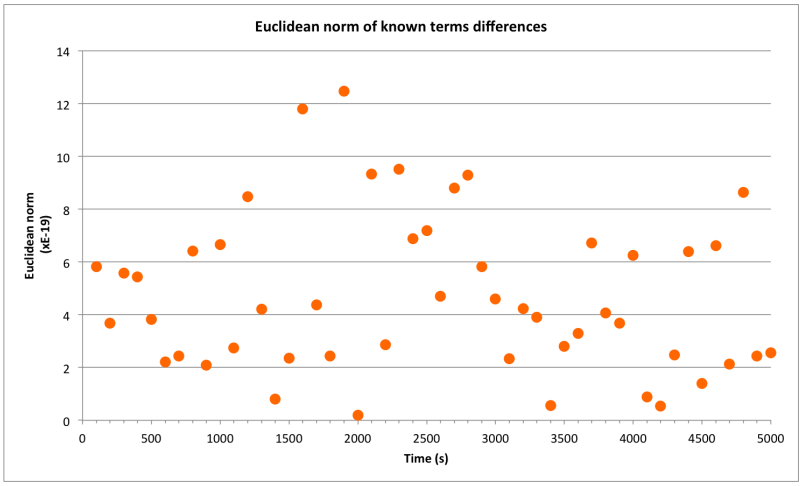

Fig. 5.2: Variation of the Euclidean norm of known terms differences ||diff|| with time in the saturated example. Note that the values of the Euclidean norms on the ordinate axis need to be multiplied by 10^{-19}.

$$f(\theta_{E2}) = A(\theta_{E2})\theta_{E2} - \tilde{b}(\theta_{E2}) = 0 \tag{5.72}$$

where $f(\theta) : \mathbb{R}^N \to \mathbb{R}^N$, θ_{E1} is solution to E1, θ_{E2} is solution to E2, $A(\theta)$ comprises stiffness and mass matrices, and $\tilde{b}(\theta)$ accounts for the imposed Neumann flux. Since in this example we are considering a saturated domain, we have that

$$H(\theta_{E1}) = H(\theta_{E2}) = H_c \tag{5.73}$$

and

$$P(\theta_{E1}) = P(\theta_{E2}) = P_c \tag{5.74}$$

which leads to

$$A(\theta_{E1}) = A(\theta_{E2}) = A_c \tag{5.75}$$

Recasting and combining eq. (5.71) and eq. (5.72) with eq. (5.75) we obtain

$$\tilde{b}_{E1} - \tilde{b}_{E2} = A_c(\theta_{E1} - \theta_{E2}) \tag{5.76}$$

which can be expressed in numerical terms as

$$\begin{aligned} D(\Theta_h^{k+1,r+1}) = & \\ & = \left[H_c + \frac{1}{\Delta t} P_c\right](\Theta_{h,E1}^{k+1,r+1} - \Theta_{h,E2}^{k+1,r+1}) \\ & - \frac{1}{\Delta t} P_c(\Theta_{h,E2}^{k+1,r+1} - \Theta_{h,E1}^{k+1,r+1}) + \hat{q}_{E2}(\Psi_{h_{E2}}^{k+1}) - \hat{q}_{E1}(\Psi_{h_{E1}}^{k+1}) \end{aligned} \tag{5.77}$$

with $D(\Theta_h^{k+1,r+1})$ being the reconstructed difference of the known terms between E1 and E2. Note that the time step size Δt does not depend on the iteration index

k, since it is constant throughout both simulations, as required by the procedure in sec. 5.5.

Eq. (5.77) is applied at each node of the mesh in Fig. 5.1. The results are shown in Fig. 5.2, where they are expressed at each time step in terms of the Euclidean norm of the difference between the real and the computed known terms differences, i.e.

$$||d_r(t)|| = \sqrt{\sum_{i=1}^{N}(D_{real_i}(t) - D_i(t))^2} \text{ with } t = 100, 200, \cdots, 5000\text{s} \tag{5.78}$$

where $||\cdot||$ is the Euclidean norm of the difference d_r between real and reconstructed values, $N = 27$ is the number of nodes, D_{real_i} is the real difference between the known terms of E1 and E2 (i.e. as output from CATHY), and D_i is the computed difference between known terms according to eq. (5.77), and t is the time at each time step.

Even if the values shown in Fig. 5.2 are rather scattered, their order of magnitude is 10^{-19}, which means that, from a numerical point of view, they can be considered 0. Therefore, we can conclude that we properly reconstructed the difference between the known terms of E1 and E2 at each time step of the simulations.

6

Synthetic case study

***

As already introduced before, we develop a synthetic case study in order to obtain a dataset suitable to test the reconstruction of plant transpiration as described in sec. 5.5. This synthetic case study consists of two hydrological models: the former is an infiltration model, while the latter describes the activity of a plant. These two models are identical, except for the presence of the tree, and in both cases all parameters are chosen in order to develop a plausible case and not to reproduce some real conditions. The main advantage of working with a synthetic case study is the absence of all the uncertainties that affect real datasets, like those related to ERT measurements and numerical models.

6.1 Infiltration model

This first model is aimed at representing the variation of spatial and temporal soil moisture content patterns as a consequence of the sole infiltration of irrigation water.

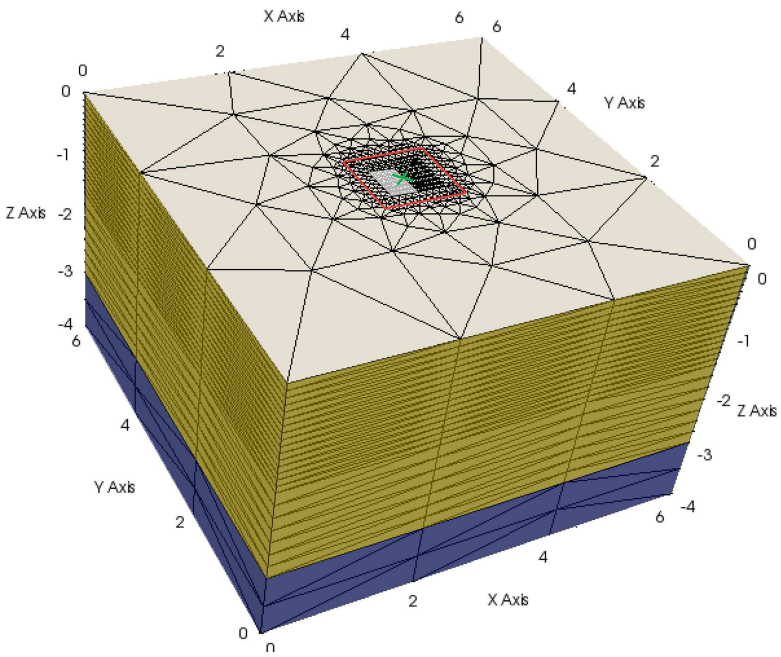

Fig. 6.1: Finite element mesh for infiltration and plant models. It is made up of 9282 nodes and 52500 tetrahedral elements. The white part locates the irrigation atmospheric boundary condition, the yellow part corresponds to the no flow Neumann boundary condition, and the dark blue part pinpoints the Dirichlet boundary condition nodes. The green cross indicates the position of the tree trunk (only in the plant model).

The first step is the development of a three–dimensional finite element mesh representing the investigated domain, over which the system of equation describing

both surface and subsurface processes is solved. In our case, it consists of 9282 nodes and 52500 elements, subdivided into 25 horizontal layers with thickness increasing with depth (i.e. 16 layers 0.1 m thick, 7 layers 0.2 m thick, and 2 layers 0.5 m thick), as shown in Fig. 6.1. Thus, the total depth is equal to 4.0 m, while length and width are both equal to 6.4 m. In spite of the dimensions of our mesh, we are actually interested only on a smaller subdomain (called "inner domain"), assumed to recall the volume investigated during the ERT surveys. In particular, it is defined by a superficial square with side equal to 1.2 m (red polygon in Fig. 6.1) and extended till a depth of 1.2 m. Nevertheless, modeling a bigger domain is mandatory, in order to avoid the influence of boundary effects on the inner zone.

Once created the mesh, we characterized the soil by means of the parameters in Tab. 6.1, provided by Leij et al. [1996]. We opted for a loamy sand soil, homogeneous and isotropic, while the water retention curve is described thanks to van Genuchten and Nielsen [1985] (Tab. 6.1). The water table is located 3.0 m below ground level. The resulting relationships between soil water content and pressure head, and relative hydraulic conductivity and pressure head, are shown in Fig. 6.2 and Fig. 6.3, respectively.

Parameter	Symbol	Value
Saturated hydraulic conductivity	K_s	4.05278E-05 m/s
Porosity	$\phi = \theta_s$	0.41
Residual moisture content	θ_r	0.057
van Genuchten curve parameter	α	12.4 m^{-1}
van Genuchten curve exponent	n	2.28

Tab. 6.1: Soil and van Genuchten parameters for the infiltration and plant models. Values taken from Leij et al. [1996].

On all nodes of the lateral boundary of the vadose zone (i.e. above the water table), as well as on the bottom face of the mesh, we imposed a Neumann condition of no flow, while, on the boundary of the saturated zone, pressure head is assumed to linearly increase with depth from a value of $\psi = 0$ m in correspondence of the water table (i.e. Dirichlet boundary condition) (Fig. 6.1). Irrigation is imposed as an atmospheric boundary condition and takes place on a small portion of the upper surface (i.e. 39 nodes covering an area of about 0.18 m^2, Fig. 6.1), so as to resemble the drip irrigation occurring at the field site. We assumed an irrigation of 4 l h^{-1} (i.e. 22.1 mm h^{-1}) for 5 h d^{-1} taking place for 15 days, then suspended for 5 days, and then performed for other 10 days, while rain precipitation is not considered. Water ponding is neglected. The initial pressure head distribution (i.e. the initial condition) is nonuniform and has been computed thanks to another infiltration model, where irrigation is simulated for 15 days. This expedient is necessary since the infiltration and the plant models need to share the same initial conditions in

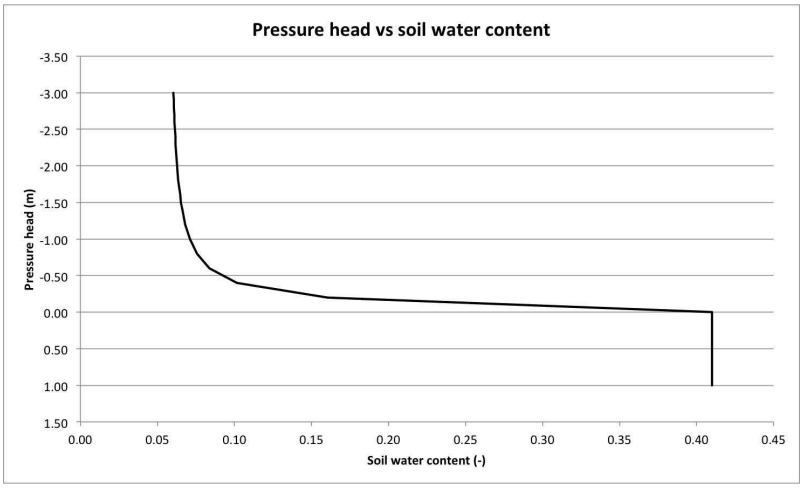

Fig. 6.2: Graph representing the relationship between soil water content and pressure head according to the parameters chosen for the simulations described in Tab. 6.1.

order to be comparable, and derives from the impossibility to "activate" the plant after a certain amount of time from the beginning of the simulation. Therefore, the total simulation time is equal to 45 days. Finally, time adaptation is intentionally avoided, in order to maintain the time step size constant (and equal to 120 s) throughout the whole simulation.

The results of this first model in terms of saturation evolution over time are shown in Fig. 6.5(a).

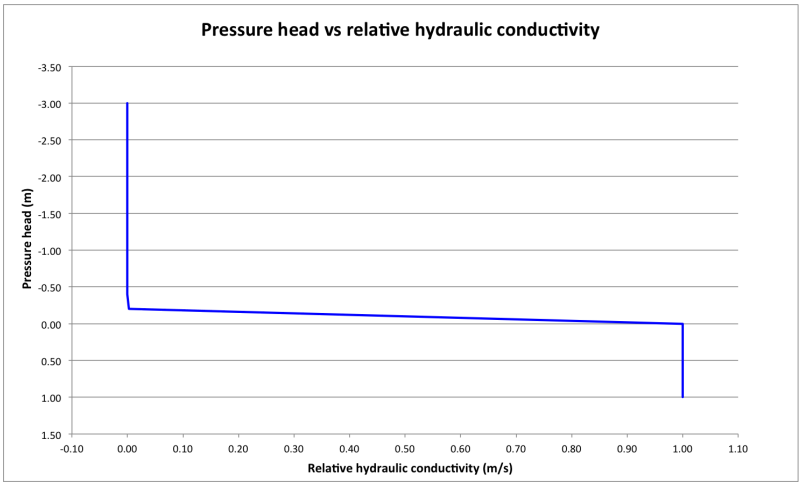

Fig. 6.3: Graph representing the relationship between relative hydraulic conductivity and pressure head according to the parameters chosen for the simulations described in Tab. 6.1.

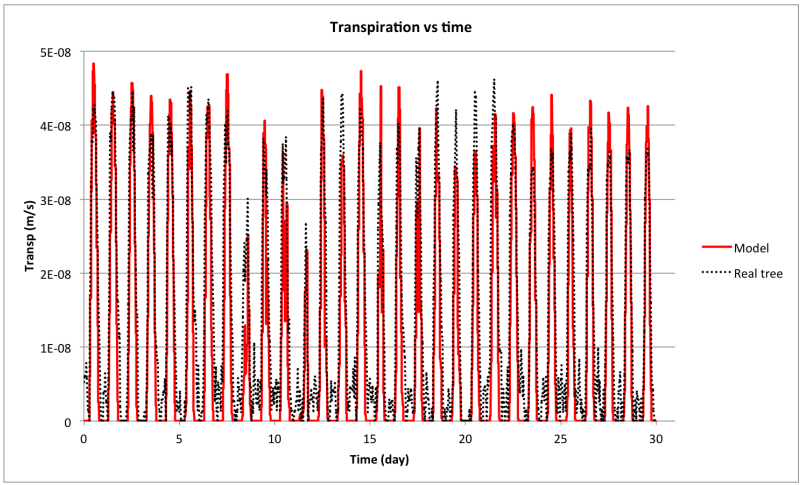

Fig. 6.4: Comparison between the real transpiration of an orange tree at Bulgherano field site (see chap. 3), black dotted line, and the transpiration resulting from the synthetic model, red solid line. The nocturnal activity is not modeled.

6.2 Plant model

The plant model is identical to the infiltration model except for the presence of the tree. Therefore, mesh, irrigation schedule, boundary conditions, initial conditions, and soil parameters are those described in subsec. 6.1. In particular, the chosen initial conditions allow us to start modeling the plant activity after 15 days of sole irrigation. So also in this case the simulation time is equal to 45 days (i.e. 15 days of sole irrigation, 15 days of irrigation and plant activity combined, 5 days of sole plant activity, and finally 10 more days of irrigation and plant activity combined). Furthermore, time step adaptation is not taking place, as the time step size needs to be constant during the whole simulation (see sec. 5.5 for further details).

The plant is described by means of several parameters, summarized in Tab. 6.2, as required by the model of Manoli et al. [2014]. In particular, the leaf area index is assumed constant over time, i.e. the plant does not grow nor the canopy is trimmed. The parameters can be either measured, i.e. from real orange trees, assumed, or taken from literature. The root system covers an area of 1.2×1.2 m^2 centered on the tree trunk and reaches a maximum depth of 0.4 m below ground level, in accordance with Kotur and Keshava Murthy [1998]. For the root length density vertical profile we assumed an exponential distribution [Volpe et al., 2013]. As already described above, plant transpiration is mainly driven by external stressors (i.e. atmosphere and weather conditions). Therefore, also for this synthetic model, it is necessary to take into account meteorological information to determine the atmospheric forcing. In this case we took advantage of a real dataset measured from the meteorological station at the Bulgherano field site (see chap. 3), which consisted of photosynthetically active radiation, relative humidity, and temperature, all measured at a height of 4 m, except for PAR, which was measured at 8 m. The acquisitions took place on a hourly basis from 25^{th} September 2013 to 24^{th} October 2013. On the basis of these data, we considered precipitation negligible.

Plant parameters			
Parameter	Symbol	Value	Reference
Plant height	h_{cano}	3.75 m	Measured
Projected canopy area	A_{cano}	12.5 m^2	Measured
Xylem area	A_{xylem}	0.09 m^2	Measured
Root conductance	g_r	9E-10 s^{-1}	Assumed
Leaf area index	LAI	4.30	Measured
Xylem conductance			
Parameter	Symbol	Value	Reference
Maximum xylem conductance	$g_{x,max}$	9E-6 s^{-1}	Assumed
Vulnerability curve coefficient	d	200 m	Aspinwall et al. [2011] Volpe et al. [2013]
Vulnerability curve coefficient	c	2	Aspinwall et al. [2011] Volpe et al. [2013]
Photosynthetic model			
Parameter	Symbol	Value	Reference
Maximum carboxylation capacity at 25 °C	$V_{c,max25}$	98 μmol m^{-2} s^{-1}	Farquhar et al. [1980]
Michealis constant for CO_2 fixation at 25 °C	$K_{c,max25}$	300 μmol mol^{-1}	Volpe et al. [2013]
Michealis constant for O_2 fixation at 25 °C	$K_{o,max25}$	300 mmol mol^{-1}	Volpe et al. [2013]
CO_2 compensation point at 25 °C	$c_{p,25}$	2.6 mmol μmol^{-1}	Volpe et al. [2013]
Stomatal optimality model			
Parameter	Symbol	Value	Reference
Maximum marginal water use efficency	λ_{max}	4442.0 μmol mol^{-1}	Manzoni et al. [2011]
Empirical parameter	β	3.7E-05 m^{-2}	Manzoni et al. [2011]
Leaf potential at maximum λ	$\psi_{L,max}$	-145 m	Manzoni et al. [2011]
Apparent quantum yield	γ	0.015	Samuelson et al. [2001]
Relative H_2O/CO_2 diffusivity	a	1.6	Volpe et al. [2013]
Coefficient for g_s calculation	s	0.7	Volpe et al. [2013]
O_2 concentration in air	$C_{o,a}$	210 mmol mol^{-1}	Volpe et al. [2013]
Reference CO_2 concentration	$c*_a$	400 μmol mol^{-1}	Volpe et al. [2013]
Ambient CO_2 concentration	c_a	380 mmol mol^{-1}	Volpe et al. [2013]

Tab. 6.2: Plant parameters for the synthetic plant model. “Measured” is referred to parameters measured on trees at the Bulgherano field site (chap. 3), “assumed” describes parameters chosen in order to fit the modeled transpiration to the real transpiration (Fig. 6.5), while in the other cases the literature reference is indicated.

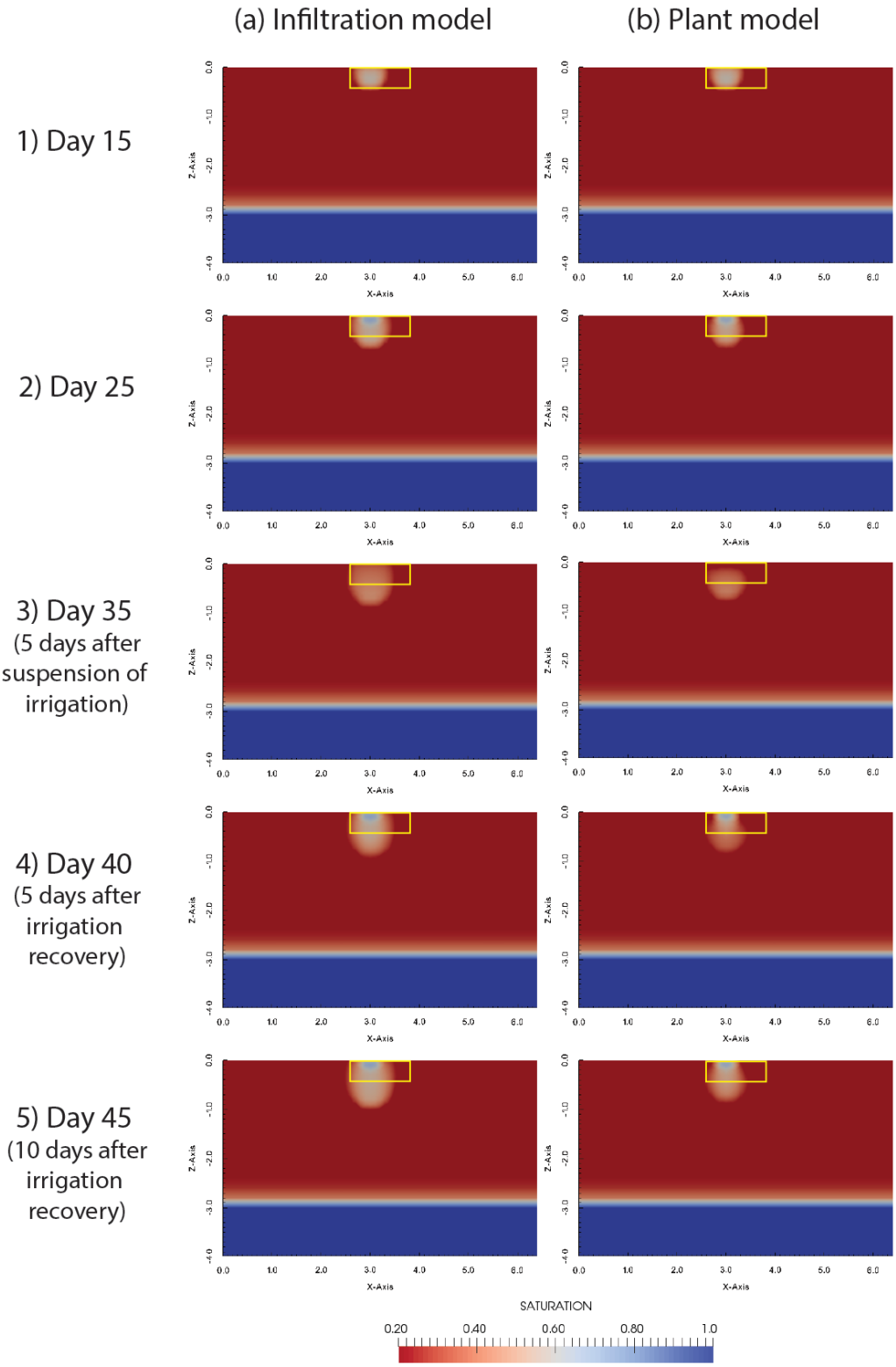

Fig. 6.5: Evolution of saturation over time as a consequence of water infiltration and root water uptake (a) in the infiltration model (i.e. without the plant) and (b) in the plant model. The yellow rectangle indicates the position of the root system. The influence of the plant activity is clearly visible especially after the suspension of irrigation.

The resulting transpiration is shown in Fig. 6.4 (red solid line) and is compared against the transpiration of a real orange tree located in the Bulgherano orchard, measured between 25^{th} September 2013 and 24^{th} October 2013 (black dotted line in Fig. 6.4). Despite some discrepancies, the synthetic transpiration shows the same trend of the real one, except for the nocturnal activity, which is not modeled. This allowed us to verify the plant activity, which is actually very similar to that of a real tree. Nevertheless, it has to be underlined once again that our aim is not to obtain an exact representation of the activity of a known plant, but to develop a synthetic model resembling a real tree insted, to get a known water content distribution recalling the ERT data.

Fig. 6.5(b) displays the variation of saturation over time. The effect of root water uptake is particularly clear after the suspension of irrigation (i.e. point 3) in Fig. 6.5), especially if compared to the infiltration model results.

6.3 Transpiration reconstruction and discussion

The reconstruction of plant transpiration b_T^R in this synthetic case study is performed on the basis of the outputs of the previous models, i.e. the infiltration model and the plant model. In particular, we performed two different transpiration reconstructions, namely the "exact reconstruction" and the "approximated reconstruction". Here, we present the results for $t = 392400$ s, i.e. at 12:00 pm of the 20^{th} day.

The "exact reconstruction" (Fig. 6.6(b)) is aimed at assessing b_T^R without introducing any approximation. This is possible only in this synthetic case study, as all the necessary terms are available (i.e. also $\hat{\theta}_M^k$, see sec. 5.5). As expected, we are capable of recreating the real distribution and magnitude of the transpiration provided by the plant model, as shown in Fig. 6.6.

The "approximated reconstruction", on the contrary, is shown in Fig. 6.7(b). By comparing this image with Fig. 6.7(a) (i.e. the real plant transpiration from the model in sec. 6.2), it is clear that the reconstruction is not as good as in the previous case. This is a consequence of all the approximations introduced during the numerical procedure, which can be summarized as:

i Approximations due to Taylor series, as we are omitting all the terms with order higher than 2. In fact, eq. (5.64) is expanded up to the Jacobian of b_T^R, thus the Hessian, for instance, is not considered;

ii Approximation due to the omission of the term described in eq. (5.67), since $\hat{\theta}_M^k$ needs to be approximated as well, as it is not available in a real case study;

iii Approximations due to the estimation of the Jacobians in eq. (5.68), eq. (5.69), and eq. (5.70), here performed by means of the finite difference method.

Despite the difference between the real and the approximated transpiration, mainly in terms of magnitude (Fig. 6.7), it is important to underline that, however, our procedure allowed to locate the position of the active root zone, as depicted in Fig. 6.8. This is a very important result, especially if considering all the approximations introduced and described above. Furthermore, this first approximated

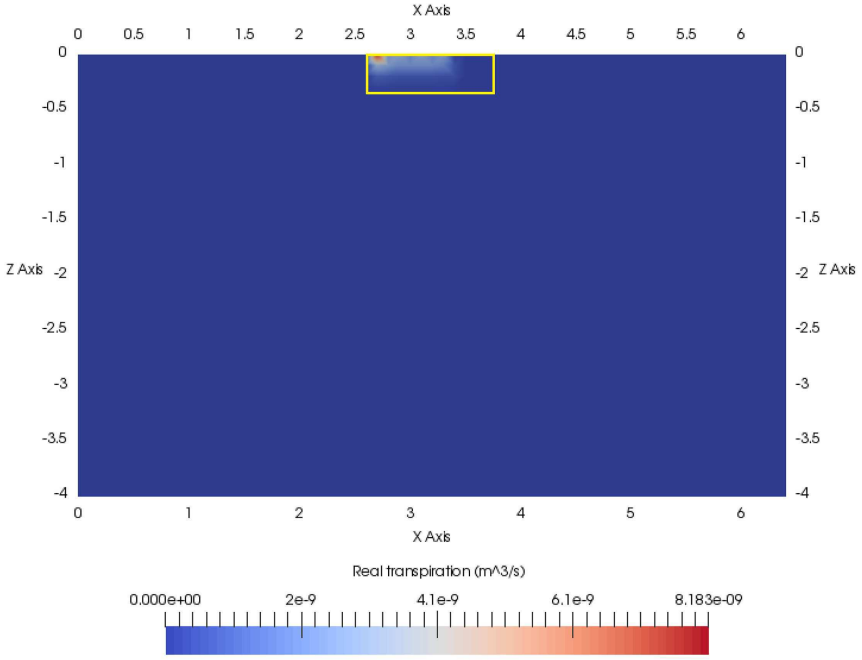

(a) Real transpiration

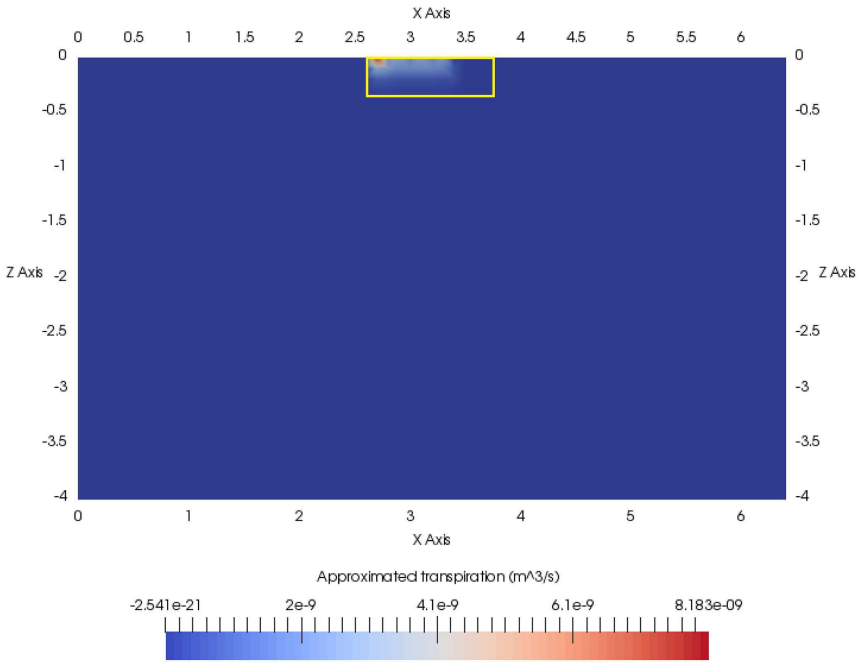

(b) Exact reconstruction

Fig. 6.6: Comparison between (a) the real transpiration and (b) the exact reconstruction on a vertical section. The yellow rectangle locates the root system position.

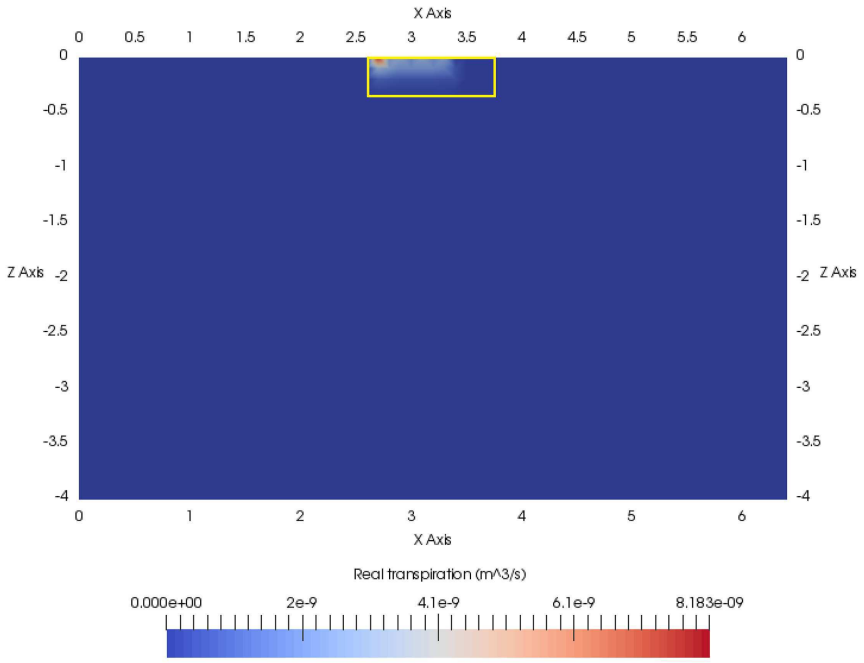

(a) Real transpiration

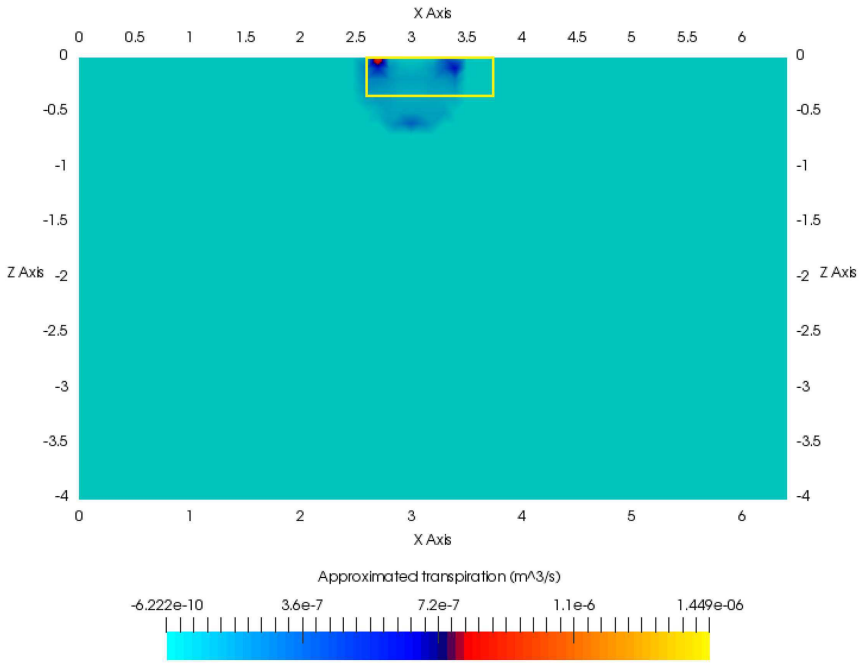

(b) Approximated reconstruction

Fig. 6.7: Comparison between (a) the real transpiration and (b) the approximated reconstruction on a vertical section. The yellow rectangle locates the root system position.

result shows as the potentialities of the proposed method, which still need to be fully exploited by a more accurate numerical procedure, aimed at estimating more accurately the first order terms and $\hat{\theta}_M^k$ in eq. (5.64).

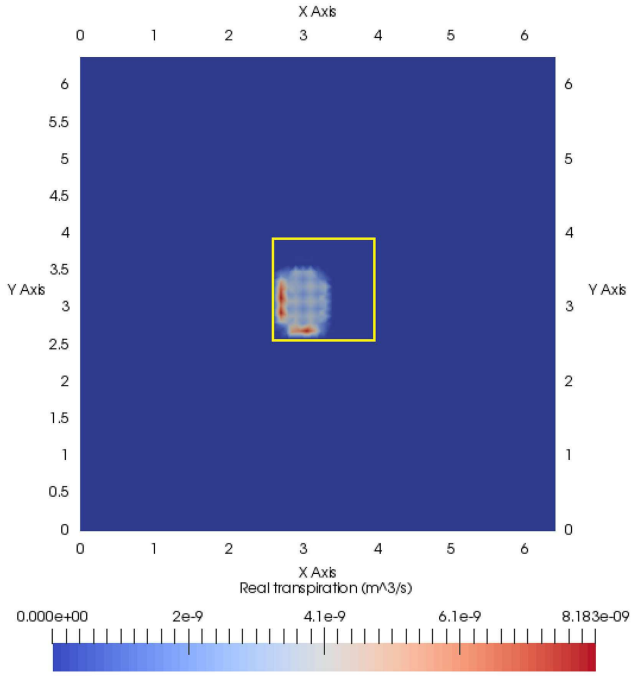

(a) Real transpiration

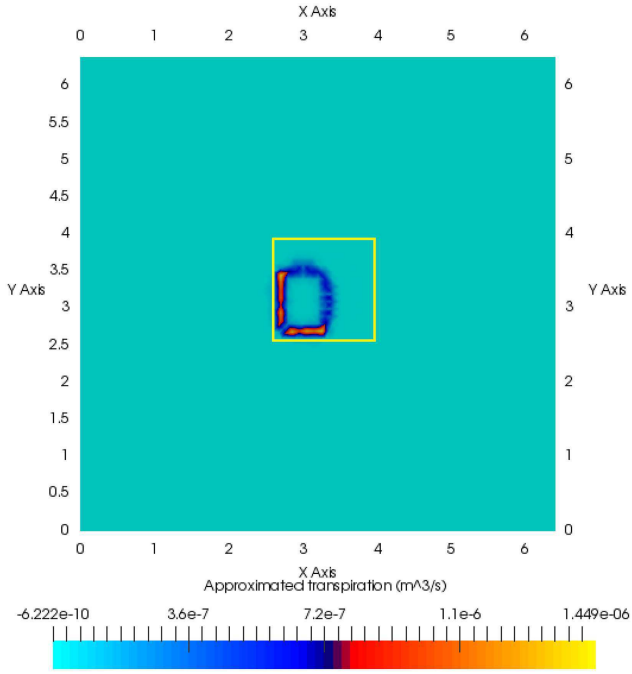

(b) Approximated reconstruction

Fig. 6.8: Comparison between (a) the real transpiration and (b) the approximated reconstruction as seen from top. The yellow square locates the root system position.

7

Conclusions

***

The Soil–Plant continuum is one of the main subdomains of the Earth's critical zone and plays a crucial role in the exchanges of mass and energy between soil and atmosphere. Nevertheless, the localization of the active root zone (i.e. the portion of the root system involved in the water uptake) is still in an early stage, despite its undeniable importance for many practical applications, first and foremost precision irrigation. Therefore, in this dissertation geophysical measurements and hydrological modeling have been proposed and described to characterize the active root zone of different orange trees.

The ERT results here presented well highlight the spatial and temporal resistivity patterns occurring in the root zone of the considered plants. In particular, the importance and novelty of the data at our disposal rely on the combination of measurements with and without the active tree in the Bulgherano field site, and on the comparison of trees drip irrigated with different treatments in Palazzelli. In absolute terms, the variability of resistivity is likely due to a combination of root distribution and preferential water pathways toward the roots (Palazzelli) or is mainly an expression of the low soil water content (Bulgherano). However, the most interesting results are certainly provided by the time–lapse monitoring, which highlights the occurring and interacting processes from a dynamic perspective. In both case studies, our data highlight the areas which che be considered as location of the active root zone. In particular, at the Bulgherano field site it is confined in the upper 0.4 m of the subsoil, while at the Palazzelli field site a switch of tree water source seems to occur, from the deeper soil profile (at the beginning of the irrigation season), to shallow water source points (during the irrigation phase). Also the short–term monitoring shows clear, although difficult to interpret univocally, variations in terms of resistivity.

Therefore, even if these ERT data are rich in information, their complete exploitation requires an appropriate combination with hydrological modeling. The innovative numerical procedure here developed is based on several assumptions and approximations that need to be introduced in order to deal with the interacting nonlinear processes occurring. The reconstructed transpiration here presented, albite not completely satisfying, provides interesting insights into the potentialities of the methods, which appears to be promising for a future application on a real case. In particular, this first attempt allowed us to locate the active root zone in a synthetic case study. However, some considerable improvements are required to better estimate also the magnitude of the fluxes taking place.

In conclusion, the combination of geophysical measurements and hydrological

modeling provides interesting and innovative insights into the Soil–Plant continuum dynamics. To fully take advantage of the proposed procedure, an accurate planning is mandatory, in order to develop the field campaign on the basis of the future numerical application. Although rather complex, this approach allows changing the interpretation point of view from simply qualitative (as mainly shown in the literature) to quantitative, with evident advantages for practical applications.

7.1 Challenges for future research

The results described throughout this dissertation lead to future research opportunities for both ERT and modeling applications. First of all, the geophysical measurements should be repeated on other orange trees, especially in the Palazzelli field site, so as to increase the robustness of the ERT monitoring results. This can be done adopting different measurement schemes (e.g. variating the skip) and/or employing new micro–boreholes installation techniques. Moreover, the ERT data should be combined with measurements of the soil suction in the root zone.

However, the main future challenges concern the procedure here presented to locate the active root zone. This not only means facing the issues and the approximations describes before, but also moving from a synthetic example to a real dataset. Thus, further uncertainties will be introduced at all steps of the procedure, from the geophysical acquisition, to the hydrological model. Nevertheless, such an application would be completely innovative and suitable also for other types of plants, thus increasing the knowledge of the Soil–Plant continuum with relevant advantages for the water resource exploitation

Acknowledgments

***

I wish to acknowledge the EU FP7 project GLOBAQUA ("Managing the effects of multiple stressors on aquatic ecosystems under water scarcity") for the support. I also wish to thank the Agro-meteorological Service of the Sicilian Region for supporting field campaigns.

I would like to acknowledge my supervisor Prof. Giorgio Cassiani and my co–supervisor Dott. Jacopo Boaga for the opportunities they gave me during this Ph.D. course, for their precious advices, and for their honest opinions. I also thank the other members, present and past, of the geophysical group at Unipd: dott.ssa Maria Teresa Perri and dott. Matteo Rossi, for their help and support. The second acknowledgment goes to Prof. Mario Putti, dott. Gabriele Manoli, and dott. Damiano Pasetto for their careful guidance and infinite patience during the modeling phase. Their teaching allowed me facing for the first time the difficulties (and pleasures) of hydrological modeling and without their help this thesis would not have been completed. I would also like to thank Prof. Simona Consoli, for the constructive collaboration and the kind welcome in Sicily, and Prof. Andy Binley, for the wonderful time spent at Lancaster University under his supervision, despite Storm Desmond and the following flood and blackout (it was a "record–breaking wet November", after all!). A special acknowledgement goes to Daniela Vanella. We shared a house and two cats for three months, as well as huge datasets and modeling problems, but your laughs surely simplified everything. Plus, your real "pasta di mandorle" is always welcome! Finally, I would like to thank my family for the strong support during the good and the bad times in these last years.

Bibliography

***

Aiello, R., V. Bagarello, S. Barbagallo, S. Consoli, S. Di Prima, G. Giordano, and M. Iovino, 2014. An assessment of the Beerkan method for determining the hydraulic properties of a sandy loam soil. *Geoderma*, 235, 300–307, doi:10.1016/j.geoderma.2014.07.024.

al Hagrey, S. A., 2007. Geophysical imaging of root–zone, trunk, and moisture heterogeneity. *Journal of Experimental Botany*, 58(4), 839–854.

al Hagrey, S. A. and T. Petersen, 2011. Numerical and experimental mapping of small root zones using optimized surface and borehole resistivity tomography. *Geophysics*, 76(2), G25–G35.

Allen, R. G., L. S. Pereira, D. Raes, and M. Smith, 1998. Crop evapotranspiration: guidelines for computing crop water requirements. *Irrigation and Drainage Paper No. 56.*, 300(9), D05109.

Allen, R. G., W. O. Pruitt, J. L. Wright, T. A. Howell, F. Ventura, R. Snyder, D. Itenfisu, P. Steduto, J. Berengena, J. Baselga Yrisarry, M. Smith, L. S. Pereira, D. Raes, A. Perrier, I. Alves, and I. Walter, 2006. A recommendation on standardized surface resistance for hourly calculation of reference ET_o by the FAO56 Penman–Monteith method. *Agricultural Water Management*, 81(1), 1–22.

Amato, M., B. Basso, G. Celano, G. Bitella, G. Morelli, and R. Rossi, 2008. In situ detection of tree root distribution and biomass by multi–electrode resistivity imaging. *Tree physiology*, 28(10), 1441–1448.

Amato, M., G. Bitella, R. Rossi, J. A. Gómez, S. Lovelli, and J. J. F. Gomes, 2009. Multi–electrode 3d resistivity imaging of alfalfa root zone. *European Journal of Agronomy*, 31(4), 213–222.

Amato, M., R. Rossi, G. Bitella, and S. Lovelli, 2010. Multielectrode geoelectrical tomography for the quantification of plant roots. *Italian Journal of Agronomy*, 5(3), 257–264.

Archie, G. E., 1942. The electrical resistivity log as an aid in determining some reservoir characteristics. *Transactions of the AIME*, 146(01), 54–62.

Aspinwall, M. J., J. S. King, J.-C. Domec, S. E. McKeand, and F. Isik, 2011. Genetic effects on transpiration, canopy conductance, stomatal sensitivity to vapour pressure deficit, and cavitation resistance in loblolly pine. *Ecohydrology*, 4(2), 168–182, doi:10.1002/eco.197.

Aubinet, M., A. Grelle, A. Ibrom, Ü. Rannik, J. Moncrieff, T. Foken, A. Kowalski, P. Martin, P. Berbigier, C. Bernhofer, R. Clement, J. Elbers, A. Granier, T. Grünwald, K. Morgenstern, K. Pilegaard, C. Rebmann, W. Snjiders, R. Valentini, and T. Vesala, 1999. Estimates of the annual net carbon and water exchange of forests: the EUROFLUX methodology. *Advances in ecological research*, 30, 113–175.

Banwart, S. A., J. Chorover, J. Gaillardet, D. Sparks, T. White, S. Anderson, A. Aufdenkampe, S. Bernasconi, S. L. Brantley, O. Chadwick, W. E. Dietrich, C. Duffy, M. Goldhaber, and K. Lehnert, 2013. Sustaining Earth's critical zone basic science and interdisciplinary solutions for global challenges. *University of Sheffield, Sheffield*, p. 47.

Binley, A., 2013. R3t, version 1.8. http://www.es.lancs.ac.uk/people/amb/Freeware/R3t/R3t.htm.

Binley, A., 2015. Tools and techniques: Electrical methods. In G. Schubert, editor, *Treatise on Geophysics (Second Edition)*, chapter 11.08, pp. 233 – 259, Elsevier, Oxford, second edition, doi:http://dx.doi.org/10.1016/B978-0-444-53802-4.00192-5.

Binley, A., G. Cassiani, and R. Deiana, 2010. Hydrogeophysics: Opportunities and challenges. *Bollettino di Geofisica Teorica ed Applicata*, 51(4), 267–284.

Binley, A., G. Cassiani, R. Middleton, and P. Winship, 2002. Vadose zone flow model parameterisation using cross–borehole radar and resistivity imaging. *Journal of Hydrology*, 267(3), 147–159.

Binley, A., S. S. Hubbard, J. A. Huisman, A. Revil, D. A. Robinson, K. Singha, and L. D. Slater, 2015. The emergence of hydrogeophysics for improved understanding of subsurface processes over multiple scales. *Water resources research*, 51(6), 3837–3866, doi:10.1002/2015WR017016.

Binley, A. and A. Kemna, 2005. DC resistivity and induced polarization methods. In Y. Rubin and S. S. Hubbard, editors, *Hydrogeophysics*, chapter 5, pp. 129 – 156, Springer Science & Business Media, first edition.

Binley, A., A. Ramirez, and W. Daily, 1995. Regularised image reconstruction of noisy electrical resistance tomography data. In *Process Tomography – 1995, Proceedings of the 4th Workshop of the European Concerted Action on Process Tomography, Bergen*, pp. 6–8.

Boaga, J., M. Rossi, and G. Cassiani, 2013. Monitoring soil–plant interactions in an apple orchard using 3D electrical resistivity tomography. *Procedia Environmental Sciences*, 19, 394–402.

Brantley, S. L., M. B. Goldhaber, and K. V. Ragnarsdottir, 2007. Crossing disciplines and scales to understand the critical zone. *Elements*, 3(5), 307–314.

Brooks, R. H. and A. T. Corey, 1964. Hydraulic properties of porous media and their relation to drainage design. *Transactions of the ASAE*, 7(1), 26–0028.

Brovelli, A. and G. Cassiani, 2011. Combined estimation of effective electrical conductivity and permittivity for soil monitoring. *Water Resources Research*, 47(8).

Burdine, N. T., 1953. Relative permeability calculations from pore size distribution data. *Journal of Petroleum Technology*, 5(03), 71–78, doi:10.2118/225-G.

Busato, L., J. Boaga, L. Peruzzo, M. Himi, S. Cola, S. Bersan, and G. Cassiani, 2016. Combined geophysical surveys for the characterization of a reconstructed river embankment. *Engineering Geology*, 211, 74–84.

Camporese, M., G. Cassiani, R. Deiana, P. Salandin, and A. Binley, 2015. Coupled and uncoupled hydrogeophysical inversions using ensemble kalman filter assimilation of ert–monitored tracer test data. *Water Resources Research*, 51(5), 3277–3291, doi:10.1002/2014WR016017.

Camporese, M., C. Paniconi, M. Putti, and S. Orlandini, 2010. Surface–subsurface flow modeling with path–based runoff routing, boundary condition–based coupling, and assimilation of multisource observation data. *Water Resources Research*, 46, W02512, doi:10.1029/2008WR007536.

Cassiani, G., J. Boaga, D. Vanella, M. T. Perri, and S. Consoli, 2015. Monitoring and modelling of soil–plant interactions: the joint use of ERT, sap flow and eddy covariance data to characterize the volume of an orange tree root zone. *Hydrology and Earth System Sciences*, 19(5), 2213–2225.

Cassiani, G., V. Bruno, A. Villa, N. Fusi, and A. M. Binley, 2006. A saline trace test monitored via time-lapse surface electrical resistivity tomography. *Journal of Applied Geophysics*, 59(3), 244–259.

Chapin, F. S., A. J. Bloom, C. B. Field, and R. H. Waring, 1987. Plant responses to multiple environmental factors. *Bioscience*, 37(1), 49–57.

Chorover, J., R. Kretzschmar, F. Garcia-Pichel, and D. L. Sparks, 2007. Soil biogeochemical processes within the critical zone. *Elements*, 3(5), 321–326.

Cohen, Y., M. Fuchs, and S. Cohen, 1983. Resistance to water uptake in a mature citrus tree. *Journal of Experimental Botany*, 34(4), 451–460.

Consoli, S., F. Stagno, G. Roccuzzo, G. L. Cirelli, and F. Intrigliolo, 2014. Sustainable management of limited water resources in a young orange orchard. *Agricultural Water Management*, 132, 60–68.

Constable, S. C., R. L. Parker, and C. G. Constable, 1987. Occam's inversion: A practical algorithm for generating smooth models from electromagnetic sounding data. *Geophysics*, 52(3), 289–300.

Daily, W., A. Ramirez, A. Binley, and D. LeBrecque, 2004. Electrical resistance tomography. *The Leading Edge*, 23(5), 438–442.

Daily, W., A. Ramirez, D. LaBrecque, and J. Nitao, 1992. Electrical resistivity tomography of vadose water movement. *Water Resources Research*, 28(5), 1429–1442.

Dasberg, S. and D. Or, 1999. *Practical Applications of Drip Irrigation*. Springer.

Deiana, R., G. Cassiani, A. Kemna, A. Villa, V. Bruno, and A. Bagliani, 2007. An experiment of non–invasive characterization of the vadose zone via water injection and cross–hole time–lapse geophysical monitoring. *Near Surface Geophysics*, 5(3), 183–194.

Department of Agriculture and Food, Government of Western Australia, 2016. Citrus irrigation recommendations in Western Australia. https://agric.wa.gov.au/n/1551, accessed: August 2016.

Farquhar, G. D., S. von Caemmerer, and J. A. Berry, 1980. A biochemical model of photosynthetic CO_2 assimilation in leaves of C_3 species. *Planta*, 149(1), 78–90.

Fereres, E. and M. A. Soriano, 2007. Deficit irrigation for reducing agricultural water use. *Journal of experimental botany*, 58(2), 147–159.

Friedman, S. P., 2005. Soil properties influencing apparent electrical conductivity: a review. *Computers and electronics in agriculture*, 46(1), 45–70.

Garré, S., M. Javaux, J. Vanderborght, L. Pagès, and H. Vereecken, 2011. Three–dimensional electrical resistivity tomography to monitor root zone water dynamics. *Vadose Zone Journal*, 10(1), 412–424.

Gee, G. W. and J. W. Bauder, 1986. Particle–size analysis. In A. Klute, editor, *Methods of Soil Analysis, Part 1, Physical and Mineralogical Methods, Agronomy Monograph No. 9*, pp. 383 – 411, American Society of Agronomy/Soil Science Society of American, Madison, WI, second edition.

Geuzaine, C. and J.-F. Remacle, 2009. Gmsh: A 3–d finite element mesh generator with built–in pre–and post–processing facilities. *International Journal for Numerical Methods in Engineering*, 79(11), 1309–1331.

Green, S., B. Clothier, and B. Jardine, 2003. Theory and practical application of heat pulse to measure sap flow. *Agronomy Journal*, 95(6), 1371–1379.

Griffiths, D. H. and J. Turnbull, 1985. A multi-electrode array for resistivity surveying. *First break*, 3(7), 16–20.

Hallof, P. G., 1957. *On the interpretation of resistivity and induced polarization field measurements*. Ph.D. thesis, Massachusetts Institute of Technology.

Hinnell, A. C., T. P. A. Ferré, J. A. Vrugt, J. A. Huisman, S. Moysey, J. Rings, and M. B. Kowalsky, 2010. Improved extraction of hydrologic information from geophysical data through coupled hydrogeophysical inversion. *Water resources research*, 46(4), doi:10.1029/2008WR007060.

Huyakorn, P. S., S. D. Thomas, and B. M. Thompson, 1984. Techniques for making finite elements competitive in modeling flow in variably saturated porous media. *Water Resources Research*, 20(8), 1099–1115.

Jarvis, N. J., 2011. Simple physics–based models of compensatory plant water uptake: Concepts and eco–hydrological consequences. *Hydrology and Earth System Sciences*, 15(11), 3431–3446.

Jayawickreme, D. H., E. G. Jobbágy, and R. B. Jackson, 2014. Geophysical subsurface imaging for ecological applications. *New Phytologist*, 201(4), 1170–1175.

Jayawickreme, D. H., R. L. Van Dam, and D. W. Hyndman, 2008. Subsurface imaging of vegetation, climate, and root–zone moisture interactions. *Geophysical Research Letters*, 35(18).

Jury, W. A., D. Or, Y. Pachepsky, H. Vereecken, J. W. Hopmans, L. R. Ahuja, B. E. Clothier, K. L. Bristow, G. J. Kluitenberg, P. Moldrup, J. Šimůnek, M. T. van Genuchten, and R. Horton, 2011. Kirkham's legacy and contemporary challenges in soil physics research. *Soil Science Society of America Journal*, 75(5), 1589–1601.

Kemna, A., 2000. *Tomographic inversion of complex resistivity: Theory and application*. Der Andere Verlag Osnabrück, Germany.

Kemna, A., B. Kulessa, and H. Vereecken, 2002. Imaging and characterisation of subsurface solute transport using electrical resistivity tomography (ert) and equivalent transport models. *Journal of Hydrology*, 267(3), 125–146.

Keyes, S. D., K. R. Daly, N. J. Gostling, D. L. Jones, P. Talboys, B. R. Pinzer, R. Boardman, I. Sinclair, A. Marchant, and T. Roose, 2013. High resolution synchrotron imaging of wheat root hairs growing in soil and image based modelling of phosphate uptake. *New Phytologist*, 198(4), 1023–1029, doi:10.1111/nph.12294.

Koestel, J., J. Vanderborght, M. Javaux, A. Kemna, A. Binley, and H. Vereecken, 2009. Noninvasive 3–d transport characterization in a sandy soil using ert: 1. investigating the validity of ert–derived transport parameters. *Vadose Zone Journal*, 8(3), 711–722.

Kotur, S. C. and S. V. Keshava Murthy, 1998. Root activity distribution studies in citrus, grape, mango and guava using isotopic techniques. *Karnataka J. Agric. Sci*, 11, 651–657.

LaBrecque, D. J., M. Miletto, W. Daily, A. Ramirez, and E. Owen, 1996. The effects of noise on Occam's inversion of resistivity tomography data. *Geophysics*, 61(2), 538–548.

Lambers, H., F. S. Chapin III, and T. L. Pons, 2008a. Photosynthesis. In *Plant physiological ecology*, pp. 11–99, Springer.

Lambers, H., F. S. Chapin III, and T. L. Pons, 2008b. *Plant physiological ecology*. Springer, ISBN 978-0-387-78341-3.

Leij, F. J., W. J. Alves, and M. T. van Genuchten, 1996. *The UNSODA unsaturated soil hydraulic database: user's manual*, volume 96. National Risk Management Research Laboratory, Office of Research and Development, US Environmental Protection Agency.

Lin, H., 2010. Earth's Critical Zone and hydropedology: concepts, characteristics, and advances. *Hydrology and Earth System Sciences*, 14(1), 25.

Lynch, J., 1995. Root architecture and plant productivity. *Plant physiology*, 109(1), 7.

Mancuso, S., 2011. *Measuring roots: an updated approach*. Springer Science & Business Media.

Manoli, G., S. Bonetti, J.-C. Domec, M. Putti, G. Katul, and M. Marani, 2014. Tree root systems competing for soil moisture in a 3d soil–plant model. *Advances in Water Resources*, 66, 32 – 42, doi:10.1016/j.advwatres.2014.01.006.

Manoli, G., S. Bonetti, E. Scudiero, F. Morari, M. Putti, and P. Teatini, 2015. Modeling Soil–Plant Dynamics: Assessing Simulation Accuracy by Comparison with Spatially Distributed Crop Yield Measurements. *Vadose Zone Journal*, 14(12).

Manzoni, S., G. Vico, G. Katul, P. A. Fay, W. Polley, S. Palmroth, and A. Porporato, 2011. Optimizing stomatal conductance for maximum carbon gain under water stress: a meta–analysis across plant functional types and climates. *Functional Ecology*, 25(3), 456–467.

Michot, D., Y. Benderitter, A. Dorigny, B. Nicoullaud, D. King, and A. Tabbagh, 2003. Spatial and temporal monitoring of soil water content with an irrigated corn crop cover using surface electrical resistivity tomography. *Water Resources Research*, 39(5).

Moreno, P., S. Ambrós, M. R. Albiach-Martí, J. Guerri, and L. Peña, 2008. Citrus tristeza virus: a pathogen that changed the course of the citrus industry. *Molecular Plant Pathology*, 9(2), ISSN 1364-3703, doi:10.1111/j.1364-3703.2007.00455.x.

Motisi, A., F. Rossi, S. Consoli, R. Papa, M. Minacapilli, G. Rallo, C. Cammalleri, and G. D'urso, 2012. Eddy Covariance and Sap Flow Measurement of Energy and Mass Exchanges of Woody Crops in a Mediterranean Environment. *Acta Horticulturae*, 951, 121–127.

National Research Council, 1991. *Opportunities in the Hydrologic Sciences*. The National Academies Press, Washington, DC, doi:10.17226/1543.

National Research Council, 2001. *Basic Research Opportunities in Earth Science*. National Academy Press.

Nijland, W., M. Van der Meijde, E. A. Addink, and S. M. De Jong, 2010. Detection of soil moisture and vegetation water abstraction in a mediterranean natural area using electrical resistivity tomography. *Catena*, 81(3), 209–216.

Nilson, S. E. and S. M. Assmann, 2007. The control of transpiration. Insights from Arabidopsis. *Plant physiology*, 143(1), 19–27.

Nyquist, J. E. and M. J. S. Roth, 2005. Improved 3d pole–dipole resistivity surveys using radial measurement pairs. *Geophysical Research Letters*, 32(21), L21416, doi:10.1029/2005GL024153.

Orghidan, T., 2010. A new habitat of subsurface waters: the hyporheic biotope. *Fundamental and applied limnology*, 176(4), 291.

Orlandini, S. and R. Rosso, 1996. Diffusion wave modeling of distributed catchment dynamics. *Journal of Hydrologic Engineering*, 1(3), 103–113, doi:10.1061/(ASCE)1084-0699(1996)1:3(103).

Paniconi, C. and M. Putti, 1994. A comparison of Picard and Newton iteration in the numerical solution of multidimensional variably saturated flow problems. *Water Resources Research*, 30(12), 3357–3374.

Paniconi, C. and E. F. Wood, 1993. A detailed model for simulation of catchment scale subsurface hydrologic processes. *Water Resources Research*, 29(6), 1601–1620.

Parasnis, D., 1988. Reciprocity theorems in geoelectric and geoelectromagnetic work. *Geoexploration*, 25(3), 177 – 198, doi:10.1016/0016-7142(88)90014-2.

Passioura, J. B., 1982. Water in the soil–plant–atmosphere continuum. In *Physiological Plant Ecology II*, pp. 5–33, Springer.

Pinton, R., Z. Varanini, and P. Nannipieri, 2007. *The rhizosphere: biochemistry and organic substances at the soil–plant interface*. CRC press.

Porporato, A., P. D'odorico, F. Laio, L. Ridolfi, and I. Rodriguez-Iturbe, 2002. Ecohydrology of water–controlled ecosystems. *Advances in Water Resources*, 25(8), 1335–1348.

Richter, D. and M. L. Mobley, 2009. Monitoring Earth's Critical Zone. *Science*, 326(5956), doi: 10.1126/science.1179117.

Ritchie, J. T., 1981. Water dynamics in the soil–plant–atmosphere system. *Soil Water and Nitrogen in Mediterranean–Type Environments*, pp. 81–96.

Rodriguez-Iturbe, I. and A. Porporato, 2004. Ecohydrology of water controlled ecosystems: plants and soil moisture dynamics.

Rossi, M., G. Manoli, D. Pasetto, R. Deiana, S. Ferraris, C. Strobbia, M. Putti, and G. Cassiani, 2015. Coupled inverse modeling of a controlled irrigation experiment using multiple hydro-geophysical data. *Advances in Water Resources*, 82, 150–165, doi: 10.1016/j.advwatres.2015.03.008.

Rossi, R., M. Amato, G. Bitella, R. Bochicchio, J. J. Ferreira Gomes, S. Lovelli, E. Martorella, and P. Favale, 2011. Electrical resistivity tomography as a non–destructive method for mapping root biomass in an orchard. *European Journal of Soil Science*, 62(2), 206–215.

Rubin, Y. and S. S. Hubbard, 2005. *Hydrogeophysics*. Springer Science & Business Media.

Sadler, E. J., R. G. Evans, K. C. Stone, and C. R. Camp, 2005. Opportunities for conservation with precision irrigation. *Journal of soil and water conservation*, 60(6), 371–378.

Samuelson, L., T. Stokes, T. Cooksey, and P. McLemore, 2001. Production efficiency of loblolly pine and sweetgum in response to four years of intensive management. *Tree Physiology*, 21(6), 369–376.

Schiefelbein, J. W. and P. N. Benfey, 1991. The development of plant roots: new approaches to underground problems. *The Plant Cell*, 3(11), 1147.

Schmidt, S., A. G. Bengough, P. J. Gregory, D. V. Grinev, and W. Otten, 2012. Estimating root–soil contact from 3D X–ray microtomographs. *European Journal of Soil Science*, 63(6), 776–786, doi:10.1111/j.1365-2389.2012.01487.x.

Schneider, C. L., S. Attinger, J.-O. Delfs, and A. Hildebrandt, 2010. Implementing small scale processes at the soil-plant interface–the role of root architectures for calculating root water uptake profiles. *Hydrology and Earth System Sciences*, 14(2), 279–289.

Scudeler, C., M. Putti, and C. Paniconi, 2016. Mass-conservative reconstruction of Galerkin velocity fields for transport simulations. *Advances in Water Resources*, 94, 470–485.

Segal, E., T. Kushnir, Y. Mualem, and U. Shani, 2008. Water uptake and hydraulics of the root hair rhizosphere. *Vadose Zone Journal*, 7(3), 1027–1034.

Seidel, K. and G. Lange, 2007. Direct current resistivity methods. In K. Knödel, G. Lange, and H.-J. Voigt, editors, *Environmental geology: Handbook of field methods and case studies*, chapter 4.3, pp. 205–237, Springer, first edition.

Srayeddin, I. and C. Doussan, 2009. Estimation of the spatial variability of root water uptake of maize and sorghum at the field scale by electrical resistivity tomography. *Plant and Soil*, 319(1-2), 185–207.

Swanson, R. H. and D. W. Whitfield, 1981. A numerical analysis of heat pulse velocity theory and practice. *Journal of Experimental Botany*, 32(1), 221–239.

Tenhunen, J. D., F. M. Catarino, O. L. Lange, and W. C. Oechel, 2013. *Plant response to stress: functional analysis in mediterranean ecosystems*, volume 15. Springer Science & Business Media.

Tikhonov, A. N. and V. Y. Arsenin, 1977. *Solutions of ill–posed problems*. Winston.

Ursino, N., G. Cassiani, R. Deiana, G. Vignoli, and J. Boaga, 2014. Measuring and modeling water–related soil–vegetation feedbacks in a fallow plot. *Hydrology and Earth System Sciences*, 18(3), 1105–1118.

U.S. NSF National Program, 2016. Critical zone observatories. http://criticalzone.org/national/, accessed: September 2016.

Van Alphen, B. J. and J. J. Stoorvogel, 2000. A functional approach to soil characterization in support of precision agriculture. *Soil Science Society of America Journal*, 64(5), 1706–1713.

van Genuchten, M. T. and D. R. Nielsen, 1985. On describing and predicting the hydraulic properties of unsaturated soils. *Annales Geophysicae*, 3(5), 615–628.

Vanderborght, J., J. A. Huisman, J. Kruk, and H. Vereecken, 2013. Geophysical methods for field–scale imaging of root zone properties and processes. In S. H. Anderson and J. W. Hopmans, editors, *Soil–Water–Root Processes: Advances in Tomography and Imaging*, pp. 247–282, SSSA Special Publication 61.

Vereecken, H., A. Binley, G. Cassiani, A. Revil, and K. Titov, 2006. Applied hydrogeophysics. In A. Revil and K. Titov, editors, *NATO science series IV: earth and environmental sciences*, pp. 1–8, Springer, Dordrecht.

Volpe, V., M. Marani, J. Albertson, and G. Katul, 2013. Root controls on water redistribution and carbon uptake in the soil–plant system under current and future climate. *Advances in Water Resources*, 60, 110 – 120, doi:10.1016/j.advwatres.2013.07.008.

Waxman, M. H. and L. J. M. Smits, 1968. Electrical conductivities in oil–bearing shaly sands. *Society of Petroleum Engineers Journal*, 8(02), 107–122.

Werban, U., S. Attia al Hagrey, and W. Rabbel, 2008. Monitoring of root–zone water content in the laboratory by 2D geoelectrical tomography. *Journal of Plant Nutrition and Soil Science*, 171(6), 927–935.

Zanetti, C., A. Weller, M. Vennetier, and P. Mériaux, 2011. Detection of buried tree root samples by using geoelectrical measurements: a laboratory experiment. *Plant and soil*, 339(1-2), 273–283, doi:10.1007/s11104-010-0574-0.

A

Attachments

***

A.1 Time–lapse monitoring of the hyporheic zone of an alpine river using non–invasive methodologies 93
A.2 Combined geophysical surveys for the characterization of a reconstructed river embankment 102

A.1 Time–lapse monitoring of the hyporheic zone of an alpine river using non–invasive methodologies[1]

Introduction

The hyporheic zone (HZ) is the area located beneath and adjacent to rivers and streams, where the interactions between surface water and groundwater take place [Reidy and Clinton, 2004; Westhoff et al., 2011]. Therefore, this domain allows the transport of several substances (e.g., water, nutrients, and pollution) [Boulton et al., 1998] from a stream to the unconfined aquifer below, and vice versa, thus playing a fundamental role in the river ecosystem. The importance of the hyporheic zone in such a complex environment makes its characterization a goal shared by several disciplines, which range from applied geophysics to biogeochemistry, from hydraulics to ecology [Bridge J.W., 2005]: Regardless of the field of study, the main aim is always to completely describe the structures and the processes that distinguish this zone. Furthermore, flow and transport models are nowadays key instruments to efficiently characterize the HZ, given their ability of simulating surface water-groundwater exchange phenomena at a local scale [Constantz, 1998; Bianchin et al., 2010]. In order to achieve this common purposes, almost all these disciplines offer many invasive techniques that permit punctual in situ surveys and/or sample analysis [Bridge, 2005]; on the other hand, applied geophysics supplies a few non–invasive

[1]The contents of this attachment has been published in:
Busato L., J. Boaga, M.T. Perri, and G. Cassiani, 2014. Time–lapse monitoring of the hyporheic zone of an alpine river using non–invasive methodologies. In *Atti del 33° Convegno Nazionale GNGTS, Tema 3: Geofisica applicata*, pp. 129–135, ISBN: 978–88–940442–3–2.

methodologies (e.g., Electrical Resistivity Tomography – ERT – and Distributed Temperature Sensing – DTS), which allow a high resolution characterization of the hyporheic zone, overcoming the critical problem of measurements under riverbeds. In fact, ERT is a state–of–the–art technique for this kind of surveys, although it is commonly applied in a cross-well configuration or with a superficial electrodes deployment [Acworth and Dasey, 2003; Crook et. al, 2008]; conversely, the DTS usage in hydrogeophysics has been developing since the last decade, revealing a wide applicability to the typical issues of this field of study: Based on Raman scattering, this methodology employs heat as tracer and uses a fiber-optic cable to acquire temperature (T) values [Boulton et. al, 1998; Anderson, 2005; Selker et al., 2006; Lane, 2008].

In this work, we present the preliminary results (first year) regarding the characterization of the hyporheic zone of an alpine river (Vermigliana creek), obtained combining ERT and DTS time–lapse measurements. The typical ERT superficial data collection benefits from an innovative instrumentation deployment, which consists of both an ERT multicore cable and a DTS fiber–optic located in two separated boreholes drilled under the watercourse and perpendicular to it. These acquisition schemes led to high quality data capable to highlight some of the dynamics taking place in the HZ, which, however, still need to be coupled with a flow and transport model, in order to completely describe the domain of interest. The site and the results here described are part of the EU FP7 CLIMB (Climate Induced Changes on the Hydrology of Mediterranean Basins) project.

Creek and site description

The Vermigliana creek is the main watercourse of the Upper Val di Sole, Northern Italy, originates from the Presena Glacier (Presanella Group) and is one of the main tributaries of the Noce creek. Being the Vermigliana an alpine river, it presents a nivo–glacial regime, which entails higher flow rates during the summer (due to snow and glacial melting) and lower flow rates during the winter season. A variation in terms of discharges takes place also daily, since morning flow rates are on average higher than those in the late afternoon.

The whole valley bottom, where the Vermigliana flows, is entirely filled with heterogeneous glacial till and quaternary slope deposits, made up of material whose granulometry ranges from clays to boulders. Our site is located near the small village of Vermiglio (TN), 1165 meters above mean sea level.

Set–up and acquisitions

In order to characterize the HZ in our site, we combined two different methodologies, ERT and DTS. The former has been widely applied for this kind of surveys in many different sites, commonly using cross-well configurations and/or superficial cables [Acworth and Dasey, 2003; Crook et al., 2008]. Even if all these typical deployments lead to the acquisition of excellent data, we attempted to improve them by positioning part of the 72 total electrodes used inside the hyporheic zone (Fig. A.1): this was possible thanks to the horizontal directional drilling technology, which

allowed the remote–guided drilling of a horizontal borehole under the Vermigliana riverbed. The result consists of an 80 m long perforation under the watercourse that permitted the placement of a multicore cable with 48 brass electrodes, spaced 1 m, inside the HZ; these electrodes have a diameter of 30 mm and a length of 60 mm. The choice of brass electrodes is due to both economical and technical issues: on the one hand, brass is less expensive than graphite and stainless steel, but offers a lower resistance to water over time; on the other hand, this instrumentation will not be removed from the Vermigliana site and therefore an amortization of its high costs, with an usage in other case studies, will not be possible. To ensure a higher data reliability, we deployed also a superficial survey line of 24 stainless steel electrodes (12 on each river levee) spaced 1 m, in vertical correspondence to the horizontal borehole (Fig. A.1). Given the need of creating a single superficial deployment perpendicular to the river and the availability of a non–waterproof multicore cable for superficial surveys, 4 take–outs allowed the connection of the 4 electrodes nearest to the watercourse to the cable itself, which was partly located over the bridge upstream.

Each ERT survey is performed with an IRIS Syscal Pro resistivity meter using all 72 electrodes, with a skip–0 dipole-dipole scheme and duration of circa 30 minutes. The acquisition of both direct and reciprocal measurements (i.e., exchanging current electrodes with potential electrodes) permits the error assessment: in fact, each ERT sequence is made up of 4885 measurements, comprising both direct and reciprocal values. The latter, DTS (Distributed Temperature Sensing), has been employed in hydrogeophysics only for the last dozen of years. This methodology is based on the Raman effect, one of the scattering phenomena arising from the interaction between light photons and the noncrystalline structure of fiber-optic: Such an interaction generates a backscattered signal, whose intensity is temperature dependent [Selker et al., 2006]. Therefore, with an appropriate data processing, it is possible to compute how temperature varies along the whole fiber–optic cable. The usage of this methodology enables then to exploit heat as a natural tracer, showing its temporal and spatial changes in the domain of interest. Given our aim of characterizing the hyporheic zone of the Vermigliana creek, also for this technique we opted for an innovative deployment, which consists of a 200 m long fiber–optic located in a horizontal borehole a few meters downstream from the ERT perforation and parallel to it: Thus, also the fiber-optic is placed inside the HZ (Fig. A.1). For a better comprehension of the site geometry, it is necessary to underline that the DTS perforation has a 100 m linear length. Therefore, the fiber-optic is folded, creating the "double-ended" configuration required (i.e., both ends are connected to the DTS instrument).

For every DTS survey we used the AP Sensing N4386A Distributed Sensing system with a double–ended fiber–optic configuration, a sampling interval equal to 1 m and a spatial resolution equal to 1 m. In each survey, we acquired three single traces with update time and measurement time both equal to 30 s (i.e., every 30 seconds a new trace acquisition begins and lasts 30 seconds) and then averaged the three temperature values thus obtained for every sampling point: The result consists of a single profile with 200 temperature values, spaced 1 m one from the other.

The ERT time–lapse monitoring started in July 2013 and still is being carried out

approximately once or twice a month, mostly according to the weather conditions. On the other hand, we have been performing the DTS time–lapse monitoring since June 2014 approximately once a month. Because of the typical continental climate characterizing the Upper Val di Sole, the time–lapse monitoring (both ERT and DTS) can be performed only from spring to autumn, given the absence of snow and of seasonally frozen ground that would lead to high resistivity values and noisy data.

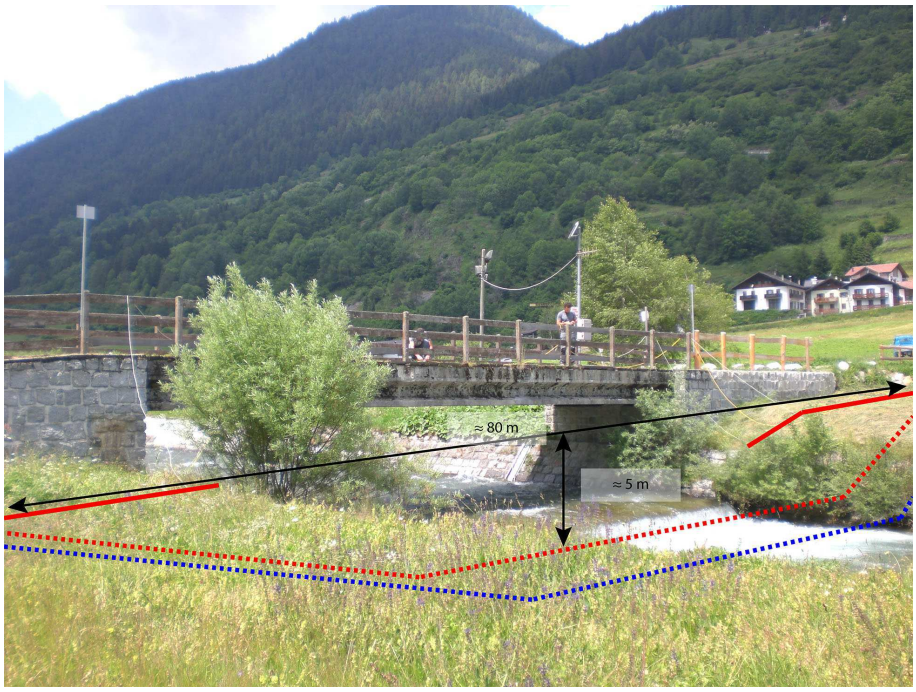

Fig. A.1: Vermigliana creek site (1165 meters above sea level). The red solid line represents the superficial ERT deployment on both levee surfaces, the red dotted line represents the ERT borehole deployment (under the Vermigliana creek, inside the hyporheic zone) and the blue dotted line represents the DTS fiber–optic under the watercourse. The DTS borehole is a few meters downstream from the ERT borehole and parallel to it.

Data processing, results and discussions

The ERT data at our disposal call for two different types of inversion. First of all, from each dataset (one from every survey) the correspondent absolute resistivity (ρ) cross–section is obtained with an appropriate inverse modeling, in order to represent the state of the hyporheic zone at the measurement time. After the error calculation based on the combination of each direct measurement with the correspondent reciprocal one, every dataset is refined applying an error threshold equal to 10%, which reduces each sequence to 1400 measurements on average. Despite 10% may seem a quite high error limit, it is perfectly compatible with the heterogeneous material whereof the investigated domain is composed (i.e., clay, tonalite boulders, gravelly–sand and silty deposits, as described by Dal Piaz et al. [2007]). Then, we performed the ERT data inversion thanks to the R2 code (Lancaster University, UK), fixing an error equal to 10% and using a triangular mesh with 5039 nodes and 9729 triangular

elements.

An example of the result of such a processing is the resistivity cross-section depicted in (Fig. A.2), representing the acquisition carried out on the 30^{th} August 2013. The resistivity distribution here illustrated is largely comparable to those of the other ERT surveys.

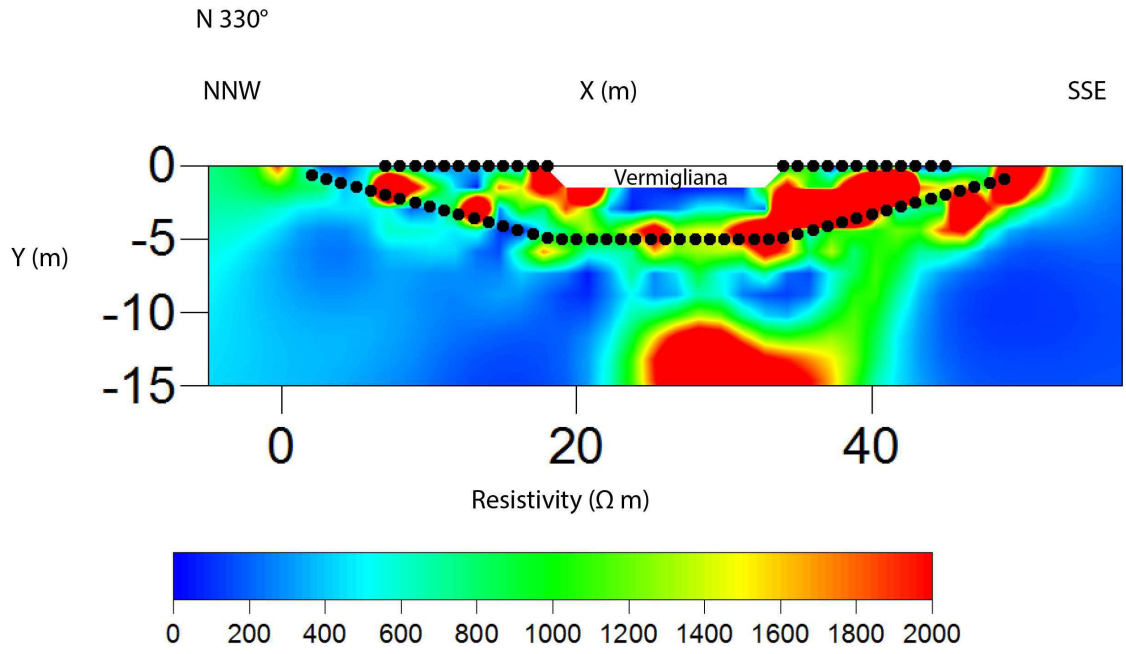

Fig. A.2: Example of resistivity cross–section resulting from the ERT survey conducted in Vermiglio on 30^{th} July 2013. The cross–section is facing downstream. A low resistivity domain is located under the Vermigliana creek, while the riparian zones show, on average, higher resistivity values. The black dots represent the electrodes position both on the levee surface (24 stainless steel electrodes) and inside the perforation drilled under the Vermigliana creek (48 brass electrodes).

A very low resistivity domain characterizes the area beneath the Vermigliana creek and extends till a depth of 4 m below ground level, with an average resistivity value of 50 Ωm. At first glance, the presence of such a domain may be justified by the seepage process, which allows the – total or partial – sub–riverbed saturation with the consequent overall resistivity modification (as expeted, according to Archie's law). If we focus on resistivity values instead, a discrepancy emerges: An average resistivity of 50 Ωm is incompatible with the values characterizing both deposits and waters of the Vermigliana creek, whose resistivity have orders of magnitude of 1000 Ωm and 100 Ωm respectively. In order to explain the features of this domain, whose existence in the HZ has also been confirmed by two auxiliary ERT surveys, we hypothesized the presence of a high clay fraction coming from the glacial moraines and transported by the creek itself, which not only increases the electrical conductivity in the sub–riverbed, but also reduces its hydraulic conductivity. On the other hand, if we focus on the areas adjacent to the river, also referred to as "riparian zones", it is possible to highlight a difference between the left and the right bank (Fig. A.2), since the former has an average electrical conductivity slightly lower than the latter.

Finally, albeit being outside our domain of interest (i.e., the area between the surface electrodes and the borehole electrodes), the resistivity cross–section in Fig. A.2 also shows the bedrock, identified by the very high resistivity domain at a depth of 10 m below ground level.

The second inversion technique is strongly related to the ERT time–lapse monitoring currently in progress in the Vermigliana site and aims at highlighting how resistivity varies over time. As already described by Perri et. al [2012], this approach is based on the following equation:

$$R = \frac{R_t}{R_0} R_{hom} \tag{A.1}$$

where R_t is the transfer resistance measured at time t, R_0 is the background (i.e., time 0) transfer resistance and R_{hom} is the transfer resistance for a homogenous resistivity distribution model; all these transfer resistance values are referred to the same quadrupole. Once R is computed for every electrodes quadrupole common to all the available datasets, the ERT data inversion with an error equal to 3% is performed, as already described above. The results consist of $T - 1$ cross-sections (with T total number of ERT acquisitions) displaying the resistivity variation over time expressed as percentage, with respect to the background survey (100% indicates no changes, higher values imply an increase in resistivity, and lower values are related to a decrease). Although the time–lapse monitoring began in July 2013, for this work we consider only the acquisitions carried out from 5^{th} May 2014 onwards, because of the nature of the observed phenomena.

In order to better analyze the outcome of this second inversion technique, it is useful to divide the domain of interest into three parts: sub–riverbed, left bank, and right bank. In the first part, between 14^{th} May 2014 and 16^{th} July 2014 an increase in resistivity variation takes place (up to 150%), followed by a rapid decrease to 100%. Such behavior may be due to a glacial water pulse, which is poor in ions and therefore characterized by a high resistivity. On the other hand, the left bank is characterized by a constant decrease in resistivity variation, from values higher than 120% to values around 60% (on average). This variation is probably related to the presence of an effluent of two small lakes upstream, whose waters are presumably more conductive. Finally, the last part shows a slight increase in resistivity variation over time (values are always, on average, higher than 100%). Therefore, the right bank has constantly a higher resistivity with respect to the background, which may be caused by a constant flux of new glacial water poor in ions.

Al already mentioned in chapter 2, together with the ERT technique we applied also the DTS methodology: Given the double–ended configuration chosen, it is necessary to lead back the temperature profile to the effective length of the borehole perforation and this has been achieved by averaging each "onward" temperature value with the correspondent "backward" value. Hence, each ultimate temperature profile has a length equal to 96 m with 97 temperature values (4 meters at each fiber–optic end have been removed since they are located outside the borehole). The four temperature profiles available so far are displayed and compared in Fig. A.3, where also the relative positions of both Vermigliana creeks and riverbanks are indicated. All these profiles show a common trend, which can be detected in each

trace and analyzed according to the partitioning in Fig. A.3:

- Part 1: These segments are characterized by the highest temperature values, since here the fiber–optic cable is rather shallow. Therefore, there is a strong influence of the superficial temperature, which is probably also combined with the effect of the waters from the effluent nearby;
- Part 2: In this portion, the trend of each T profile is fairly linear and the temperature values are relatively high. Also here, there may be an influence from the effluent of the lakes upstream;
- Part 3: These segments correspond to the sub–riverbed of the Vermigliana creek. Here the trend is more variable than the other parts and sharpens over time, given the complexity of the processes taking place (e.g., mixing between glacial water and rain water with ground water);
- Part 4: This part of the traces is relative to the right bank and is clearly characterized by the lowest temperature values, probably due to the flux of glacial water;
- This portion represents the part of the fiber–optic cable in excess that has been rolled and located at a depth of 0.5 m below ground level.

A time–lapse analysis of the profiles in Fig. A.3 highlights a temperature increase over time: In fact, from the first to the last survey, the mean temperature augments of 2.09 °C. This temperature variation is not constant along the whole fiber, since the left bank warms up a little bit more than the right bank (i.e, mean increase for the left bank = 2.67 °C vs. mean increase for the right bank = 2.12 °C): this is also confirmed by the T variation computed for each sampling point. Therefore, not only we can assume that such temperature variation over time is instrument independent, but also we can hypothesize that the left and right riverbanks behave in two different ways, or, more likely, that are subject to different phenomena (i.e., flux of lacustrine and glacial water, respectively).

Finally, what needs to be strongly highlighted is the relation existing between DTS and ERT data, well proven by the comparison of Fig. A.3 with the results of the time–lapse inversion. The relatively higher temperature values characterizing the left bank of the Vermigliana creek well fit the decrease in resistivity described before, since both this two effects may be caused by a sub–superficial flow of lacustrine water, which is hotter and richer in ions with respect to glacial water. On the contrary, a sub–superficial flux of glacial water may explain the overall lower temperature of the right bank and its relatively higher resistivity, given the lower ions contents.

Future work

The data acquired so far need to be coupled with a flow and transport model, in order to completely describe the structures and the processes characterizing the HZ of the Vermigliana creek. To achieve this future goal, we will use the CATHY (CATchment HYdrology) model combined with data assimilation methods, thanks

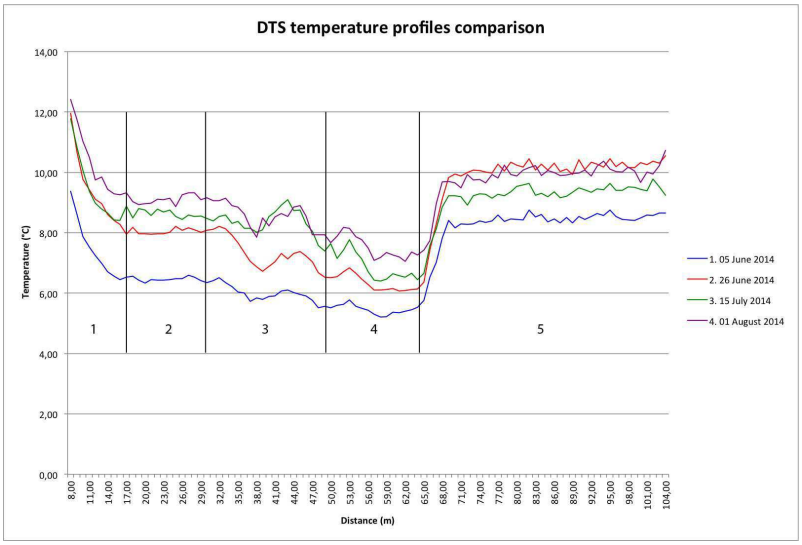

Fig. A.3: Comparison between DTS temperature profiles acquired in the Vermigliana site. In each profile five segments can be identified: 1, initial part influenced by the lakes' effluent and the surface temperature; 2, left bank of the Vermigliana creek (comparable with the left bank of the ERT cross section); 3, Vermigliana creek; 4, right bank of the Vermigliana creek (comparable with the right bank of the ERT cross section); 5, fiber–optic cable rolled at 0.5 m below ground level. All the temperature profiles show the same trend, with higher temperatures in the left bank and lower values in the right one, while the hyporheic zone below the Vermigliana creek is characterized by a variable trend that sharpens over time.

to whom it is possible to assimilate both ERT and DTS data inside the numerical model itself. Furthermore, the time–lapse monitoring of the hyporheic zone of the Vermigliana creek will continue in the next years, given the need of analyzing more in detail the applicability of these two non–invasive methodologies in such a unique domain.

Conclusions

One of the main problems in the HZ characterization is the obvious need of investigating a domain located under a riverbed. In order to overcome such a problem, we applied two non–invasive methodologies, ERT and DTS, with an innovative instrumentation deployment: Both a multicore cable and a fiber–optic cable are located into two horizontal perforations drilled below the Vermigliana creek. Thus, the instruments are inside the HZ, our domain of interest. These two methodologies not only allowed fast surveys, but also supplied several high–quality datasets, comprising both resistivity values and temperature profiles that permitted a time–lapse analysis of the investigated area. The comparison between these different data highlighted a complex domain, characterized by the interaction of waters with different origin (e.g., glacial, superficial, and groundwater). Therefore a combined application of ERT and DTS measurements can lead to a deeper characterization of the hyporheic zone, given the strong correlation existing between the physical parameters analyzed. Hence, the preliminary results presented in this work already show their high potential, which, however, will be fully expressed only through an appropriate

hydrological modeling.

References

Acworth, R. I. and G. R. Dasey, 2003. Mapping of the hyporheic zone around a tidal creek using a combination of borehole logging, borehole electrical tomography and cross-creek electrical imaging, New South Wales, Australia. *Hydrogeology Journal*, 11(3), 368–377.

Anderson, M. P., 2005. Heat as a ground water tracer. *Groundwater*, 43(6), 951–968.

Bianchin, M., L. Smith, and R. Beckie, 2010: Quantifying hyporheic exchange in a tidal river using temperature time series. *Water Resources Research*, 46(7).

Boulton, A. J., S. Findlay, P. Marmonier, E. H. Stanley, and H. M. Valett, 1998. The functional significance of the hyporheic zone in streams and rivers. *Annual Review of Ecology and Systematics*, 59–81.

Bridge, J.W., 2005. High resolution in-situ monitoring of hyporheic zone biogeochemistry. *Environmental Agency Science Report*.

Constantz, J., 1998. Interaction between stream temperature, streamflow, and groundwater exchanges in alpine streams. *Water resources research*, 34(7), 1609–1615.

Crook, N., A. Binley, R. Knight , D. A. Robinson, J. Zarnetske, and R. Haggerty, 2008. Electrical resistivity imaging of the architecture of substream sediments. *Water Resources Research*, 44(4).

Dal Piaz, G. V., A. Castellarin, A. Carton, F. Daminato, S. Martin, L. Montresor, V. Picotti, G. Prosser, E. Santuliana, and L. Cantelli, 2007. Note Illustrative della Carta Geologica d'Italia alla scala 1: 50.000, Foglio 042 Malè. Provincia Autonoma di Trento, Servizio Geologico. APAT, Servizio Geologico d'Italia, Roma.

Krause, S., D. M. Hanna, and J. H. Fleckenstein, 2009. Hyporheic hydrology: interactions at the groundwater-surface water interface. *Hydrological Processes*, 23(15), 2103–2107.

Lane, J. W., F. D. Day–Lewis , C. D. Johnson, C. B. Dawson, D. L. Nelms, C. A. Eddy–Miller, J. D. Wheeler, C. F. Harvey, and H. Karam, 2008- Fiber–optic distributed temperature sensing: a new tool for assessment and monitoring of hydrologic processes. *Symposium on the Application of Geophysics to Engineering and Environmental Problems*.

Perri, M.T., G. Cassiani, I. Gervasio, R. Deiana, and A. Binley, 2012. A saline tracer test monitored via both surface and cross–borehole electrical resistivity tomography: comparison of time-lapse results. *Journal of Applied Geophysics*, 79, 6–16.

Reidy, C. A. and S. M. Clinton, 2004. Delineation of the hyporheic zone. University of Washington Water Center.

Selker, J. S., L. Thevenaz, H. Huwald , A. Mallet, W. Luxemburg, N. Van De Giesen, M. Stejskal, J. Zeman , M. Westhoff, and M. B. Parlange, 2006. Distributed fiber–optic temperature sensing for hydrologic systems. *Water Resources Research*, 42(12).

Westhoff M. C., M. N. Gooseff, T. A. Bogaard, and H. H. G. Savenije, 2011. Quantifying hyporheic exchange at high spatial resolution using natural temperature variations along a first–order stream. *Water Resources Research*, 47(10).

A.2 Combined geophysical surveys for the characterization of a reconstructed river embankment

Engineering Geology 211 (2016) 74–84

Contents lists available at ScienceDirect

Engineering Geology

journal homepage: www.elsevier.com/locate/enggeo

Combined geophysical surveys for the characterization of a reconstructed river embankment

Laura Busato [a,*], Jacopo Boaga [a], Luca Peruzzo [b,c], Mahjoub Himi [d,e], Simonetta Cola [f], Silvia Bersan [f], Giorgio Cassiani [a]

[a] Department of Geosciences, University of Padua, Via Giovanni Gradenigo 6/A, 35131 Padua, Italy
[b] ENSEGID, University of Bordeaux Montaigne, EA4592-Bordeaux INP, 1 allée Daguin, Pessac, France
[c] GO-Energy, Geosciences Division at Lawrence Berkeley National Laboratory, Building 74, Calvin Road, Berkeley, CA, USA
[d] Department of Mineralogy, Petrology and Applied Geology, University of Barcelona, Martí i Franquès s/n, 08030 Barcelona, Spain
[e] Département de Génie Civil et Environnement, Ecole Nationale des Sciences Appliquées (ENSAH), Université Mohammed Premier, 32003, Sidi Bouafif, Morocco
[f] Department of Civil, Environmental, and Architectural Engineering, University of Padua, Via Marzolo 9, 35131 Padua, Italy

ARTICLE INFO

Article history:
Received 15 March 2016
Received in revised form 23 June 2016
Accepted 26 June 2016
Available online 28 June 2016

Keywords:
River embankment
Jet-grouting
ERT
MASW
GPR
Geophysical characterization

ABSTRACT

The managing and monitoring of natural and artificial river levees are crucial in order to reduce the hydrological risk. As these hydraulic structures are very extensive, the typically applied techniques (e.g. geotechnical soundings and visual inspections) provide only punctual information that are generally focused on areas already recognized as troublesome. To overcome these well-known issues, non-invasive and cost-effective geophysical measurements have been proposed (and used) to supply spatially extensive data that should be integrated with direct investigations. Therefore, in this paper we present the joint use of multichannel analysis of surface waves (MASW), electrical resistivity tomography (ERT), and ground penetrating radar (GPR) to characterize a reconstructed river embankment (made of concrete and tout-venant) prone to serious leakages. We compare common lengthwise ERT profiles, performed from the levee crest, with cross-embankment and cross-river profiles, showing how relying only on the first type of surveys may lead to misinterpretations. Furthermore, we take advantage of a land-streamer for the MASW surveys and of a trans-illumination approach to improve the GPR application. The comparison between geophysical and geotechnical data helps identify the spatial extent of the volume actually invaded by grouting injections, which appears as a highly electrically conductive mean. The lack of homogeneity within this domain, highlighted by the cross-embankment ERT profiles, can be related to the seepage phenomena affecting this artificial levee. Therefore, this case study demonstrates the effectiveness of combining direct and non-invasive investigations for the characterization of river embankments.

1. Introduction

Frequency and magnitude of extreme flood events in Southern Europe, and in Italy in particular, have been rapidly increasing as a consequence of the combination of several factors, such as climatic changes and reduced maintenance of hydraulic structures. As river embankments provide a fundamental defence against these extreme phenomena, their characterization and maintenance play a pivotal role in hydrological risk reduction. Usually, embankment monitoring takes place mainly through visual inspections, boreholes, and point geotechnical measurements; this cannot provide an exhaustive characterization over large structures. If system's heterogeneities are not properly identified, this may lead to a serious underestimation of the relevant hydraulic risk, as the overall levee's resistance depends, practically, on the absence of localized weak points.

In this paper we focus on the specific problem of characterizing river embankments reconstructed, often under the pressure of emergency, following a collapse. These emergency interventions usually consist in building provisional artificial structures that typically require further reinforcement works. This results in the overlapping of several structures whose geometrical, mechanical and hydraulic properties are, in the end, poorly known.

This is the case of our studied site, located in North-Eastern Italy, where an embankment was reconstructed in 2010 following a collapse caused by a large rainfall event. In this case the embankment reconstruction, in terms of structural and river containment functions, included the placement of a grout wall designed to be, as much as possible, a waterproof cutoff wall (Sharma and Reddy, 2004).

* Corresponding author.

http://dx.doi.org/10.1016/j.enggeo.2016.06.023
0013-7952/

The effective maturation of the concrete, and the continuity of the overlapping grout columns cannot be fully ascertained with localized probing. Thus geophysical prospection methods can provide an effective and cheap alternative, whose application overcomes several limitations of typical monitoring techniques (e.g., piezometers and geotechnical sounding). The use of electrical resistivity tomography is nowadays state of the art in levee and dam characterization (Cho and Yeom, 2007; Sjödahl et al., 2009), together with seismic methods (Ivanov et al., 2005; Karl et al., 2011; Lane et al., 2008), and ground penetrating radar (Di Prinzio et al., 2010). However, it is increasingly apparent how only a smart integration of different geophysical methodologies can lead to sharp progresses (see e.g. Cardarelli et al., 2014; Inazaki and Sakamoto, 2005;). These non-invasive techniques, in addition, definitely need the validation provided by more traditional, pointwise, geotechnical investigations (e.g. Perri et al., 2014). Non-invasive techniques have also been successfully used to image concrete structures, where cement appears generally more electrically conductive than the surrounding materials (Karastathis et al., 2002; Karhunen et al., 2010; Turk and Dearman, 1987).

In this work we combine three different non-invasive geophysical methods in order to characterize a reconstructed river embankment, with the specific aim of imaging the continuity of a grout wall. Therefore all considerations above are highly relevant here, and the case study is an excellent testing ground to assess pros and cons of each approach and of their combination, with additional insight into the possible interpretation pitfalls.

2. Study site

The study site is located in the municipality of Megliadino San Fidenzio, in the province of Padova, north-eastern Italy. Here a 100-meter reach of the Frassine River embankment collapsed in 2010, after a very large rainfall event, in the Prà di Botte area (Lat. 45°15′ 18.3″ N, Long. 11°32′35.8″ E, Fig. 1).

From a geological viewpoint, the site lies in the Adige Alluvial Plain, a part of the Veneto-Friuli Plain, and therefore is characterized by Tertiary to Quaternary sediments. The entire domain has been strongly influenced by the Last Glacial Maximum (LGM, 30,000–17,000 years B.P.) and the following post-LGM phase, which has led to the formation of paleosols (e.g., caranto paleosol) and fluvial terraces (Fontana et al., 2008). More in detail, the field site area consists of ancient fluvial ridges now evolved into silty-clayey soils with a low sand content (ARPAV, 2013).

The Frassine River is one of the six segments into which the Guà River is divided. It flows from Borgo Frassine (Montagnana, PD) to Brancaglia (Este, PD), with a length of 13.42 km, and is part of the larger Brenta-Bacchiglione catchment. From a hydrological point of view, this river has a mixed regime that implies high flow rates during spring and autumn and low flow rates on the other seasons (Bondesan, 2001).

The flood event that caused the levee rupture took place in the early afternoon of November 1st 2010 (Fig. 1), when the water level of the Frassine River reached its ever-recorder historical peak (4.54 m). This happened after a three-day precipitation event that resulted in a cumulative rainfall amount of 300 mm (ARPAV, 2010). As a consequence, the right embankment collapsed for a total length of about 100 m.

The emergency phase began with the building of a preliminary barrier made of boulders with different diameters. Given the need of reducing the water flow, this first structure has then been reinforced with concrete and sheet piles, which also helped in increasing the overall stability. Then, three days after the flood event, the whole preliminary structure was covered with aggregates (tout-venant), thus ending the first phase of the embankment restoration.

In order to provide a longer-term solution, new reinforcement works from the embankment crest took place in 2012 (second phase). They can be divided into three activities: (i) concrete injection along the whole preliminary structure (110.0 m length, 9.5 m depth), (ii) jet-grouting diaphragm construction, extended also to the undamaged levee (170.0 m total length, 22.0 m total depth), and (iii) "Tube a Manchette" grouting to further waterproof the whole structure. These interventions created a grout wall in the central part of the reconstructed embankment.

Despite these actions to improve the embankment's hydraulic performance, water infiltration occurred during the following months, thus showing that the new structure needed further investigations and interventions. More in detail, a diffuse seepage in the embankment toe was observed upstream, while water infiltration in the lower part of the outer face characterized the downstream sector. Therefore, nine geotechnical soundings were carried out in 2013, six of which were drilled in the reconstructed part, showing a rather heterogeneous system, where the different reinforcing interventions overlap. Since these soundings provide only punctual information, a characterization of the system's heterogeneous structure was not possible with these means.

The remaining three soundings were drilled in the original earthen levee, which is homogeneously composed of silty-clayey sand, as expected. These soundings also show a clayey layer between 11 m and 13 m depth below the levees' crest.

In a third phase, some interventions were put in place to try and limit the observed seepage (year 2014). In particular, a stability bank was built on the outer side of the embankment, with a 0.5 m thick gravel drainage mattress and a seepage berm and a collector ditch to avoid

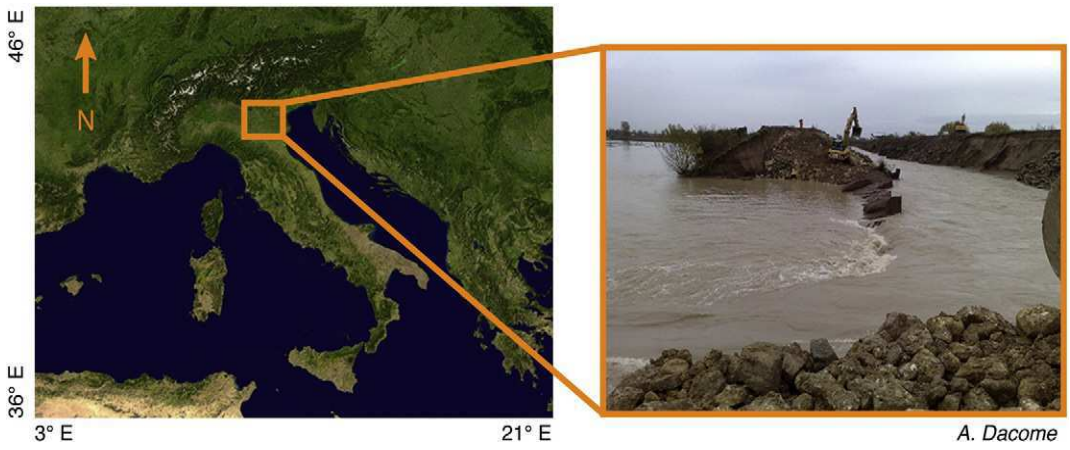

Fig. 1. Location and collapse of the right embankment of the Frassine River. The field site is located in north-eastern Italy (Lat. 45°15′18.3″ N, Long. 11°32′35.8″ E) and consists of the reconstructed embankment of the Frassine River. The collapse occurred on November 1st 2010 as a consequence of an extreme flood event.
(Courtesy of A. Dacome).

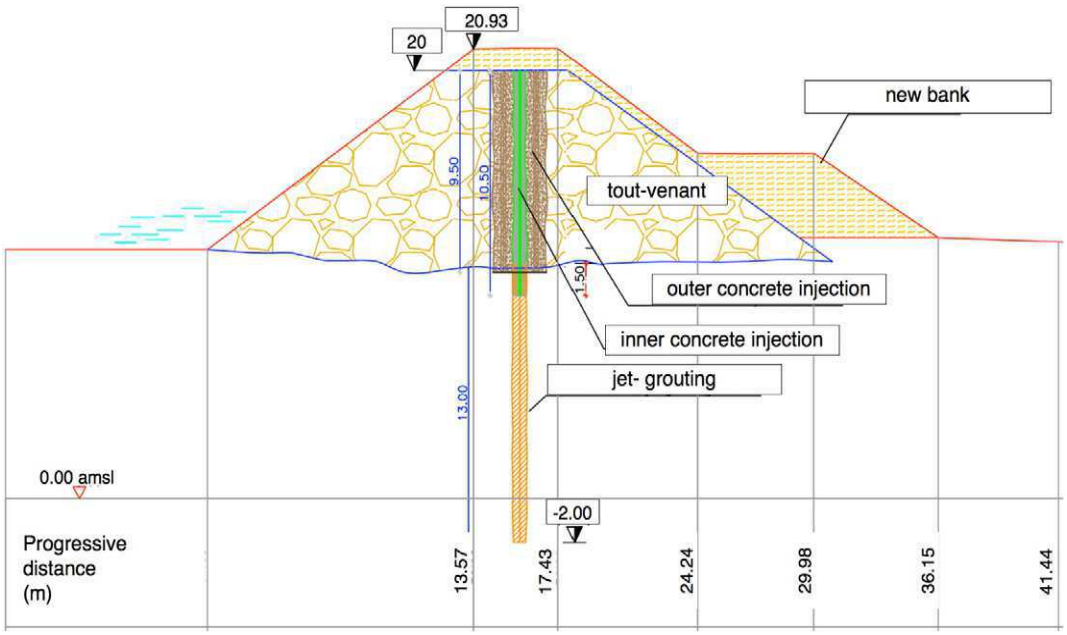

Fig. 2. Technical section of the reconstructed embankment as resulting after three reconstruction phases (2010–2014). The scheme is facing downstream with the river on the left side of the section (blue dashes). The labels describe the material forming each part of the levee (i.e. tout-venant in the outer part and concrete injection in the core of the levee). All values are expressed in metres.

water stagnation. A section of the resulting geometry is shown in Fig. 2, where also the arrangement of the different materials is indicated (i.e. grout wall in the central part and tout-venant in the outer zone). The embankment total height from ground level is 8.7 m, with a crown 4 m wide, and both inner and upper-outer faces have a ratio of width to height of 3:2. The stability bank ("new bank" in Fig. 2) is 5 m high from ground level, has a ratio of width to height of 2:1 and a crown 4 m wide.

In spite of the efforts expended to try and secure the embankment hydraulic containment, as of today still some seepage shows up during high water levels. This also raises concern about the embankment stability. Therefore, a suitable extensive and high-resolution characterization of the structure is mandatory.

The goal of this paper is to present and thoroughly discuss the results of this characterization, conducted with a combination of non-invasive and traditional geotechnical methods. We used multichannel analysis of surface waves (MASW) in an innovative land-streamer mode, electrical resistivity tomography (ERT), and ground penetrating radar (GPR). These results were compared against and validated with the support of geotechnical information from boreholes, showing the tremendous potential of this data integration approach.

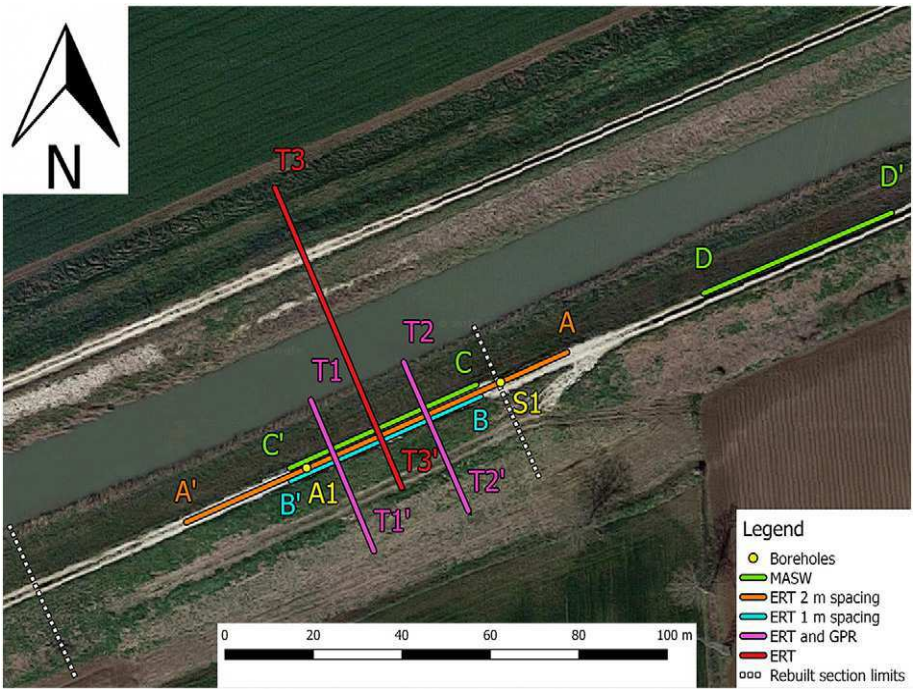

Fig. 3. Map of all geophysical measurements conducted on the Frassine River site. The surveys comprise: lengthwise ERT profile with 2 m electrode spacing (A'A), lengthwise ERT profile with 1 m electrode spacing (B'B), cross-embankment profiles (T1'T1) and (T2'T2), cross-river profile (T3'T3), MASW on the natural (D'D) and on the artificial (C'C) levee, GPR with *trans*-illumination approach (T1'T1) and (T2'T2), and boreholes (*A*1 and *S*1).

3. Geophysical measurements

The location of each geophysical survey is shown in Fig. 3. Each technique provides different and complementary pieces of information concerning the investigated domain (in terms of electrical resistivity, shear wave velocity and dielectric permittivity). Moreover, the acquisition geometries are different, in order to extract the relevant information content.

The seismic surveys consisted of two surface wave profiles analysed using multichannel analysis of surface waves (MASW) (Foti, 2005; Foti et al., 2015; Park et al., 1999; Socco and Strobbia, 2004).

Here we only performed two classical MASW acquisitions, namely:

- one MASW survey within the reconstructed levee (C'C in Fig. 3);
- one MASW survey outside the reconstructed levee (D'D in Fig. 3).

These two MASW surveys were located in order to compare the reconstructed sector to an adjacent natural portion, given the difference in terms of mechanical properties that should arise as a consequence of the different materials involved.

In order to perform these measurements, we took advantage of a seismic streamer, a specific tool composed of several geophones linked together by means of fabric straps. More in detail, the streamer consisted of 24 4.5 Hz vertical geophones, each one screwed on a heavy metallic plate. These plates not only allowed a good coupling with the ground surface but also permitted an easier repositioning of the instrumentation along the embankment crest. In fact, one of the main advantages of the seismic streamer is that an AVT vehicle, which usually hosts the seismograph and the laptop controller, can easily drag it. When the area of interest is reached, the vehicle is stopped and the measurement takes place. Therefore, this setup allowed a quick acquisition process that is ideal for larger scale mapping, particularly on one dimensional structures such as levees.

In our field site, both lines used 24 channels with 2 m spacing between geophones, for a total length of 46 m. The source offset was equal to 6 m and a sledgehammer (5 kg) was used as seismic source. For each MASW survey we used a Geometrics Geode seismograph with 24 bit resolution, sampling rate equal to 0.25 ms, and total acquisition time equal to 2 s.

Electrical resistivity tomography (ERT) can provide meaningful, high-resolution images of the system's electrical conductivity (Binley and Kemna, 2005). In the context of embankment investigation this results in very detailed information concerning the system's structure (e.g. Niederleithinger et al., 2012; Perri et al., 2014; Weller et al., 2006), particularly as fine-grained sediments are generally more electrically conductive than coarse materials, and fine-grained sediments (clay and silt) represent the core of well-built embankments. ERT is also very flexible in terms of scaling and resolution, so it is particularly suitable for this type of investigation. On the other hand, ERT may not be appropriate when large-scale fast mapping is requested. In this case, electromagnetic methods are to be preferred (see e.g. Cassiani et al., 2012).

Electrical resistivity tomography (ERT) was applied at this site with different configurations, in order to vary depth of investigation, resolution, and explore longitudinal and transverse sections of the reconstructed embankment. The ERT surveys consisted of:

- Lengthwise profiles: 48 stainless-steel electrodes placed along the levee crest, in correspondence to the reconstructed part. We used electrode spacing values of 1 m and 2 m, so as to vary total length (47 m and 96 m, respectively) and consequently spatial resolution and depth of investigation (the latter being about 10 m and 20 m, respectively). All these surveys share the position of the 23rd electrode, which was fixed to guarantee the overlapping of the profiles. Furthermore, we employed both Wenner-Schlumberger and dipole–dipole skip-zero acquisition schemes, the latter being characterized by a distance between electrodes forming each dipole equal to the electrode spacing (for a discussion, see Binley and Kemna, 2005).
- Cross-embankment profiles: we collected two transverse lines (one upstream and one downstream, labelled T1'T1 and T2'T2 respectively in Fig. 3), with 48 stainless-steel electrodes spaced 0.75 m. In both cases the acquisition scheme was a dipole–dipole skip-zero. These profiles covered the outline of the embankment (from the seepage berm to the water level, via the embankment crest). The locations of these profiles were selected according to the results of the lengthwise surveys;
- Cross-river profile: we used 72 stainless-steel electrodes (and a waterproof cable) spaced 1 m along a line covering the outline of the reconstructed embankment, the riverbed, and the profile of the opposite bank. Again, we employed both Wenner-Schlumberger and dipole–dipole skip-zero acquisition schemes.

Each ERT acquisition was made with an IRIS Instruments Syscal Pro resistivity metre, measuring both direct and reciprocal resistance values (Daily et al., 2004), necessary to assess the measurement error. For ERT inversion we used the open software provided by A. Binley (Profiler and R2, Lancaster University, UK). As for the data inversion an exact knowledge of the topography is required (Henning et al., 2005), we created the inversion domain (i.e. the mesh) for the cross-embankment profiles on the basis of the technical section represented in Fig. 2. Therefore, we considered the height and distances therein (for a more detailed description, see Section 2). For the lengthwise profiles we assumed a flat surface, given that the slope is negligible. The error threshold for the resistance measurements and the error for the inversions were consistently fixed at 5%.

We also used Ground-penetrating Radar (GPR) for further investigations. Note that GPR (Annan, 2005) has been often proposed as a fast diagnostic method for embankment characterization in zero-offset mode (e.g. Di Prinzio et al., 2010; Niederleithinger et al., 2012; Szynkiewicz, 2000). However, in many cases the use of GPR in reflection mode from the top of the embankment may prove disappointing. In particular, if the structure of the embankment is, as it should be, made mostly of fine materials (silt and clay), the corresponding high electrical conductivity will prevent an effective propagation of the electromagnetic wave associated with GPR. This high attenuation will kill the signal and produce practically no reflections or diffractions from the body of the embankment. Thus the identification of cavities created, for example, by animals, does not seem reliable using GPR in the classical surface configuration.

In this framework we tried a different use of GPR, in the attempt of measuring the average volumetric moisture content of the embankment at selected locations. The adopted geometry is a simple trans-illumination approach across the embankment structure (Fig. 9c), somehow similar to a classical zero-offset profile adopted in cross-hole GPR (e.g. Deiana et al., 2008). Knowing the geometry it is thus possible to obtain an estimate of the soil moisture content across the embankment. We collected GPR data in correspondence of the cross-embankment ERT lines (T1'T1 and T2'T2 in Fig. 3), to produce two radargrams: one upstream and one downstream. We used a PulseEKKO system with 100 MHz antennas.

All information about location, date and profiling mode for the different surveys are summarized in Table 1.

4. Geophysical surveys results

4.1. Multichannel analysis of surface waves

The MASW survey was planned also as a test of the seismic streamer system in order to assess the homogeneity of long structure as river embankment. The aim was the quick detection of the reconstructed part of the levee via the simple phase velocity-frequency (p-f) spectrum

Table 1
Summary of the geophysical measurements at the Frassine field site. The multichannel analysis of surface waves (MASW) measurements (meas.) took place with 24 geophones (geoph.) spaced (sp.) 2 m. Electrical resistivity tomography (ERT), with both dipole–dipole skip-zero (dip-dip) and Wenner-Schlumberger (W-S) acquisition schemes, was carried out with an electrode (elec.) spacing varying from 0.75 m to 2 m. Finally, ground penetrating radar (GPR) was applied with a *trans*-illumination configuration.

Date	Methodology	Set-up and array
October 9th, 2014	ERT	Longitudinal profile, 48 elec., 1 m sp., dip-dip
		Longitudinal profile, 48 elec., 1 m sp., W-S
		Longitudinal profile, 48 elec., 2 m sp., dip-dip
		Longitudinal profile, 48 elec., 2 m sp., W-S
November 21st, 2014	ERT	Longitudinal profile, 48 elec., 1 m sp., dip-dip
		Longitudinal profile, 48 elec., 1 m sp., W-S
		Longitudinal profile, 48 elec., 2 m sp., dip-dip
		Longitudinal profile, 48 elec., 2 m sp., W-S
	MASW	19 meas. on the reconstructed sector, 6 on the natural levee: 24 geoph., 2 m sp.
February 2nd, 2015	ERT	Longitudinal profile, 48 elec., 2 m sp., dip-dip
February 20th, 2015	ERT	T1: Cross-embankment profile, 48 elec., 0.75 m sp., dip-dip
		T2: Cross-embankment profile, 48 elec., 0.75 m sp., dip-dip
	GPR	G1: Cross-embankment, trans-illumination configuration
		G2: Cross-embankment, trans-illumination configuration
April 9th, 2015	ERT	Cross-river profile, 72 elec., 1 m sp., dip-dip
		Cross-river profile, 72 elec., 1 m sp., W-S

characteristics of the surface wave data. It is expected that the presence of the grout wall dramatically changes the mechanical characteristics of the structure and thus of the propagating surface waves (SW). In fact, the reconstructed embankment of the studied area presents a significant difference in terms of modal distribution, with respect to the natural levee. This difference is quickly detectable by the simple observation of the spectrum computable directly on site after the seismograms recording.

More in detail, the phase velocity of the Rayleigh wave of the undisturbed portion of the embankment is characterized by rather low values slightly decreasing with increasing frequency (from 260 m/s down to 120 m/s). These are likely related to the presence of clayey and silty sand, which is in agreement with both the ERT results (see Section 4.2) and the geotechnical soundings (see boreholes projections in Figs. 4 and 5 showing alternation of cemented layers and silty sand layers). The fundamental mode of Rayleigh wave propagation is clearly identifiable and, due to the homogeneous composition of the original levee, presents little to no dispersion in frequency below the frequency of 7 Hz (Fig. 8a). On the contrary, the frequency-phase velocity spectrum recorded above the reconstructed section displays large energy dispersion with the presence of energy on several higher modes. This can be attributed to the propagation of surface waves being influenced by the heterogeneities within this part. The distribution of higher modes energy is often a consequence of the presence of strong impedance contrasts in the shallow subsurface (see e.g. Boaga et al., 2014). Moreover, the stiffening due to the grout wall is exhibited by the high Rayleigh phase velocities, close to 1000 m/s (especially for frequencies >20 Hz, Fig. 8b).

4.2. Electrical resistivity tomography

The lengthwise resistivity profiles (Fig. 4) show clearly the presence of a heterogeneous resistive body in the reconstructed part of the river embankment.

This resistive body has relatively higher resistivity values (150–600 Ω m) to a maximum depth equal to roughly 8 m from the embankment crest, while the natural levee is characterized by much lower resistivity values (50–100 Ω m) consistent with the presence of fine-grained material. It must be underlined that the measurements were conducted during low water river level; in such condition piezometer revealed an average water table at 13 m depth from the levee surface (Dacome and Bersan, 2014).

It is apparent that a quick interpretation of these results clearly confirms that the reconstructed part of the levee is very easy to identify on the basis of electrical resistivity only. However, attributing this high resistivity to the right cause may be less trivial. Considering the designed cross-sections and knowing the presence of the grout wall, one may be tempted to associate the higher resistivity values to the concrete injection, thus using ERT as a diagnostic of the extent and continuity of otherwise difficult to monitor grout injections. This simplified approach would prove, however, incorrect.

The resistivity section with 1 m electrode spacing helped us distinguish two subdomains within the reconstructed part, since it showed some heterogeneity in the resistivity structure. To better understand the reasons of these differences, we carried out two cross-embankment surveys. The location of these two cross-sections was decided on the basis of the lengthwise profiles (Fig. 4): T1, upstream, is in a region where the lengthwise profile has an average resistivity equal to roughly 500 Ω m; T2, downstream, has an average resistivity of 300 Ω m.

Both sections T1 and T2 show the presence of high resistivity regions in correspondence to the presence of coarse-grained material used in the quick reconstruction (tout-venant – see Fig. 2), and both show a more conductive inner core that corresponds to the grout injection

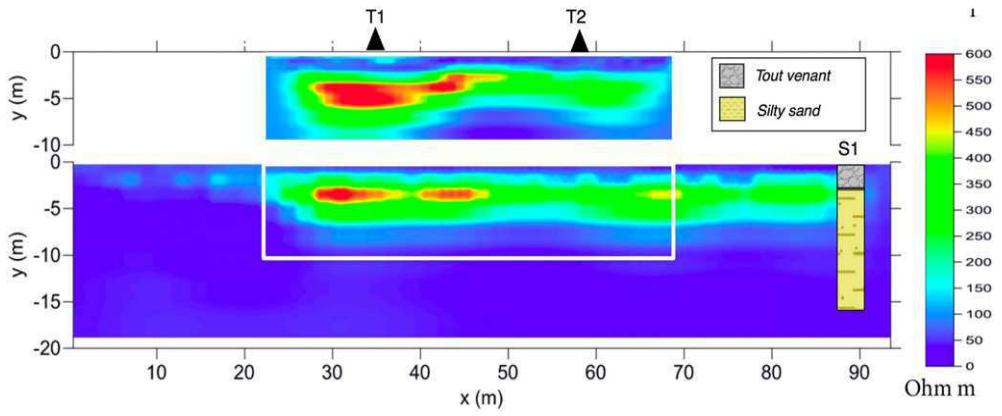

Fig. 4. ERT inversion results of the longitudinal profiles performed (mostly) on the reconstructed embankment. We used a dipole–dipole skip-zero acquisition scheme with both 1 m electrode spacing (top, B'B in Fig. 3) and 2 m electrode spacing (bottom, A'A in Fig. 3). These figures are characterized by a resistive body (150–600 Ω m) on the reconstructed part, while the natural levee has lower average resistivity (50–100 Ω m). T1 and T2 indicate the positions of the cross-sections shown in Fig. 5. *S*1 indicates the projection of the geotechnical borehole (see Fig. 3).

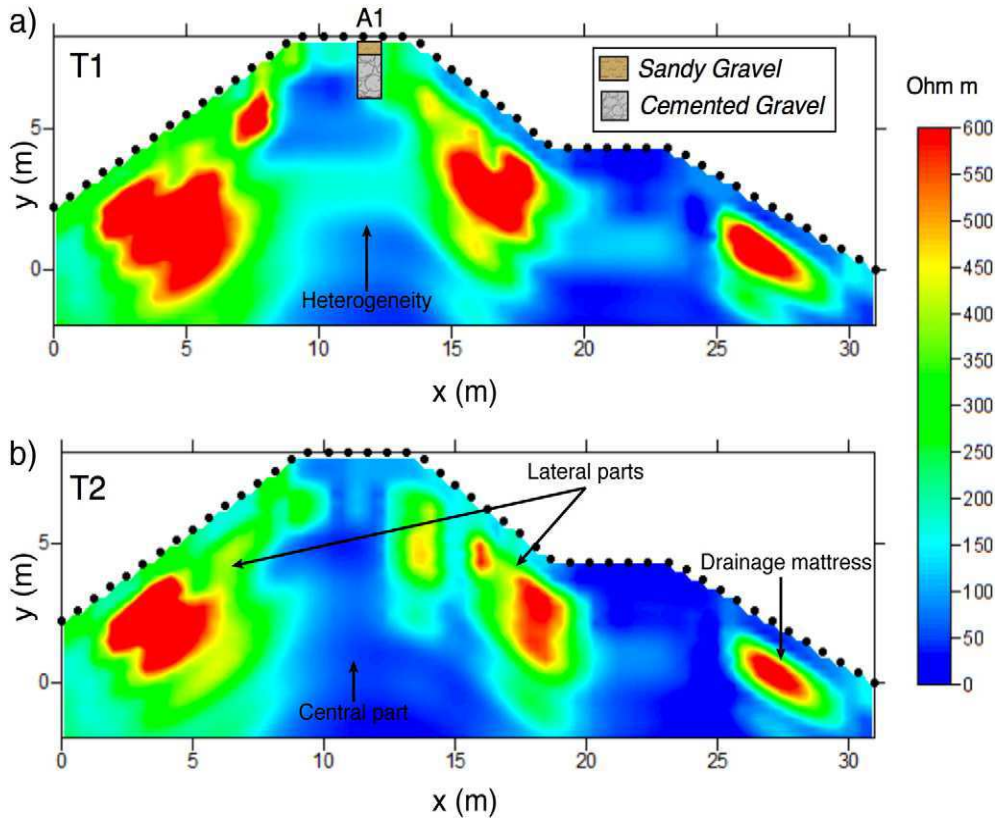

Fig. 5. ERT inversion results of the cross-embankment profiles (a) T1 and (b) T2 performed on the reconstructed embankment. In both cases we used a dipole–dipole skip-zero acquisition scheme, with 0.75 m electrode spacing. We can identify two subdomains: (i) lateral parts, with higher average resistivity due to the ballasts covering and (ii) central part, with lower average resistivity related to the concrete septum (affected by heterogeneity in the middle part in T1). The high resistivity domain between 25 m and 30 m locates the drainage mattress in both cases. The black points represent the electrode positions, while *A*1 indicates the projection of the geotechnical borehole (see Fig. 3). The cross-sections are facing downstream, with the river on the left side of the sections (not represented). For a better understanding of the geometry, see Fig. 2.

(Fig. 2). The simple comparison between Figs. 2 and 5 (i.e. the technical section and cross-embankment profiles) well explains the correspondence between the different materials and their electrical response. Note that, however, these cross-sections are not long enough to image the deeper part of the reconstructed levee, i.e. the region where jet-grouting was performed (Fig. 2).

More in detail, each cross-section can be divided into two subdomains:

- Lateral parts: both sides of the embankment have higher resistivity values because of the cited ballasts covering the outer faces. Moreover, these cross-sections well identify the drainage mattress within the stability bank.
- Central part: in both cases, this subdomain has lower average resistivity values (<150 Ω m), due to the presence of the grout wall. This is consistent with evidence from other sites (see Section 4.3 below). Furthermore, T1 shows higher resistivity in the inner core, with what appears also to be a horizontal stretch of resistivity larger than 150 Ω m, crossing the structure. This may indicate a discontinuity in the grout injection that is not apparent in section T2. This discontinuity may be related to the seepage observed in correspondence to the upstream portion of the embankment, where T1 is located.

In order to obtain information regarding the foundations of the embankment, we extended the length of the survey line to increase the

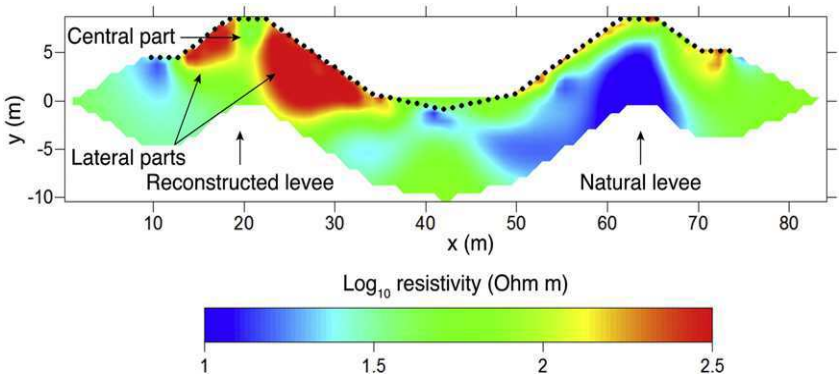

Fig. 6. ERT inversion result of the cross-river profile. This cross-section is obtained from the joint inversion of two datasets: Wenner-Schlumberger and dipole–dipole skip-zero, both with 1 m electrode spacing. This figure well highlights the differences between the reconstructed embankment (on the left) and the earthen one (on the right). The former shares the same features described for T1 and T2 (Fig. 5), while the latter has a more conductive core (likely to be clayey sand), covered with a thin layer of more resistive gravel. Unfortunately, this cross-section does not provide information regarding the reconstructed embankment foundations. The section is facing upstream and the black points represent the electrode positions.

investigation depth. Hence, we created a longer cross-river profile were both Wenner-Schlumberger and dipole–dipole skip-zero acquisition schemes were used. In the inversion procedure we considered these two datasets together, achieving both good signal to noise ratio (S/N) (from the W-S) and good resolution (from the dipole–dipole). The result, shown in Fig. 6, well represents the difference between the reconstructed embankment (on the left) and the natural one (on the right – the section is presented with a view towards upstream). The left side has the same features described for the shorter sections in Fig. 5, even though here we have a lower resolution. On the contrary, the right side is marked by a more conductive and homogeneous core (likely to be clayey sand) covered with a thin layer of more resistive gravel. The longer profile reaches a larger investigation depth, thus extending the information provided. However, no clear signal identifying the jet-grouting (Fig. 2) can be seen on the left side of Fig. 6: below the reconstructed part probably both grout and natural soil are fairly conductive, and their contrast cannot be imaged, if present.

In summary, the key finding of these ERT surveys is that the grout wall is actually an electrically conductive mean, especially if compared to the tout-venant where the grout is injected (Fig. 2). Therefore, possible discontinuities within this structure can be seen as less electrically conductive features.

4.3. Resistivity of concrete structures

The use of electrical measurements for the characterization of concrete deterioration was adopted since the first pioneering works (Hammond and Robson, 1955; Shimizu, 1928;) becoming a laboratory state-of-the-art praxis (Daily et al., 1994; Whittington et al., 1981) and a more recent field practice (Feliu et al., 1996; Polder et al., 2000; Sjödahl et al., 2009). Electrical tomography has been used to detect concrete inclusions and to detect the thickness of concrete covers (Karhunen et al., 2010; Oh, 2012). This topic is often tackled in structural engineering, also in terms of relationship between soil and concrete structures, but not so commonly faced by applied geophysicists. In general, concrete presents low resistivity values that can be easily misinterpreted in the subsoil (see e.g. Neville, 2011). As the use of jet-grouting, grout injections and grout pillars is largely diffused in geotechnical interventions, their appearance in terms of their electrical resistivity values is particularly of interest for non-invasive monitoring of these interventions.

In order to corroborate the results we obtained on the Frassine River, it is useful to report here the results of a controlled experiment of cross-hole ERT specifically designed to monitor the results of a jet-grouting experiment near the mouth of the Llobregat River near the Barcelona airport, Spain. Fig. 7a shows the configuration used for this monitoring: the instrumented boreholes are 5 m apart, while the grout injection took place in the middle. A dipole–dipole electrode array was selected for data acquisition. As it can be clearly observed in Fig. 7b, the concrete core presents very low resistivity values, and it is clearly visible (with resistivity an order of magnitude different) even though the surrounding soil is also very conductive.

Komine (1997) stated that electrical resistivity of soil–cement mortar consists of three components: (a) electrical resistivity of soil matrix; (b) electrical resistivity of pore water and (c) electrical resistivity of cement itself. Komine (1997) identified that electrical resistivity of pore

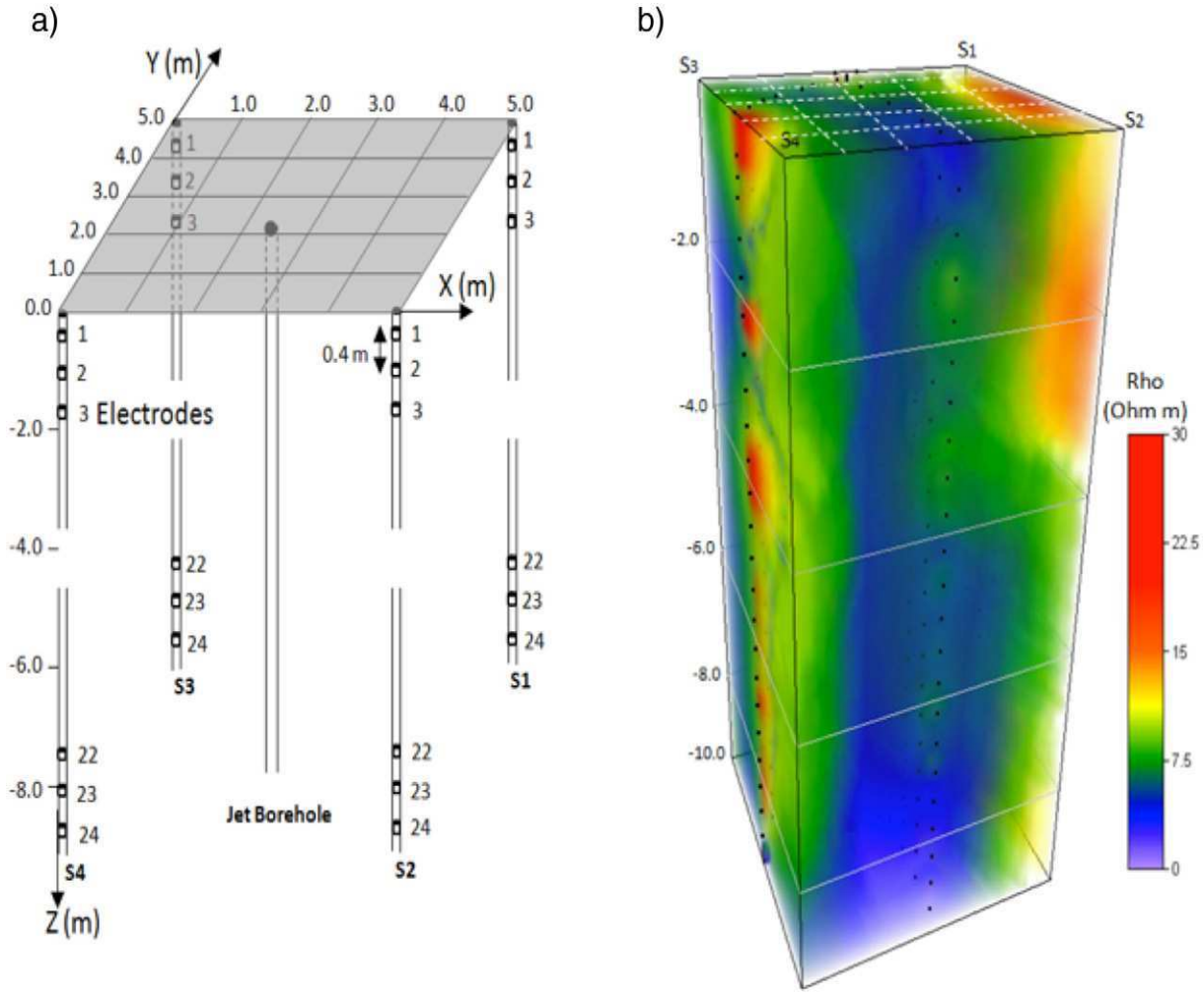

Fig. 7. (a) Electrode and borehole relative positions and (b) resistivity distribution of the three-dimensional ERT cross-hole monitoring of a jet-grouting experiment (Barcelona airport). The concrete core is well visible within the conductive soil, even if the difference in terms of resistivity is of only an order of magnitude. We used a dipole–dipole acquisition scheme.

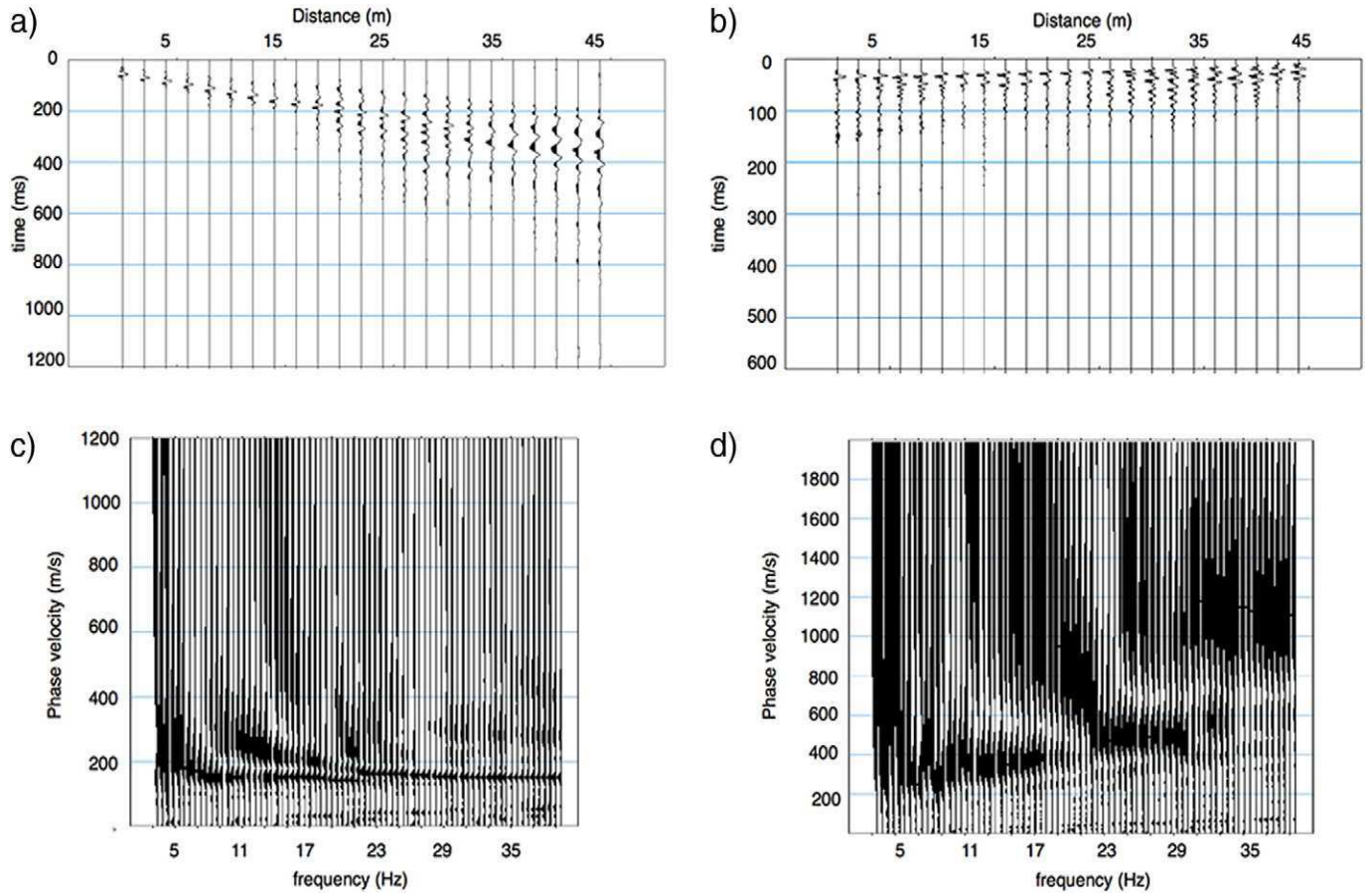

Fig. 8. Examples of seismograms recorded (a) on the natural levee and (b) on the reconstructed levee. Dispersion images (p-f spectrum) (c) for the natural levee and (d) for the reconstructed levee.

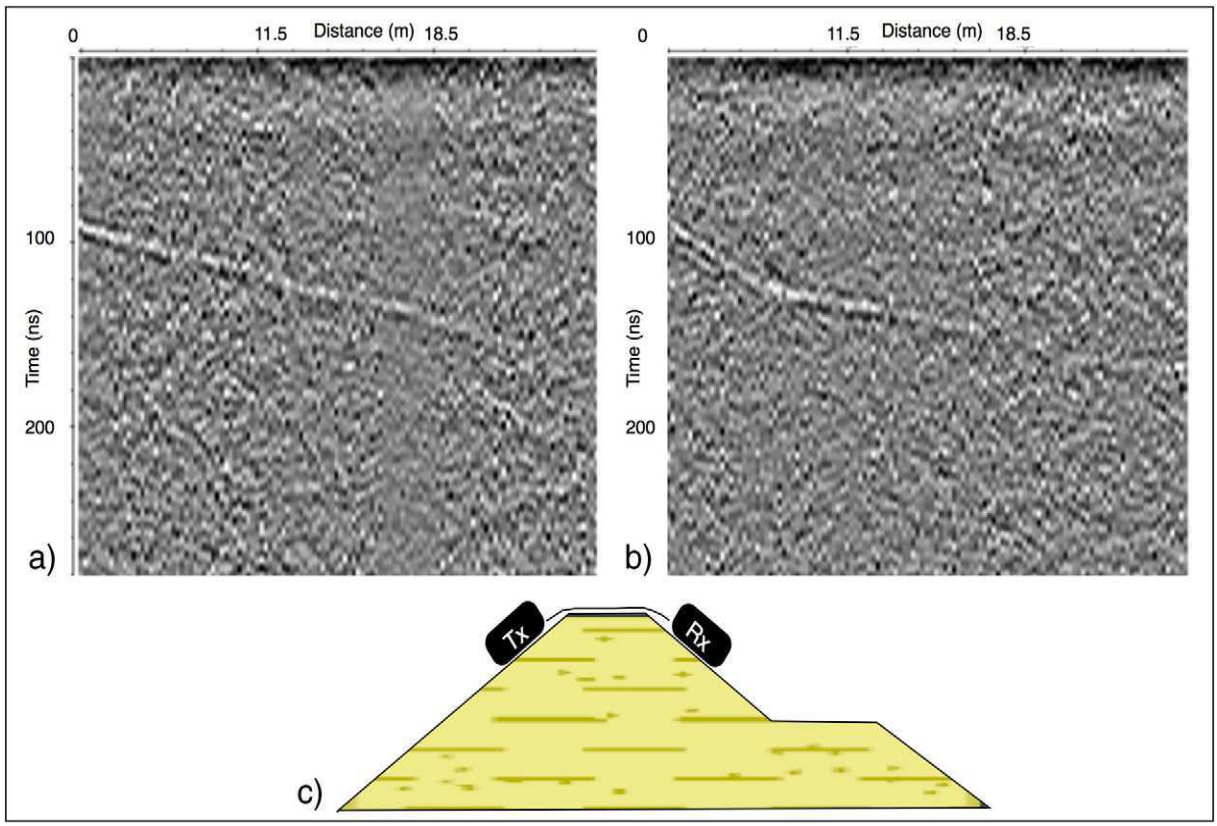

Fig. 9. Radargrams of GPR lines (a) T1 and (b) T2 and (c) schematic representation of the trans-illumination approach used across the embankment structure (the section is facing downstream, with the river on the left side – here not represented. For a better understanding of the geometry, see Fig. 2).

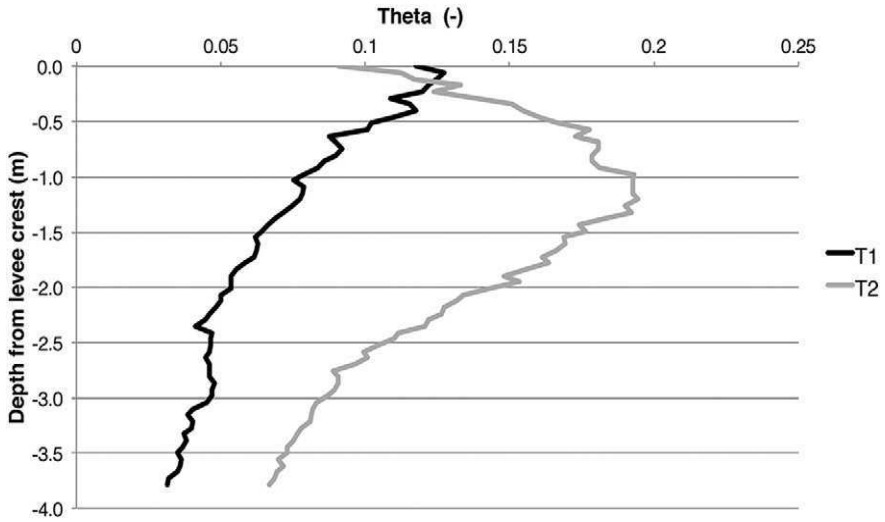

Fig. 10. Variation of average volumetric moisture content with depth from levee crest of the transverse GPR lines T1 and T2 (see Figs. 3 and 9). T2 shows higher moisture content with respect to T1, thus agreeing with the higher electrical conductivity characterizing the corresponding ERT cross-embankment profile T2 (Fig. 5b.)

water has the most significant effect because of its high electrical conductivity. The electrical resistivity increases when the degree of saturation decreases. The phenomenon behind this observation is that as saturation decreases with concrete maturation, fewer pore spaces are filled with water, which increases the electrical resistivity. Even though the evidence we present here is somewhat limited, we think that in most cases a reasonable working hypothesis is that concrete structures, especially early in their maturation stage, are to be seen as electrically conductive features with respect to their surrounding environment.

4.4. Ground penetrating radar

Two zero-offset GPR trans-illumination profiles were collected in correspondence of the transverse ERT lines T1'T1 and T2'T2. The collected radargrams are shown in Fig. 9a and b respectively. After the computation of the observed velocities from first arrival picking, and considering the complex system's geometry, we applied the empirical relation proposed by Topp et al. (1980) for the estimation of average volumetric moisture content. The corresponding profiles are shown in Fig. 10. The two profiles are very different, with a higher water content observed in section T2, i.e. in correspondence of the higher electrical conductivity in the ERT images.

It is important to underline that the water content distribution within the artificial part is likely to be very irregular, with higher values likely to be maintained by the grout wall itself. Therefore, the GPR results are consistent with the overall picture already established by ERT data. Moreover, the signal to noise ratio is lower in section T2 with respect to section T1, thus agreeing, at least from a qualitative point of view, with more electrically conductive materials, i.e. with a higher signal attenuation. It must be noted that GPR data on the Frassine River site present relatively low S/N, as expected given the general presence of fine-grained sediments.

5. Discussion and conclusions

The use of different geophysical techniques for the characterization of a reconstructed embankment has led us to a few meaningful results:

i) The use of multiple methodologies clearly improves river embankment characterization, in terms of both mechanical and hydraulic characteristics. In particular, we observed that the use of ERT only may lead to difficulties in the interpretation, as the electrical resistivity of material may vary case by case. On the other hand, GPR suffers from severe attenuation due to the presence of fine-grained sediments, typical of levees.

ii) Seismic methods are scarcely used in river embankment characterization, due to relatively complex logistics during acquisition that may limit their application for longer and more detailed surveys. The use of land-streamers can efficiently overcome this problem, allowing a quick analysis of surface waves on elongated structures like levees. In fact, surface waves are easy to generate and to analyse, even with receivers that are not firmly planted. In the case of reconstructed grout walled embankments, the simple and quick observation of dispersion spectra can be considered a good preliminary diagnostics of the mechanical changes in the structure. Once long distances are covered with this rapid technique, more detailed (seismic) prospecting can be focused on the areas with apparent anomalies.

iii) ERT data collected along the levee crest, which represent the most common approach for embankment characterization, can lead to misinterpretations. The geometry of these hydraulic structures (i.e. limited width and wide length) does not allow a complete fulfilment of the hypotheses required for a 2D inversion. Therefore, even if longitudinal ERT data are collected with a survey line located in the middle of the embankment crest, the resulting resistivity distribution is not representative of the sole inner core of the levee, but also of the outer embankment parts. For these reasons, transverse ERT profiles are mandatory to fully explore the internal structure of the embankment, given the maximum resolution available. This aspect is clearly highlighted by the comparison between our longitudinal and cross-embankment resistivity sections. Even if the high resistivity zones in Fig. 4 were initially viewed as possible indicators of the grout wall, only the transverse sections revealed the electrical properties of the inner concrete part, which appears as a relatively conductive mean (see and compare Figs. 2 and 5). Therefore, the observed longitudinal high resistivity zones must be related to external tout-venant coarse layers.

iv) Grout injections have peculiar electrical properties that should be considered in ERT data interpretation. This is shown not only by the Frassine case study, but also by the Llobregat experiment, where grout is relatively more conductive also when buried in fairly conductive soils. Our transverse ERT data clearly show jet-grouting and the grout wall in the core of the studied embankment having resistivity values below 100 Ω m (as common in concrete test literature). Moreover, they also highlighted the presence of a discontinuity in the inner core of the cross-embankment section upstream. In the context of external coarse material, these appear as a conductive zone, and are not discernable from fine sediment deposits. If only longitudinal ERT profiles

were acquired, the reconstructed embankment would have appeared only as a resistive feature, with no ability to distinguish the real distribution of grout in the structure.

v) The use of GPR in embankment characterization must be treated with care. Classic GPR prospections run along the crest of the levee in order to observe heterogeneities, such as holes and cracks. In reality, the fine-grained structure of river embankments strongly limits the application of high frequency antennas due to attenuation, while low frequency antennas do not have enough resolution to detect possible animal burrows and other sources of seepage. On the contrary, at selected sections of the embankment, the use of trans-illumination experiments may prove useful. Even if attenuation limits the observable thickness, an estimation of water content inside the structure is possible via a well-established velocity analysis. As the presence of preferential infiltration paths modifies the volumetric water content, this approach is particularly useful to monitor reconstruction and waterproofing interventions affected by seepage phenomena, as shown in our case study.

Given the presented results, the use of different geophysical methods, compared and integrated with geotechnical data, can effectively characterize river embankment structures. In the event that these techniques cannot be jointly applied, then the use of the sole ERT is suggested. Not only did it allow for the grouting volume to be delineated, but it also showed heterogeneities that would have been difficult to identify with the other methods. Nevertheless, a careful interpretation of the data is mandatory, in order to avoid bestowing the effects to the wrong causes. In conclusion, non-invasive and cost-effective geophysical prospections should be used for both the characterization of inner structures and for the testing and monitoring of reconstruction interventions.

Acknowledgements

We wish to thank P. Simonini for the helpful discussions. We are also grateful to M. Rossi, A. Dacome and G. Asta for their help with fieldwork, and precious discussion. The use of the software provided by A. Binley is also gratefully acknowledged. This research did not receive any specific grant from funding agencies in the public, commercial, or not-for-profit sectors.

References

Annan, A.P., 2005. GPR methods for hydrogeological studies. In: Rubin, Y., Hubbard, S.S. (Eds.), Hydrogeophysics. Springer, Netherlands, pp. 185–213.

ARPAV (Veneto Regional Agency for environmental Prevention and Protection), 2010a. Dati alluvione 2010. www.arpa.veneto.it (accessed October 2015).

ARPAV (Veneto Regional Agency for environmental Prevention and Protection), 2013a. Servizio Osservatorio Suolo e Bonifiche. Carta dei suoli della provincia di Padova (ISBN: 978–88–7504-163-2).

Binley, A.M., Kemna, A., 2005. DC resistivity and induced polarization methods. In: Rubin, Y., Hubbard, S.S. (Eds.), Hydrogeophysics. Springer, Netherlands, pp. 129–156.

Boaga, J., Vignoli, G., Deiana, R., Cassiani, G., 2014. The influence of subsoil structure and acquisition parameters on surface wave mode contamination. J. Environ. Eng. Geophys. 19, 87–99. http://dx.doi.org/10.2113/JEEG19.2.87.

Bondesan, M., 2001. Hydrography. In: Castiglioni, G.B., Pellegrini, G.B. (Eds.), Illustrative Notes of the Geomorphological Map of Po Plain, Comitato glaciologico italiano. 2001, pp. 33–44.

Cardarelli, E., Cercato, M., De Donno, G., 2014. Characterization of an earth-filled dam through the combined use of electrical resistivity tomography, P- and SH-wave seismic tomography and surface wave data. J. Appl. Geophys. 106, 87–95. http://dx.doi.org/10.1016/j.jappgeo.2014.04.007.

Cassiani, G., Ursino, N., Deiana, R., Vignoli, G., Boaga, J., Rossi, M., Perri, M.T., Blaschek, M., Duttmann, R., Meyer, S., Ludwig, R., Soddu, A., Dietrich, P., Werban, U., 2012. Non-invasive monitoring of soil static characteristics and dynamic states: a case study highlighting vegetation effects. Vadose Zone J. 11 (3). http://dx.doi.org/10.2136/vzj2011.0195 Special Issue on SPAC - soil-plant interactions from local to landscape scale.

Cho, I.K., Yeom, J.Y., 2007. Crossline resistivity tomography for the delineation of anomalous seepage pathways in an embankment dam. Geophysics 72 (2), G31–G38. http://dx.doi.org/10.1190/1.2435200.

Dacome, A., Bersan, S., 2014. Verifiche in situ della permeabilità di argini fluviali mediante traccianti chimici. XXV Convegno Nazionale di Geotecnica: la geotecnica nella difesa del territorio e delle infrastrutture dalle calamità naturali. Atti, Baveno (Lago Maggiore).

Daily, W., Ramirez, A., Binley, A., Henry-Poulter, S., 1994. Electrical resistance tomography of concrete structures. ECAPT94: 3rd European Concerted Action Meeting on Process Tomography, Lisbon (Portugal), pp. 24–27 (Mar 1994).

Daily, W., Ramirez, A., Binley, A., LeBrecque, D., 2004. Electrical resistance tomography. Lead. Edge 23 (5), 438–442. http://dx.doi.org/10.1190/1.1729225.

Deiana, R., Cassiani, G., Villa, A., Bagliani, A., Bruno, V., 2008. Model calibration of a water injection test in the vadose zone of the Po River plain using GPR cross-hole data. Vadose Zone J. 7 (1), 215–226. http://dx.doi.org/10.2136/vzj2006.0137.

Di Prinzio, M., Bittelli, M., Castellarin, A., Pisa, P.R., 2010. Application of GPR to the monitoring of river embankments. J. Appl. Geophys. 71 (2), 53–61. http://dx.doi.org/10.1016/j.jappgeo.2010.04.002.

Feliu, S., Andrade, C., Gonzalez, J.A., Alonso, C., 1996. A new method for in-situ measurement of electrical resistivity of reinforced concrete. Mater. Struct. 29 (6), 362–365.

Fontana, A., Mozzi, P., Bondesan, A., 2008. Alluvial megafans in the Venetian–Friulian Plain (north-eastern Italy): evidence of sedimentary and erosive phases during Late Pleistocene and Holocene. Quat. Int. 189 (1), 71–90. http://dx.doi.org/10.1016/j.quaint.2007.08.044.

Foti, S., 2005. Surface wave testing for geotechnical characterization (pp. 47–71). Springer, Vienna.

Foti, S., Lai, C.G., Rix, G., Strobbia, C., 2015. Surface Wave Methods for Near-surface Characterization. CRC Press.

Hammond, E., Robson, T.D., 1955. Comparison of electrical properties of various cements and concretes. The Engineer 199 (5156), 114.

Henning, T., Weller, A., Canh, T., 2005. The effect of dike geometry on different resistivity configurations. J. Appl. Geophys. 57 (4), 278–292.

Inazaki, T., Sakamoto, T., 2005. Geotechnical characterization of levee by integrated geophysical surveying. Proceedings of the International Symposium on Dam Safety and Detection of Hidden Troubles of Dams and Dikes.

Ivanov, J., Miller, R.D., Dunbar, J.B., Smullen, S., 2005. Time-lapse seismic study of levees in southern Texas. Expanded Abstracts of the 75th Annual International Meeting. Society of Exploration Geophysicists, pp. 1121–1124.

Karastathis, V.K., Karmis, P.N., Drakatos, G., Stavrakakis, G., 2002. Geophysical methods contributing to the testing of concrete dams. Application at the Marathon Dam. J. Appl. Geophys. 50 (3), 247–260. http://dx.doi.org/10.1016/S0926-9851(02)00145-3.

Karhunen, K., Seppänen, A., Lehikoinen, A., Monteiro, P.J., Kaipio, J.P., 2010. Electrical resistance tomography imaging of concrete. Cem. Concr. Res. 40 (1), 137–145. http://dx.doi.org/10.1016/j.cemconres.2009.08.023.

Karl, L., Fechner, T., Schevenel, s.M., François, S., Degrande, G., 2011. Geotechnical characterization of a river dyke by surface waves. NSG 9 (6), 515–527. http://dx.doi.org/10.3997/1873–0604.2011030.

Komine, H., 1997. Evaluation of chemical grouted soil by electrical resistivity. Proc. Inst. Civ. Eng. Ground Improv. 1 (2), 101–113. http://dx.doi.org/10.1680/gi.1997.010203.

Lane Jr., J.W., Ivanov, J., Day-Lewis, F.D., Clemens, D., Patev, R., Miller, R.D., 2008. Levee evaluation using MASW: preliminary findings from the citrus lakefront levee, New Orleans, Louisiana. 21st EEGS Symposium on the Application of Geophysics to Engineering and Environmental Problems.

Neville, A.M., 2011. Properties of Concrete. fifth ed. Pearson Education Limited, Essex, England.

Niederleithinger, E., Weller, A., Lewis, R., 2012. Evaluation of geophysical techniques for dike inspection. J. Environ. Eng. Geophys. 17 (4), 185–195.

Oh, S., 2012. Safety assessment of dams by analysis of the electrical properties of the embankment material. Eng. Geol. 129, 76–90. http://dx.doi.org/10.1016/j.enggeo.2012.01.016.

Park, C.B., Miller, R.D., Xia, J., 1999. Multichannel analysis of surface waves. Geophysics 64 (3), 800–808. http://dx.doi.org/10.1190/1.1444590.

Perri, M.T., Boaga, J., Bersan, S., Cassiani, G., Cola, S., Deiana, R., Simonini, P., Patti, S., 2014. River embankment characterization: the joint use of geophysical and geotechnical techniques. J. Appl. Geophys. 110, 5–22. http://dx.doi.org/10.1016/j.jappgeo.2014.08.012.

Polder, R., Andrade, C., Elsener, B., Vennesland, Ø., Gulikers, J., Weidert, R., Raupach, M., 2000. Test methods for on site measurement of resistivity of concrete. Mater. Struct. 33 (10), 603–611.

Sharma, H.D., Reddy, K.R., 2004. Geoenvironmental Engineering: Site Remediation, Waste Containment, and Emerging Waste Management Technologies. John Wiley & Sons, Inc.

Shimizu, Y., 1928. An electrical method for measuring the setting time of portland cement. Mill Sec. Concrete 32 (5), 111–113.

Sjödahl, P., Dahlin, T., Johansson, S., 2009. Embankment dam seepage evaluation from resistivity monitoring data. NSG 7 (5–6), 463–474. http://dx.doi.org/10.3997/1873–0604.2009023.

Socco, L.V., Strobbia, C., 2004. Surface-wave method for near-surface characterization: a tutorial. NSG 2 (4), 165–185. http://dx.doi.org/10.3997/1873–0604.2004015.

Szynkiewicz, A., 2000. GPR monitoring of earthen flood banks/levees. 8th International Conference on Ground Penetrating Radar. International Society for Optics and Photonics, pp. 85–90.

Topp, G., Davis, J., Annan, A.P., 1980. Electromagnetic determination of soil water content: measurements in coaxial transmission lines. Water Resour. Res. 16 (3), 574–582. http://dx.doi.org/10.1029/WR016i003p00574.

Turk, N., Dearman, W.R., 1987. Assessment of grouting efficiency in a rock mass in terms of seismic velocities. Bull. Int. Assoc. Eng. 36 (1), 101–108.

Weller, A., Canh, T., Breede, K., Vu, N.T., 2006. Multi-electrode measurements at Thai Binh dikes (Vietnam). NSG, 4(2), 135–143, doi: http://dx.doi.org/10.3997/1873-0604.2005039.

Whittington, H.W., McCarter, J., Forde, M.C., 1981. The conduction of electricity through concrete. Mag. Concr. Res. 33 (114), 48–60. http://dx.doi.org/10.1680/macr.1981.33.114.48.